Nano Energy 58 (2019) 244–276

Contents lists available at ScienceDirect

Nano Energy

journal homepage: www.elsevier.com/locate/nanoen

Review

Earth abundant materials beyond transition metal dichalcogenides: A focus on electrocatalyzing hydrogen evolution reaction

Peng Yu[a,b,1], Fengmei Wang[b,*,1], Tofik Ahmed Shifa[b], Xueying Zhan[b], Xiaoding Lou[a,*], Fan Xia[a,*], Jun He[b,*]

[a] Engineering Research Center of Nano-Geomaterials of Ministry of Education, Faculty of Materials Science and Chemistry, China University of Geosciences, Wuhan 430074, China

[b] CAS Center for Excellence in Nanoscience, CAS Key Laboratory of Nanosystem and Hierarchical Fabrication, National Center for Nanoscience and Technology, Beijing 100190, China

ARTICLE INFO

Keywords:
Electrocatalysis
Hydrogen evolution reaction
Earth-abundant materials

ABSTRACT

The depletion of the unsustainable fossil fuels drives the exploration of renewable and clean energy. Hydrogen gas, as the potential alternative for the future energy supply, is now considered as the primary choice. Recently, with the assistance of the non-noble metal based compounds, electrocatalytic hydrogen evolution has aroused tremendous attention. In particular, earth abundant materials beyond transition metal dichalcogenides, such as transition metal phosphides, carbides, nitrides, demonstrate highly active and efficient activity toward hydrogen evolution reaction (HER) under different conditions. In this review, focused on these materials, we systemically discuss their recent development in electrocatalytic hydrogen generation. The synthesis routes utilized to prepare superior and specific catalyst are highlighted. Then, we provide insight into the characterization and electrochemical performance of these materials as HER electrocatalysts. In the end, the challenges of these materials, important issues about studying eletablctrocatalysts and future perspectives are stressed.

1. Introduction

Despite the tremendous technological advances of the modern era, our world is still threatened by the problem of energy dependence on unsustainable fossil fuels. Many governments and scientists are promoting a move away from non-renewable to renewable energy sources. In this aspect, hydrogen is supposed to be the potential alternative for the future energy supply provided that it is harnessed through spotless way [1–7]. Splitting water molecules (H_2O (l) → H_2 (g) + $1/2O_2$ (g), ΔG_0 = + 237.2 kJ mol^{-1}) for pure hydrogen gas has been thought as a clean and environmentally friendly route leading to profound transformations. Several substantial techniques, such as water-alkali [8–10] or proton exchange membrane (PEM) electrolyzers [11–13], solar water splitting devices [14,15], have been designed to produce pure hydrogen gas. In particular, the hydrogen evolution reaction (HER) occurred on cathode in electrolytic bath provides pure H_2 gas. But, this reaction generally depends on the considerable electrocatalysts due to the high overpotential needed in the process [16–18]. The utilization of electrocatalysts could accelerate the reaction kinetics and lower energy barrier of water dissociation, thereby decreasing the overpotential. Hence, efficient and potent electrocatalysts have to be sought to generate pure hydrogen gas via water splitting in solution of interest. To date, a variety of noble-metal free electrocatalysts have been extensively studied to electro-catalyze water splitting. Transition metal dichalcogenides (TMDs), especially, have attracted copious attention for fundamental research and practical application [19–23]. Of particular note is that the typical TMDs, i.e., MoS_2, has been extensively explored as an earth abundant candidate with high expectation to replace noble metals following theoretical and experimental proves [24,25]. Meanwhile, there are lots of reviews communicated so far to summarize the trends in MoS_2 and the rest TMDs [19–21,26-28]. It can be noted that numerous efforts, e.g., increasing edge sites [24,29,30], tuning phase [31–33], engineering defect [34–37] and introducing strain [38–40], have been made in an attempt to improve the electrocatalytic activity of TMD nanocatalysts. As a result, high overpotentials (> 150 mV) [19–21,26,41–43] to obtain the current density of 10 mA cm^{-2} in the HER process are usually observed on the TMD electrocatalysts, signifying that these materials still could not outperform the benchmark precious metals (e.g., Pt, Ru, Pd etc.).

Apart from TMDs, other noble metal-free compounds, including

* Corresponding authors.
E-mail addresses: wangfm@nanoctr.cn (F. Wang), louxiaoding@cug.edu.cn (X. Lou), xiafan@cug.edu.cn (F. Xia), hej@nanoctr.cn (J. He).
[1] These authors contributed equally to this work.

https://doi.org/10.1016/j.nanoen.2019.01.017
Received 4 December 2018; Received in revised form 24 December 2018; Accepted 5 January 2019
Available online 09 January 2019
2211-2855/

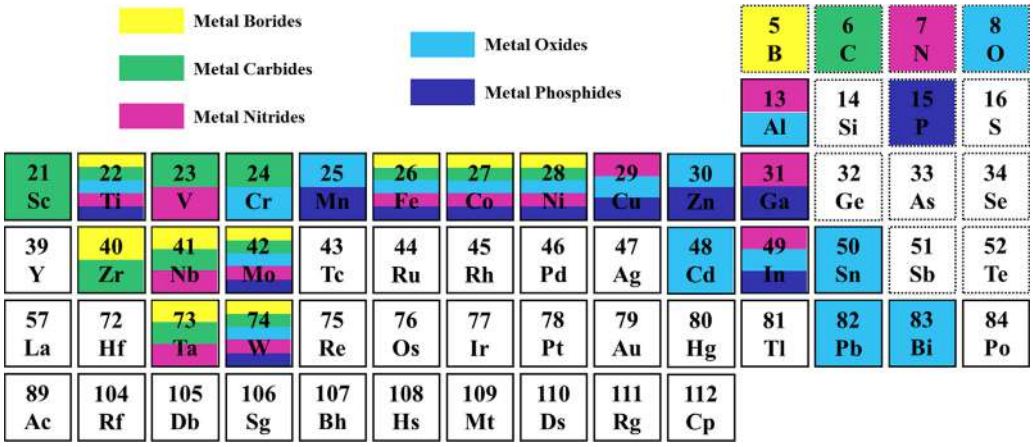

Fig. 1. The elements involved to prepare non-noble metal based HER electrocatalysts in the periodic table, in which the dashed and solid filled blocks represent non-metallic and metal elements, respectively.

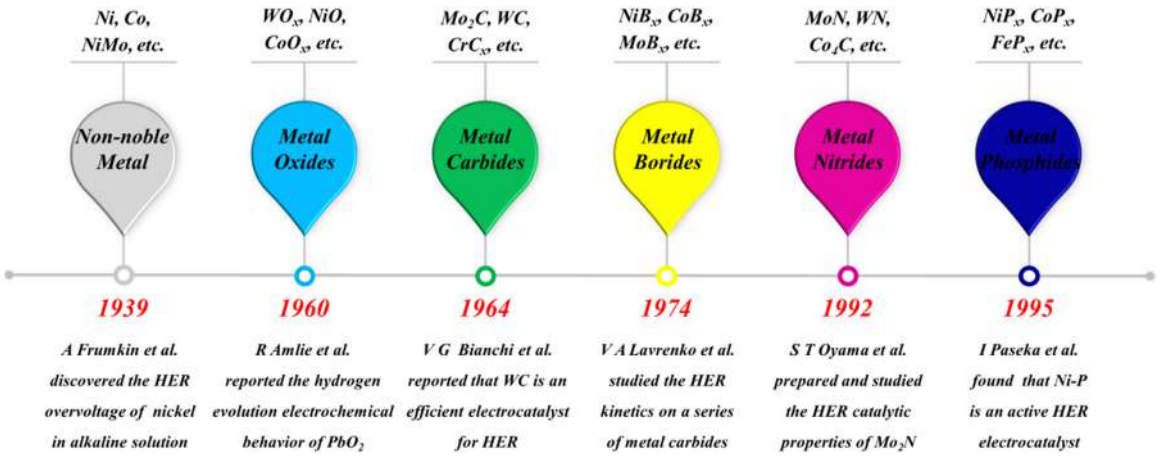

Fig. 2. The time development of the first reported non-noble metal based HER electrocatalysts. (Information are collected from Ref. [46,47,286,292,340,341]).

metal phosphides, metal carbides, metal nitrides and metal alloys, etc., have also been widely studied as HER electrocatalysts. Given their activity in hydrodesulfurization (HDS) process [44,45], where the binding of hydrogen ion regulates, these compounds are deemed to be the new earth-abundant HER catalysts. Fig. 1 demonstrates the timeline of first reported HER activities on various compounds. The hydrogen evolution was firstly realized with the assistance of nickel metal in alkaline solution [46]. Through time, other noble metal-free electrocatalysts were found to be active for catalyzing hydrogen evolution reaction. Until now, these materials are widely used as catalyst to split water for H_2 gas and the catalytic mechanism has gradually become uncovered. Significant researches were carried out in the last few years (Fig. 2) driven by the demand for designing efficient HER electrocatalysts in acidic, alkaline and neutral solutions. In 1995, I. Paseka et al. reported that the amorphous NiP_x layers with 3 wt% phosphorus demonstrated considerable HER activity in KOH solution [47]. After ten years, density functional theory (DFT) calculations validated the [NiFe] hydrogenase-like behavior of Ni_2P crystal, predicting it to be a potential HER catalyst [48]. More importantly, A. B. Laursen et al. reported crystalline Ni_5P_4 microparticles to be a superior HER elecrocatalyst, showing a small overpotential of 23 mV at 10 mA cm^{-2} with Tafel slope of 33 mV dec^{-1} in strong acidic media [49]. Besides metal phosphides, the metal carbides or nitrides are also utilized as HER electrocatalysts in all-pH electrolytes [50–54]. The electronic structure of these compounds, usually referred to as interstitial alloys, is easily modified by the incorporation of C and N atoms. In 1974, tungsten carbide, i.e., WC, was found to show the platinum-like catalytic activity [55,56]. The contribution of valence electrons from carbon to the 5*d* band of tungsten would give rise to increase in the width of unfilled portion on *d* band, resulting in a similar electronic structure to that of Pt [57]. This material has been proved to be an efficient cathode catalyst to generate hydrogen gas in conventional PEM and microbial electrolyzers [58,59]. And the Mo-based carbides (e.g., Mo_2C [51,60–62]) and nitrides (e.g., MoN [63–66]) have attracted substantial interest as HER electrocatalysts. Moreover, metal oxides and borides have also won attention in various research groups to electrocatalyze water splitting [67–71]. Notably, some earth-abundant metal alloys, like NiMo [72–74], FeCo [75,76], have been designed and reported to exhibit high HER catalytic activity and stability under alkaline conditions. Given the tremendous achievements on the noble metal-free electrocatalysts beyond TMDs, this research area has gone through considerable developments deserving a comprehensive outlook and plausible forecasts. To the best of our knowledge, there is, hitherto, no relevant analysis to systematically compare the performances and summarize the trends in the HER catalytic activities of these electrocatalysts. In this review, we start with introducing the mechanism of HER, the parameters to evaluate the HER performance and factors considered to design efficient HER electrocatalysts. Then, the recent developments in the area of non-noble metal electrocatalysts, including transition metal phosphides (TMPs), transition metal carbides (TMCs) and transition metal nitrides (TMNs), etc., are summarized. And the synthesis routes of these materials are highlighted. Specially, we review several potentially practical electrocatalysts (i.e., NiP_x, MoC_x and NiMo alloys) utilized to electrocatalyze water splitting. Some strategies like heteroatom doping,

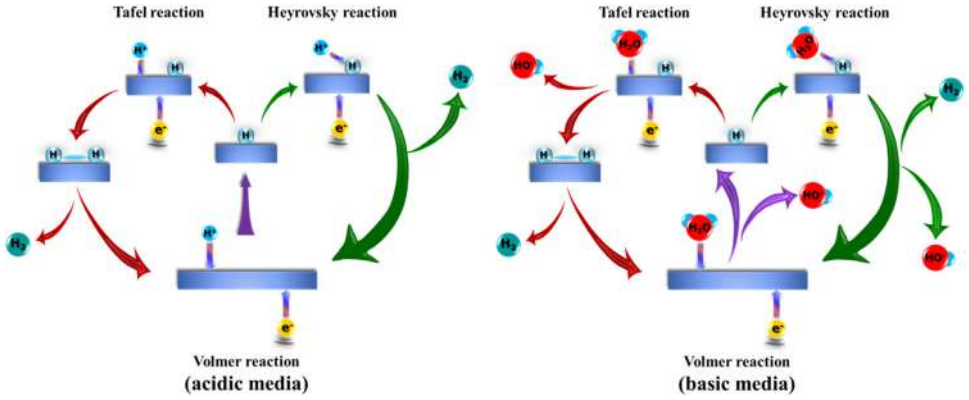

Fig. 3. Mechanism of HER electrocatalysis in two different media.

nanostructuring, constructing heterostructures etc. to optimize the HER efficiencies are also discussed. Finally, the challenges and future perspectives of these materials are stressed.

2. Electrochemical hydrogen evolution reaction

2.1. Electrocatalytic mechanism of HER

Hydrogen evolution reaction (HER), which is the cathodic half reaction of water electrolysis, has been one of the most thoroughly studied electrochemical reactions, recently. It generally contains two successive electrochemical steps as has been confirmed from the mechanisms studied on Pt-based electrocatalysts (Fig. 3) [77,78]. During the first step, i.e., Volmer reaction, the external circuit provides an electron coupling with a proton adsorbed on the surface of the electrocatalyst, to yield an adsorbed hydrogen atom (H_{ads}) intermediate. Volmer reaction is then followed by either a combination of two hydrogen atoms (Tafel reaction) or combination of an adsorbed hydrogen atom with a proton and an electron (Heyrovsky reaction). From the perspective of HER mechanism, the adsorbed protons vary with the electrolyte and play a vital role. In acidic media (e.g., H_2SO_4), protons exist in the form of hydronium ions (H_3O^+), while water molecules (H_2O) act as the proton source in alkaline (e.g., KOH) or neutral media (e.g., phosphate buffer electrolyte) (Table 1). Plethora of studies have been reported to reveal the intrinsic electrochemical activities and electronic structures of the electrocatalysts, which are closely related to their reaction pathways [79–82].

2.2. Parameters for evaluating electrocatalysts

Numerous parameters have been used elsewhere to evaluate how effective a given catalyst is. Deep understanding of these parameters is essential to design an active, efficient and robust catalyst. In the following section, the physicochemical meaning and interpretation of some commonly employed parameters are elaborated in the context of HER.

(i) **Gibbs free energy and overpotential**

The electrochemical adsorption and desorption of hydrogen atoms on the electrocatalyst surface is a pair of competitive reaction in nature. An optimal HER catalyst should adsorb H atoms neither too weakly nor too strongly on its surface. According to the Sabatier principle [83], a desired HER electrocatalyst should exhibit the ideal trade-off between the binding and releasing of the H_{ads} intermediate. The moderate bonding strength of the electrocatalyst to H_{ads} intermediate not only facilitate the charge/mass transfer but also assure a facile bond breaking and rapidly release of hydrogen molecules [84]. Unfortunately, the establishment of quantitative relationships between the energetics of the H_{ads} intermediate and the electrochemical hydrogen generation reaction rate is difficult due to the lack of direct measurement of values for the H_{ads} bonding energy. As a result, the calculated Gibbs free energy of hydrogen (ΔG_H^*) can be used as a crucial descriptor to evaluate the catalytic activity of the HER catalysts [80,85–89]. As guided by the volcano plot in which the experimental j_0 as a function of the DFT-calculated ΔG_H^* (Fig. 4) [87], the ΔG_H^* of optimal catalyst should approach to thermoneutral (e.g., $\Delta G_H^* \approx 0$), the electrochemical hydrogen production will have the maximum reaction rate under this condition. Therefore, the ΔG_H^* can act as an important reference for screening and theoretical prediction of superior HER catalysts.

In fact, there is no electrochemical reaction that occurs at the potential predicted only by thermodynamic considerations excluding the kinetic hindrances experienced in a real system. Thus, the actual potential where reaction takes place is different from Nernstian potential and the difference between the two potentials corresponds to overpotential (η) [80]. There are three plausible sources for the rise of overpotential, viz., activation overpotential, concentration overpotential and uncompensated resistance overpotential which is exerted by the electrochemical interfaces. The activation overpotential is an intrinsic property of the catalyst and varies from one material to another. Hence, it can be minimized by choosing an efficient catalyst. The concentration overpotential occurs as soon as the electrode reaction begins as a result of the sudden drop in concentration near the interfaces. This can be minimized by homogenizing the electrolyte through stirring the solution. The resistance overpotential can be minimized by conducting Ohmic drop compensation. This option is now available in many modern electrochemical workstations that are equipped to automatically compensate for *i*R loss. Experimentally, the value of

Table 1
Mechanism of HER electrocatalysis in acidic and basic media.

Steps	Acidic media	Basic media	Tafel slope (25 °C)
Volmer reaction	$H^+ + M + e^- \rightarrow M\text{-}H_{ads}$	$H_2O + M + e^- \rightarrow M\text{-}H_{ads} + OH^-$	$\approx 120\ mV\ dec^{-1}$
Heyrovsky reaction	$M\text{-}H_{ads} + H^+ + e^- \rightarrow M + H_2$	$M\text{-}H_{ads} + H_2O + e^- \rightarrow M + OH^- + H_2$	$\approx 40\ mV\ dec^{-1}$
Tafel reaction	$2M\text{-}H_{ads} \rightarrow 2M + H_2$	$2M\text{-}H_{ads} \rightarrow 2M + H_2$	$\approx 30\ mV\ dec^{-1}$

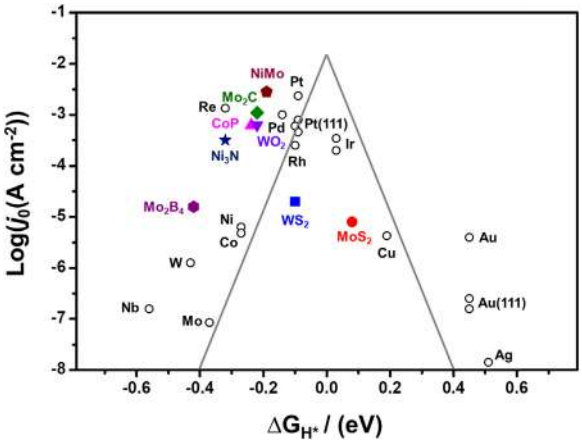

Fig. 4. The non-noble metal based compounds, compared with other HER electrocatalysts, in the "Volcano" plot of exchange current density (j_0) as a function of DFT-calculated Gibbs free energy of adsorbed atomic hydrogen (ΔG_{H^*}). (Data are extracted from Ref. [24,38,62,86,87,127,294,307,342]).

overpotential at specified current density is utilized to evaluate the performance of electrocatalysts. In a typical electrocatalysis, the most significant point is the issue of how much current do the catalyst achieve for the amount of overpotential that is applied. For ease of quantifying the overpotential, two parameters, i.e., onset overpotential and overpotential at current density of 10 mA cm^{-2} (η_{10}) are frequently utilized as figure of merits. Onset overpotential is the extra potential at which the current density starts to increase remarkably [20,90,91]. The η_{10} corresponds to the commercially equivalent photoelectrochemical water splitting efficiency of 12.3%, which is regarded as an important criterion. A high-efficiency electrocatalyst should exhibit a low overpotential when electrochemically generating hydrogen gas.

(ii) **Tafel slope and exchange current density**

The Tafel equation (Eq. (1)) is an extremely important formula in electrochemical reactions and is usually used to reveal the relationship between steady-state current density and overpotential [87,92]. From this equation, one can obtain two important parameters, Tafel slope (b) and exchange current density (j_0). Tafel slope is usually used as an indication to discern the charge transfer kinetic of the hydrogen evolution process [93]. In fact, it can be theoretically derived from the Butler-Volmer equation (Eq. (2)) [92]. When the overpotential is high ($\eta > 50$ mV), the Butler-Volmer equation can be simplified as Eq. (3).

$$\eta = a + b \log j \tag{1}$$

$$j = j_0 [-e^{-\alpha n F \eta / RT} + e^{(1-\alpha) n F \eta / RT}] \tag{2}$$

$$\eta = a + b \log j = \frac{-2.3RT}{\alpha n F} \log j_0 + \frac{2.3RT}{\alpha n F} \log j \tag{3}$$

Volmer reaction:

$$b_1 = \frac{2.3RT}{\alpha F} \tag{4}$$

Heyrovsky reaction:

$$b_2 = \frac{2.3RT}{(1+\alpha)F} \tag{5}$$

Tafel reaction:

$$b_3 = \frac{2.3RT}{2F} \tag{6}$$

Where α is the charge transfer coefficient, n is the number of electrons transferred, F (96485C mol^{-1}) is the Faraday constant, R (8.314 J mol^{-1} C^{-1}) is the ideal gas constant, and T (K) is the absolute temperature. From the Tafel slope analysis in the Butler-Volmer kinetic model, it can be deduced that each reaction intermediate of the hypothesis could be a rate-determining step [77]. At 298 K, the Tafel slopes of the above mentioned three reactions are calculated to be $b_1 \approx 120$ mV dec^{-1}, $b_2 \approx 40$ mV dec^{-1}, and $b_3 \approx 30$ mV dec^{-1}, respectively. This means that when the value of b is close to 120 mV dec^{-1} (Eq. (4)), Volmer reaction is a rate-determining step, and the electrochemical adsorption reaction of hydrogen atoms on the electrocatalyst surface is sluggish. If the value of Tafel slope approaches to 40 mV dec^{-1} (Eq. (5)), Heyrovsky reaction is the rate-determining step. In this case, the electrochemical adsorption reactions of hydrogen atoms occur easily, and the generation of hydrogen molecules is mainly governed by electrochemical desorption. If the value of Tafel slope is about 30 mV dec^{-1} (Eq. (6)), obtained on commercial Pt/C, the combination of adsorbed hydrogen atom and desorption of hydrogen molecules will be limiting steps. Based on the above discussion, one can refer to the value of Tafel slope to infer the hydrogen generation pathway.

In addition, the exchange current density (j_0) is another key descriptor to estimate the intrinsic reactivity of the electrocatalysts under equilibrium conditions. It is valued with the overpotential of zero, which profoundly depends on the reaction activation energy at the surface of the electrocatalyst [80,87]. The j_0 is comparable to the rate constants used in heterogeneous electrocatalysis, it is governed by both kinetics and thermodynamics. Usually, it assumes a very low value due to the unavailability of net current at equilibrium signifying the extent of oxidation or reduction that may occur. The intrinsic property of electrocatalyst materials, electrolyte composition and temperature will influence the value of j_0 [92]. It can be calculated by extrapolating the linear part of Tafel plots. A desirable electrocatalyst should possess a small Tafel slop (b) and a high exchange current density (j_0) simultaneously.

(iii) **Faradic efficiency and stability**

Faradic efficiency (FE), also called columbic efficiency, is an importantly technical and economic index in electrochemical reactions. It describes the proportion of electrons participating in the desired reaction versus total electrons supplied via external circuit in the desired reaction. In HER process, Faradic efficiency is defined as the ratio of the experimentally detected amount of hydrogen gas versus theoretically generated hydrogen gas [20,91]. The actual amount of hydrogen produced can be measured by gas chromatography (GC), and the theoretical hydrogen production can be calculated by integrating galvanostatic or potentiostatic electrolysis plot. However, due to the presence of side reactions on the electrode surface, the utilization efficiency of electrons is usually less than 100%.

Besides, long-term stability is also a crucial parameter to evaluate the performance of HER electrocatalysts. The robust catalysts could be potentially used in the practical application. Typically, cyclic voltammetry (CV) and galvanostatic or potentiostatic results are collected to judge the stability of the electrocatalysts. The negligible variation of the CV cycles and polarization curve obtained before and after long-term (> dozens of hours) measurement indicates the good durability.

(iv) **Electrochemical active surface area and turnover frequency**

With the advent of the nanotechnology era, the exploration of nanocatalysts has gone through significant advancements. When the

materials are brought from bulk to nanoscale, the atoms are maximally exposed to the surface thereby leading to the ease-accessibility of active sites to bind the incoming intermediates/reactants. Hence, the increasing surface-to-volume ratio with decreasing particle size strongly increases the specific catalytic activity as a result of the large specific surface area. In connection to this, estimation of the electrochemical active surface area (ECSA) is particularly important for evaluating the performance of the catalyst. One of the most commonly employed ECSA estimation methods is measuring cyclic voltammetry (CV) in the non-faradaic regions [93]. When performing the CV test, the non-faradaic current density (j) should be linearly related to scan rate (ν) in such a way that the electrochemical double-layer capacitance (C_{dl}) can be derived from the slope (Eq. (7)). After normalizing the double layer capacitance with the double layer capacitance of a flat surface, roughness factor (RF) can be estimated from Eq. (8). Given the value of the roughness factor, multiplying it with density of active sites on flat surface yields density of electrochemically active sites [87].

$$C_{dl} = \frac{j}{\nu} \tag{7}$$

$$RF = \frac{C_{dl}}{C_{dl-Ref}} \tag{8}$$

Besides, ECSA can also be estimated by underpotential deposition or carefully morphology characterization of the electrode via advanced electron microscopy [93]. It is worth noting that the chemical nature and preparation of the electrodes should be seriously considered when measuring the active surface area. For instance, some carbon-supported composites can result in overestimation of ECSA and underestimation of catalytic activity. In general, ECSA elucides information on the number of active sites of the electrocatalyst, but not all active sites are catalytically reactive. ECSA can still serve as an important reference for evaluation of catalyst performance.

To evaluate the efficiency of each active site on catalysts, turnover frequency (TOF) have to be considered [94]. TOF, representing the intrinsic activity of each active site, is defined as the number of desired reactions occurring at each active site per unit time. But, the measurement of TOF is challenging owing to the precise number of active sites per unit area is difficult to unequivocally elucidate. Especially for some emerging complex catalysts, the exact determination of the number of active site is difficult and hence various approximations are usually followed. Despite the fact that the calculated TOF is relatively imprecise, it may still give insights into the comparative catalytic activity or efficiency of different materials.

3. Non-novel metal based electrocatalysts

Over the past few decades, remarkable endeavors have been made to develop non-precious metal based electrocatalysts for hydrogen evolution. The earth-abundant transition metal based compounds arouse the attention of the researchers due to the cost-effective and specific electronic structure. Although plethora of experimental/theoretical reports and review articles have been communicated so far for transition metal dichalcogenides (TMDs), the recent research progress indicates that other types of transition metal compounds such as transition metal phosphides (TMPs), transition metal carbides (TMCs), transition metal nitrides (TMNs), transition metal oxides (TMOs), and transition metal borides (TMBs) have gone through considerable development in the electrocatalytic water splitting. These research arenas, therefore, deserves a comprehensive outlook and plausible forecasts. Here we review this aspect with particular attention is paid to the discussion of their classification, relationship between structure/composition and electrocatalytic activity and also strategies to improve the electrocatalytic performance of these materials for HER.

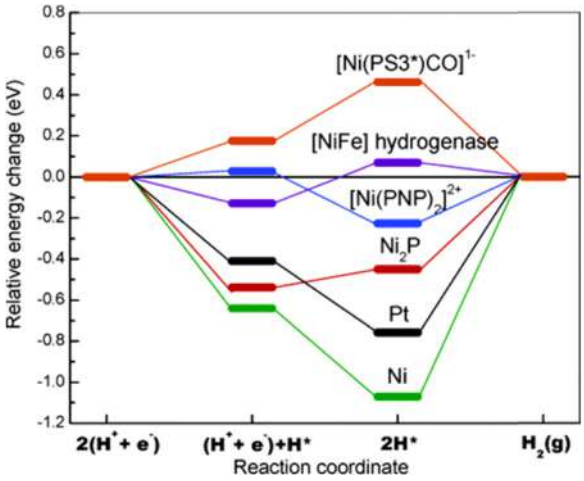

Fig. 5. Calculated energy changes for the HER on the [NiFe] hydrogenase, the $[Ni(PS_3{*})(CO)]^{1-}$ and $[Ni(PNP)_2]^{2+}$ complexes, plus $Ni_2P(001)$, Pt(111) and Ni (111) surfaces. (Reproduced from Ref. [48] with permission from American Chemical Society, Copyright 2005).

3.1. Transition metal phosphides

As the promising non-noble metal based electrocatalysts, transition metal phosphides (TMPs, TM = Fe, Co, Ni, Cu, Mo and W) have attracted a considerable interest recently. And they will likely be the candidate to replace the Pt-group nanomaterials for their highly efficient HER activities [95–99]. In 2005, inspired by the resemblance of biological pathway catalyzed by [NiFe] hydrogenase [48], Rodriguez et al. found that $Ni_2P(001)$ have an outstanding catalytic activity toward HER over the conventional Pt-group catalyst, which is ascribed to the crucial roles of P atoms for hydrogen production, based on density functional theory (DFT) calculations (Fig. 5). The P sites could provide moderate bonding to the reaction intermediates involved in the HER [48]. The proton-acceptor of P site, along with the hydride-acceptor centers of Ni site, on the surface of Ni_2P work in cooperative way to promote the hydrogen generation process. Of note, the electronic structure of TMPs is easily tuned via continuously doping P atom. Compared with metal (Ni, Co, Fe, etc.) atoms, P atoms usually possess the stronger electronegativity, resulting in withdrawing electrons from metal atoms. Thus, the positively charged protons are trapped on the P sites during the electrochemical hydrogen evolution [48,100]. From the previous studies [101,102], it is found that the increasing in atomic content of P for TMPs may effectively improve their HER activity within an appropriate range [49,101]. The excess P doping in TMPs crystals would restrict the delocalization of electrons around the metal atoms and gave rise to the decrease in the conductivity of the electrocatalyst, which severely hinders the charge transfer in the electrochemical hydrogen production [103,104]. Therefore, the appropriate ratio of P atoms should be seriously considered and controlled when utilizing the TMP crystals as catalysts for electrochemical hydrogen generation.

In the early times, the synthesis of almost all metal phosphides undergo high temperature or high pressure with flammable elemental phosphorus or noxious phosphine as the phosphorus source, which significantly hindered the developments and applications of TMPs. Until now, various methods have been developed to synthesize TMP nanomaterials. A variety of phosphorus sources, including organic phosphorus (e.g., trioctylphosphine [101,105]), inorganic phosphorus (e.g., hypophosphite [106,107], phosphate [100,108]), and elemental phosphorus (e.g., red phosphorus [109,110]) are utilized. It should be noted that the synthetic method of TMP nanomaterials is closely related to the selected phosphorus sources. Generally, organic phosphorus is used in wet-chemical method, and elemental phosphorus is used in high-temperature solid phase reaction. The detailed growth methods,

Table 2
Compilation of HER performance based on various transition metal phosphide electrocatalysts under different conditions.

Materials	Substrate	Electrolyte	Overpotential (mV)		Tafel slope (mV dec^{-1})	Loading density (mg cm^{-2})	Year	Ref.
			η_{10}	η_{100}				
NiP_2 NS	Carbon cloth	1.0 M KOH	~ 190	–	54	0.8	2014	[123]
Ni_5P_4 MPs	Ti foil	1.0 M H_2SO_4	23	62	33	177	2015	[49]
Ni-P	Carbon fiber	0.5 M H_2SO_4	98	162	59	~ 0.3	2016	[343]
Ni_xP	Ni foam	0.5 M H_2SO_4	~ 90	180	39	~ 1.0	2014	[344]
Ni_2P NPs	Ti foil	0.5 M H_2SO_4	~ 120	180	46	~ 1.0	2013	[113]
$Ni_{12}P_5$ NPs	Ti foil	0.5 M H_2SO_4	107	–	63	3.0	2014	[124]
Ni_3P MPs	Ti foil	0.5 M H_2SO_4	65	~ 172	41	177	2018	[118]
$Ni_{12}P_5$ NPs/CNTs	Ti foil	0.5 M H_2SO_4	129	–	56	~ 0.75	2015	[345]
Co-P films	Cu foil	1.0 M KOH	94	~ 145	42	–	2015	[346]
CoP NPs	Ti foil	0.5 M H_2SO_4	75	–	50	2.0	2014	[112]
CoP NS	Ti foil	0.5 M H_2SO_4	90	146	43	~ 2.0	2014	[347]
CoP NPs	Ti foil	0.5 M H_2SO_4	75	~ 150	50	~ 1.0	2015	[102]
CoP NWs	Carbon cloth	0.5 M H_2SO_4	67	204	51	0.92	2014	[126]
CoP NWs	GCE	0.5 M H_2SO_4	110	–	54	~ 0.35	2014	[106]
CoP branch	Ti foil	0.5 M H_2SO_4	100	–	48	~ 1.0	2015	[133]
CoP NCs	GCE	0.5 M H_2SO_4	~ 105	180	46	0.28	2015	[107]
CoP UPNSs	GCE	0.5 M H_2SO_4	56	131	44	0.28	2017	[127]
Co_2P NPs	Ti foil	0.5 M H_2SO_4	95	~ 180	45	~ 1.0	2015	[102]
CoP_3 CPs	Carbon fiber	0.5 M H_2SO_4	78	–	53	1.0	2017	[130]
CoP_3 NSs	Carbon cloth	1.0 M KOH	121	–	66	1.0	2017	[110]
CoP/CNT	GCE	0.5 M H_2SO_4	122	–	54	0.285	2014	[115]
CoP/PANI HNWs	Carbon fiber	0.5 M H_2SO_4	57	122	35	0.8	2018	[132]
Co_2P@C	Carbon cloth	0.5 M H_2SO_4	103	179	41	–	2017	[128]
CoP_2/RGO	GCE	1.0 M KOH	88	–	50	0.285	2016	[129]
FeP NAs	Carbon cloth	0.5 M H_2SO_4	58	–	45	~ 1.5	2014	[348]
FeP NPs	Ti foil	0.5 M H_2SO_4	154	–	65	~ 0.72	2016	[349]
FeP NPs	Ti foil	0.5 M H_2SO_4	50	–	37	~ 1.0	2014	[111]
FeP NA	Ti foil	0.5 M H_2SO_4	55	127	38	0.285	2014	[114]
FeP	FTO	0.5 M H_2SO_4	116	~ 210	79	–	2018	[138]
FeP_2 NWs	Fe foil	0.5 M H_2SO_4	61	–	37	–	2016	[350]
Fe_2P	FTO	0.5 M H_2SO_4	83	~ 163	66	–	2018	[138]
Fe_3P	FTO	0.5 M H_2SO_4	49	~ 135	57	–	2018	[138]
FeP NPs@C	GCE	0.5 M H_2SO_4	71	–	52	0.44	2017	[139]
FeP/Fe@NC	GCE	0.5 M H_2SO_4	49	~ 130	67	1.4	2018	[351]
FeP NRs/VAGNs	Carbon cloth	0.5 M H_2SO_4	53	~ 115	42	~ 0.78	2017	[148]
Cu_3P NWs	Cu foil	0.5 M H_2SO_4	143	276	67	15.2	2014	[142]
Cu_3P NS	Ni foam	1.0 M KOH	105	–	42	~ 1.2	2017	[141]
Cu_3P MSs	Ni foam	1.0 M KOH	130	–	83	0.25	2016	[146]
Cu_3P@NPPC	GCE	0.5 M H_2SO_4	89	–	76	0.29	2017	[143]
MoP	GCE	0.5 M H_2SO_4	~ 130	–	54	− 0.86	2014	[100]
MoP NPs	GCE	0.5 M H_2SO_4	125	200	54	0.36	2014	[108]
MoP NPs	Ti foil	0.5 M H_2SO_4	90	–	45	~ 1.0	2014	[153]
MoP_2 NPs	Mo Plate	0.5 M H_2SO_4	143	199	57	~ 0.18	2016	[155]
MoP/CNT	Carbon fiber	0.5 M H_2SO_4	83	142	60	0.5	2018	[149]
MoP@PC	GCE	0.5 M H_2SO_4	153	–	66	0.41	2016	[150]
MoP@C	GCE	1.0 M KOH	125	–	49	~ 0.5	2018	[152]
MoP@RGO	GCE	1.0 M KOH	~ 70	–	58	~ 0.28	2016	[154]
MoP/NG.	GCE	0.5 M H_2SO_4	94	–	50	0.28	2018	[156]
MoP@NPC/rGO	GCE	0.5 M H_2SO_4	218	–	57	0.14	2017	[151]
WP NPs	Ti foil	0.5 M H_2SO_4	120	–	54	1.0	2014	[164]
WP NAs	Carbon cloth	0.5 M H_2SO_4	130	230	69	2.0	2014	[109]
WP_2 SMPs	GCE	0.5 M H_2SO_4	161	294	57	0.5	2015	[116]
WP_2 NWs	Carbon cloth	0.5 M H_2SO_4	109	~ 190	56	6.0	2016	[119]
WP_2 NSs	Graphite paper	0.5 M H_2SO_4	155	~ 240	66	4.8	2017	[352]
WP_2 NPs	W foil	0.5 M H_2SO_4	143	211	66	~ 0.2	2016	[203]
WP NPs@NC	GCE	0.5 M H_2SO_4	102	–	58	2.0	2016	[165]
FeCoP	Carbon cloth	0.5 M H_2SO_4	37	98	30	2.2	2016	[177]
MoWP	Carbon cloth	0.5 M H_2SO_4	–	138	52	~ 4.0	2016	[204]
NiCoP	Carbon felt	1.0 M KOH	58	127	34	5.9	2016	[353]
$MoP_{2(1-x)}S_x$	Ti foil	0.5 M H_2SO_4	120	–	57	0.28	2015	[181]
CoPS NPIs	Graphite disk	0.5 M H_2SO_4	48	–	56		2015	[179]
CoP|S/CNT	Carbon fiber	0.5 M H_2SO_4	48	109	55	1.6	2016	[178]

Note: GCE, glassy carbon electrode; FTO, fluorine-doped tin oxide.

classified according to phosphorus source, will be discussed as follows.

(i) Organic phosphorus: A versatile trioctylphosphine (TOP) is commonly used in wet-chemical method at the temperature above 300 °C [111–113]. The high boiling-point organic solvents (e.g., oleylamine, octadecene and squalene etc.) are utilized to ensure the completion of the reaction yielding metal phosphides. Typically, the C-P covalent bond in TOP molecular can easily be broken over 320 °C so that it can efficiently promote the reaction. For instance, highly dispersible, uniformly sized FeP [111], CoP [112] and Ni_2P [113] nanoparticles were prepared by taking advantage of TOP as phosphorus sources to coordinate with metal atoms of metal

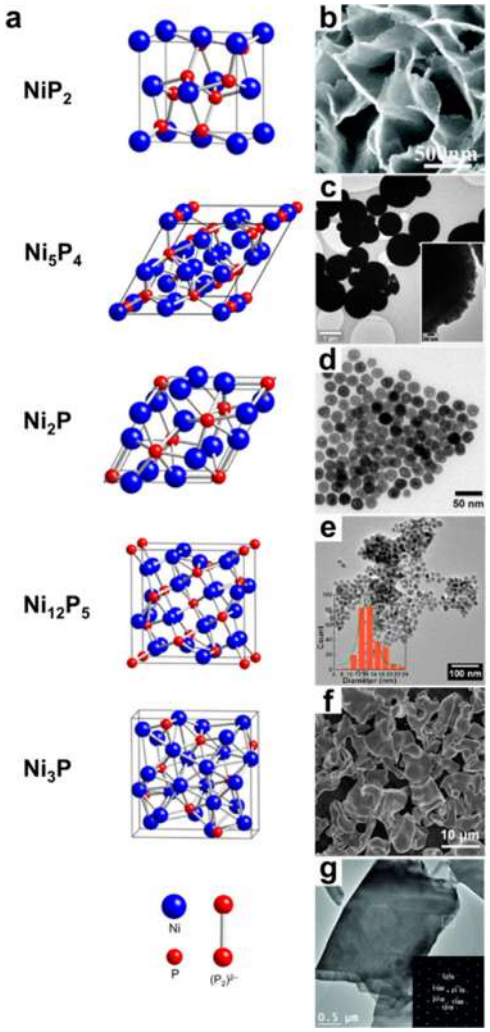

Fig. 6. (a) Crystal structures of various nickel phosphides spanning a range of Ni to P ratios. (Reproduced from Ref. [120] with permission from American Chemical Society, Copyright 2016). (b) Scanning electron microscopy (SEM) image of NiP_2 nanosheet arrays. (Reproduced from Ref. [123] with permission from The Royal Society of Chemistry, Copyright 2014). (c) Transition electron microscopy (TEM) image of Ni_5P_4 microparticles. (Reproduced from Ref. [49] with permission from The Royal Society of Chemistry, Copyright 2015). (d) TEM image of Ni_2P nanoparticles. (Reproduced from Ref. [113] with permission from American Chemical Society, Copyright 2013) (e) TEM image of $Ni_{12}P_5$ nanoparticles. (Reproduced from Ref. [124] with permission from American Chemical Society, Copyright 2014). (f) SEM image of Ni_3P microparticles. (Reproduced from Ref. [118] with permission from American Chemical Society, Copyright 2018). (g) TEM image of single Ni_5P_4-Ni_2P nanosheets. (Reproduced from Ref. [104] with permission from John Wiley & Sons, Inc., Copyright 2015).

acetylacetonates under thermal decomposition temperature. In this method, the phase, morphology and size of metal phosphide can be controlled by changing the reaction conditions, such as reaction temperature, solvent type and the ratio of phosphorus to metal [33,101]. Nevertheless, it is important to note that this reaction is carried out only under rigorously air-free conditions due to the release of phosphorus which is highly corrosive and flammable.

(ii) Inorganic phosphorus: This is another common phosphorus source for growing TMPs via chemical vapor reaction. Here, hypophosphite is made to pass through in situ pyrolysis to generate PH_3 instead of directly using extremely noxious PH_3 for solid-phase reaction. A simple operating procedure is to heat the mixture of metal precursors (e.g., metal oxides, metal hydroxides and metal-organic frameworks) and hypophosphite (e.g., $NH_4H_2PO_2$, NaH_2PO_2) over 300 °C under protective gas flow. More importantly, this hypophosphite-based reaction strategy can maximize the retention of precursors dimension and morphology. X. Sun's group prepared FeP nanowire arrays [114], CoP/CNT nanohybrid [115] and WP_2 submicroparticles [116] through this method with low-temperature hypophosphite reaction. In addition, phosphates (e.g., $(NH_4)_2HPO_4$) are also used in the preparation of TMPs, especially molybdenum phosphides [100,108] and tungsten phosphides [116]. Briefly, a mixture of stoichiometric phosphate and polymolybdate or polytungstate is subjected to hydrothermal, calcination and annealing process in sequence.

(iii) Elemental phosphorus: It is important to note that the advantage of using elemental phosphorus as a phosphorus source is the production of phosphorus-rich phosphides with high yield by tuning growth temperature and the metal/phosphorus ratio [109,117,118]. Usually, the chemical vapor reaction is utilized. For instance, the phosphorus-rich FeP_2/C nanohybrids [117] and WP_2 nanowire arrays [119] were synthesized via solid-phase phosphating reaction of red phosphorus.

In short, these three routes could be summarized with the following chemical reactions (9 – 13):

Route *i* (organic phosphorus):

$$(C_8H_{17})_3P + M(acac)_2 \rightarrow MP_x \quad (9)$$

Route *ii* (inorganic phosphorus):

$$2NaH_2PO_2 \rightarrow Na_2HPO_4 + PH_3 \uparrow \quad (10)$$

$$PH_3 + M_yO_z \rightarrow MP_x \quad (11)$$

or

$$(NH_4)_2HPO_4 + (NH_4)_6Mo_7O_2 \rightarrow MP_x \quad (12)$$

Route *iii* (elemental phosphorus):

$$P + M \rightarrow MP_x \quad (13)$$

Given the similarity of metal phosphides and hydrogenase [48], many researchers around the world have contributed extensively to the advancement of this field, including the exploring various metal phosphides as efficient hydrogen evolution catalysts, developing improved method to prepare TMP nanomaterials, investigating their catalytic mechanisms, and demonstrating their applicability in integrated systems and devices [120]. Table 2 collects HER performance of various metal phosphide electrocatalysts under different conditions. In the subsequent subsection, the prominent roles and developments in research endeavors of frontier metal phosphides are discussed.

3.1.1. Nickel phosphides

The bio-inspired design of HER catalysts opened up a route to the widespread investigation of nickel phosphide due to its resemblance with [NiFe] hydrogenase [48]. It is reported that the crystal structures of nickel phosphides can appear in several different phases with various atomic ratios of P: Ni (i.e., NiP_x). And their electronic structure and physicochemical properties vary with composition and structure [120–122]. To date, nickel phosphides of a phosphorus-rich phase with $x > 1$ (e.g., NiP_2 [123]) and metal-rich phases with $x < 1$ (e.g., Ni_5P_4 [49], Ni_2P [113], $Ni_{12}P_5$ [124], and Ni_3P [118]) have been reported to exhibit superior electrocatalytic performance toward the HER (Fig. 6). In order to gain deep insight into the electrocatalytic activity of various NiP_x nanocatalysts, numerous studies have been explored and conducted.

In 2014, X. Sun and co-workers successfully constructed NiP_2 nanosheet arrays structure on carbon cloth (NiP_2 NS) via hypophosphite-based reaction route (Route *ii*) (Fig. 6b) [123]. The as-prepared NiP_2 NS

demonstrated superior HER performance with the overpotential required to produce cathodic current density of 10 mA cm^{-2} (η_{10}) and 100 mA cm^{-2} (η_{100}) is 75 mV and 204 mV in 0.5 M H_2SO_4, respectively. The long-term electrocatalytic activity of NiP_2 NS on carbon cloth is preserved for at least 57 h. Later, considering the outstanding conductivity of Ni_5P_4, Dismukes et al. synthesized Ni_5P_4 microparticles for generating H_2 gas in both acidic and alkaline media [49]. As shown in the TEM image of micron-sized Ni_5P_4 in Fig. 6c, their size is around 0.3 ~ 1.8 μm. They exhibited exceptionally high HER activity, with a low overpotential of η_{10} = 23 mV and a small Tafel slope of 33 mV dec^{-1} in 1.0 M H_2SO_4, which is comparable to that of commercial Pt/C. Meanwhile, their HER activity with η_{10} = 49 mV in alkaline media (1.0 M NaOH) also outperformed that of the analogous Ni_2P nanocrystals. Note that, when decreasing the ratio of P ($x < 1$) atoms in nickel phosphides, the HER activity of NiP_x is restricted. For instance, Schaak et al. utilized organic phosphine pyrolysis (Route *i*) to prepare Ni_2P nanoparticles with hollow and multifaceted structure [113]. The Ni_2P(001) crystal plane, on which theoretical calculation predicted the excellent electrocatalytic activity, was controlled and exposed in their work. As shown in Fig. 6d, the as-synthesized hollow Ni_2P exhibited HER performance with the overpotential at 20 mA cm^{-2} of 130 mV. Likewise, C. Zhang et al. obtained crystalline $Ni_{12}P_5$ nanoparticles (Fig. 6e), showing the uniform size of 14 ± 2 nm [124]. Using these nanoparticles as electrocatalyst for HER in acidic media, the overpotential to generate the current density of 10 mA cm^{-2} is around 107 mV. The inferior HER activity was also observed on Ni_3P microparticles (Fig. 6f) [118]. The comparison of HER activity on NiP_x with different ratios were carefully studied by Liu et al [101]. The Ni_5P_4 crystals showed much more superior electrocatalytic activity than $Ni_{12}P_5$ and Ni_2P for HER in 0.5 M H_2SO_4 due to higher positive charge of Ni and a stronger ensemble effect of P in Ni_5P_4. Apart from the single-phase nickel phosphides mentioned above, the electrocatalytic properties of biphasic Ni_5P_4-Ni_2P nanosheet arrays have been studied by Liu and co-workers (Fig. 6g) [104]. The biphasic Ni_5P_4-Ni_2P nanosheet shows a low onset overpotential and excellent long-term durability in acidic solution.

3.1.2. Cobalt phosphides

As previously reported, metallic cobalt has been theoretically calculated to have low energy barriers for adsorbed hydrogen atoms [80,125], and therefore Co-based compounds are considered to be promising catalysts for HER. Cobalt phosphide (CoP_x) [102,106,107,110,112,126–135], another important member of the TMP family, has been confirmed to be a highly active and acid-resistant electrocatalyst. Recently, the CoP crystals were extensively studied as catalyst for electrochemical hydrogen evolution. It possesses MnP-type structure, in which the phosphorus atom is surrounded by six cobalt atoms to form a highly distorted triangular prism structure [112]. To date, various CoP nanocrystals with different morphologies, such as nanoparticle [112], nanowire [126] and nanosheet [127] have been designed and synthesized. As shown in Fig. 7a-b, Schaak's group firstly prepared uniform CoP nanoparticles with an average particle size of 13 ± 2 nm through organic phosphorus route (Route *i*) [112]. These CoP nanoparticles supported on the Ti foil demonstrate well HER performance with overpotential of 85 mV at the current density of 20 mA cm^{-2} in 0.5 M H_2SO_4. After that, the improved electrocatalytic activity was realized on the CoP nanowires (Fig. 7c-d) in the electrolyte with the pH range from 0 to 14 [126]. Inspired by the advantages, i.e., large surface area, appropriate structural distortion, abundant active sites and high proton/electron transfer efficiency, of two-dimensional (2D) materials [136], Zhang et al. designed and synthesized porous CoP nanosheets (Fig. 7e-f) with a two unit cell-thin thickness (1.1 nm) by phosphidation of Co_3O_4 precursors (Route *ii*) [127]. The as-prepared samples possess a high proportion of CoP (200) crystal face, which have been theoretically proved to be highly active toward the HER [39]. As expected, the porous CoP nanosheets exhibit superb electrocatalytic performance, with a low overpotential of η_{10} = 56 mV and η_{100} = 131 mV, as well as a small Tafel slope of 44 mV dec^{-1} in 0.5 M H_2SO_4 and long-term durability of over 24 h under time-dependent current density test. Additionally, urchin-like CoP nanocrystal (Fig. 7g-h) was also reported as the electrocatalyst to catalyze the hydrogen generation [107].

Other cobalt phosphide phases such as Co_2P [128], CoP_2 [129] and CoP_3 [130] nanomaterials have also been reported as the HER electrocatalysts. S. Chen and co-workers successfully prepared porous CoP_3 concave polyhedron structures through two steps, involving the transformation of Co-MOFs to porous Co_3O_4 and the subsequent procedure of Co_3O_4 (Route *ii*) [130]. The resulting material displayed outstanding electrocatalytic performance for the HER with a small overpotential of η_{10} = 78 mV in 0.5 M H_2SO_4 and showed a high stability in all-pH solutions. The work by N. Li's group is an exemplary report for being able to successfully synthesize a nanohybrid structure of carbon wrapped Co_2P nanoparticles(Co_2P@C) on carbon cloth (Fig. 8a-c) [128]. Benefitted from the feature of nanohybrid structures, the as-synthesized Co_2P@C showed excellent conductivity and abundant active sites toward the HER, and exhibited low onset overpotential of 42 mV and overpotential of η_{100} = 179 mV in 0.5 M H_2SO_4 (Fig. 8d). Similarly, a nanocomposite structure of reduced graphene oxide (RGO) supporting CoP_2 nanoparticles (CoP_2/RGO) was reported by J. Liu and co-workers (Fig. 8e-f) [129]. The synergistic effect of CoP_2 nanoparticles of high intrinsic electrochemical activity and graphene of excellent electrical conductivity further enhances the electrochemical performance. When tested for HER, the CoP_2/RGO displayed higher activities, requiring the overpotential of η_{10} = 88 mV and Tafel slope of 50 mV dec^{-1} in 1.0 M KOH (Fig. 8g), than that of bulk CoP_2.

3.1.3. Iron phosphides

With the similar structure with the active sites in [FeFe] hydrogenases, iron phosphide (FeP_x) was thought to be highly active for electrochemically generating hydrogen gas [91,111,114,120,137]. And the abundant resource of iron atoms render FeP_x low cost for industrial application. Superior electrocatalytic activity for hydrogen evolution has been realized based on FeP [111], Fe_2P [138] and Fe_3P [138]. Whitmire et al. synthesized phase-pure Fe_xP (x = 1, 2, 3) thin films (Fig. 9a-c) via chemical vapor deposition (CVD) to study their comparative catalytic activities [138]. Their HER activity follows the trend FeP < Fe_2P < Fe_3P with the lowest overpotential of η_{10} = 49 mV for Fe_3P. From the DFT calculations (Fig. 9d-f), the hydrogen binding strength on the surface of Fe_3P (100), Fe_2P (100), and the Fe-terminated $FeP_{Fe\text{-}t}$ (011) revealed that hydrogen universally prefers binding to Fe-rich region, resulting in higher hydrogen coverages on Fe-rich Fe_2P and Fe_3P surface for the incoming HER process. Additionally, FeP nanoparticles with uniform hollow sphere structure were prepared to realize the electrocatalytic HER activity in different media [111]. And Sun's group reported that the low onset overpotential of 16 mV and η_{10} of 55 mV could be achieved upon FeP nanowires on Ti foil in 0.5 M H_2SO_4 [114]. A drawback that has to be mentioned here is the fact that FeP demonstrate a poor stability due to the easy corrosion occurred on its surface in acidic solution.

In order to improve the long-term durability of HER electrocatalyst under harsh reaction conditions, Y. E. Sung and co-workers prepared carbon-shell-protected FeP nanoparticles (NPs) through the simultaneous phosphidation and carbonization method (Fig. 10a) [139]. During the thermal treatment, chemical conversion from polymer coating to carbon shell and Fe_2O_3 nanoparticles to FeP nanoparticles occurs at the same time. As expected, the long-term durability of FeP nanoparticles with a carbon shell was realized, even though FeP nanoparticles with or without carbon shell showed a consistent activity (Fig. 10b-c). As shown in Fig. 10d-e, the EXAFS analysis showed that the uncoated FeP NPs is slightly shifted to the left after 5000 potential cycles, while the carbon-shell-coated ones show little difference. These results confirm the carbon shell could effectively prevent the FeP from oxidation and corrosion.

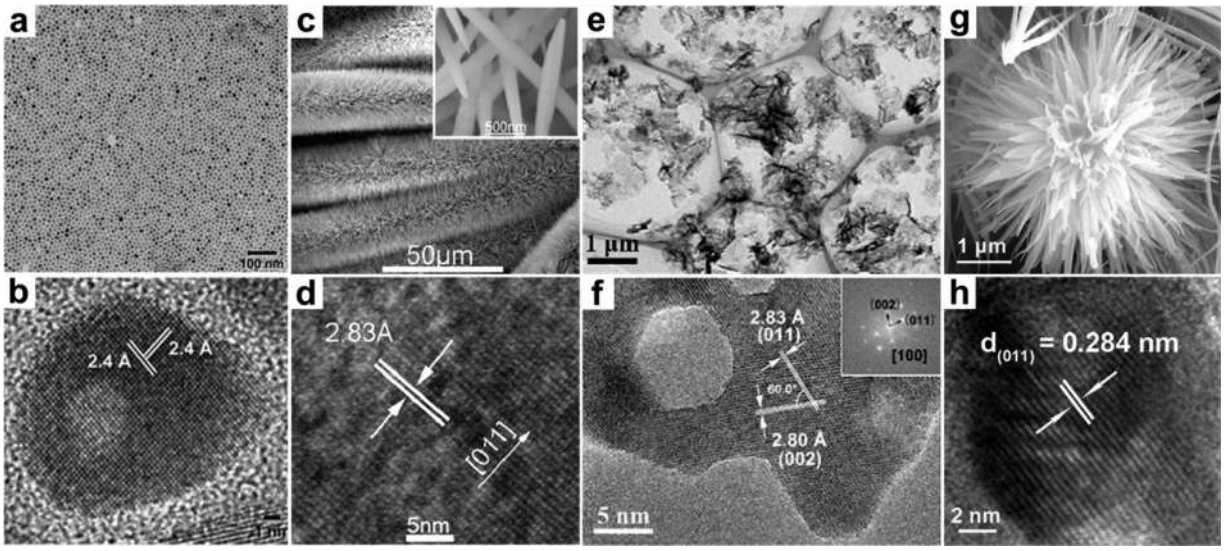

Fig. 7. (a) TEM and (b) HRTEM images of CoP nanoparticles. (Reproduced from Ref. [112] with permission from John Wiley & Sons, Inc., Copyright 2014). (c) SEM image of CoP nanowire arrays on carbon cloth and (d) HRTEM image of CoP nanowire. (Reproduced from Ref. [126] with permission from American Chemical Society, Copyright 2014). (e) TEM and (f) HRTEM images of ultrathin porous CoP nanosheets. (Reproduced from Ref. [127] with permission from The Royal Society of Chemistry, Copyright 2017). (g) SEM and (h) HRTEM images of urchin-like CoP nanocrystals. (Reproduced from Ref. [107] with permission from John Wiley & Sons, Inc., Copyright 2015).

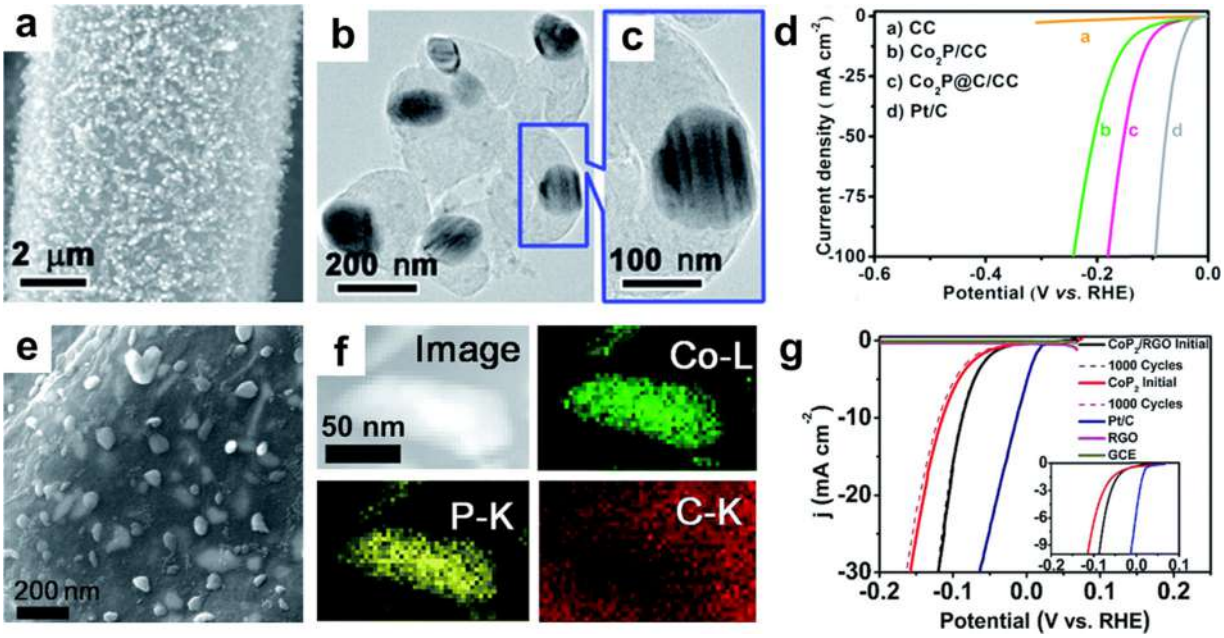

Fig. 8. (a-c) SEM and TEM images of Co_2P@C on carbon cloth. (d) Polarization curves for various catalysts in 0.5 M H_2SO_4. (Reproduced from Ref. [128] with permission from The Royal Society of Chemistry, Copyright 2017). (e-f) SEM, STEM and corresponding EDX elemental mapping of CoP_2/RGO. (g) Polarization curves for various catalysts in 1.0 M KOH. Inset: enlarged region from 0 to -10 mA cm^{-2}. (Reproduced from Ref. [129] with permission from The Royal Society of Chemistry, Copyright 2016).

3.1.4. Copper phosphides

As to the copper phosphide, the Cu_3P were considered for electrocatalytic HER [140–147]. A Cu_3P unit cell is alternately stacked with four different sites of copper and one kind of phosphorus to form the deformed triangular prism (Fig. 11a) [140]. Based on the theoretical calculations, its (110) surface is usually exposed and acts as the active site for HER. This result is also consistent with the experimentally reported result [141]. In this regard, X. Sun's group directly grew self-supported Cu_3P nanowires on copper foam (Cu_3P NW) by hypophosphite-based reaction route (Route *ii*) [142]. The Cu_3P electrode showed moderate HER performance with overpotential of η_{10} = 143 mV and Tafel slope of 67 mV dec^{-1} in 0.5 M H_2SO_4. P. Du et al. recently prepared Cu_3P nanosheet (Cu_3P NS) on nickel foam (Fig. 11b-c) [141]. The Cu_3P NS exhibited high-efficiency electrocatalytic performance toward HER in 1.0 M KOH with overpotential of η_{10} = 105 mV and Tafel slope of 42 mV dec^{-1} (Fig. 11d). Meanwhile, the overpotential was negligibly decreased under a fixed catalytic current density of 10 mA cm^{-2} for 24 h (Fig. 11e), confirming its robustness for hydrogen evolution with a long time. The electrolysis experiment produced ~1200 μmol H_2 within one hour, revealing the high faraday efficiency of 98% (Fig. 11f).

To be noted, the Cu_3P were explored as HER electrocatalyst, but was

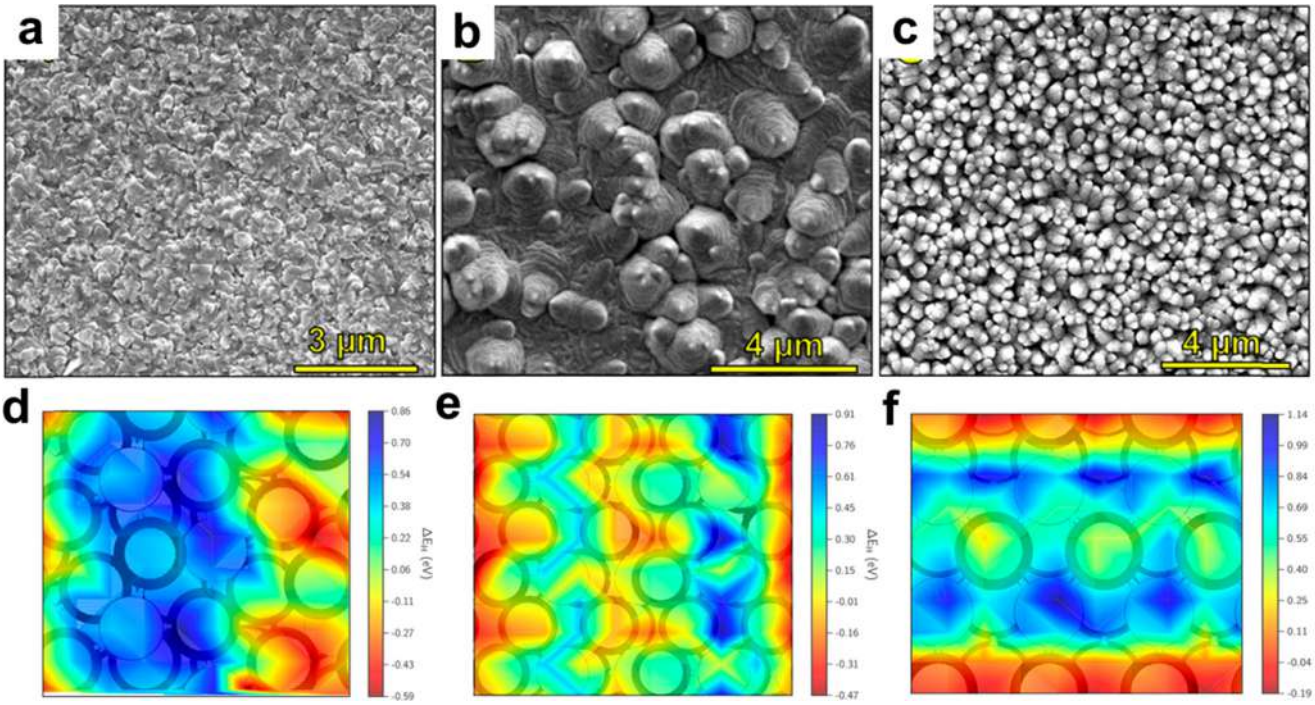

Fig. 9. SEM images of (a) FeP, (b) Fe_2P and (c) Fe_3P on FTO. Contours of H binding strength on the surfaces of (d) $Fe_3P(100)$, (e) $Fe_2P(100)$ and (f) $FeP_{Fe\text{-}t}(011)$. Fe atoms are depicted with thick boundaries, while P atoms are depicted with thin boundaries. Red areas indicate strong binding, while blue represents areas of weak binding. (Reproduced from Ref. [138] with permission from American Chemical Society, Copyright 2018).

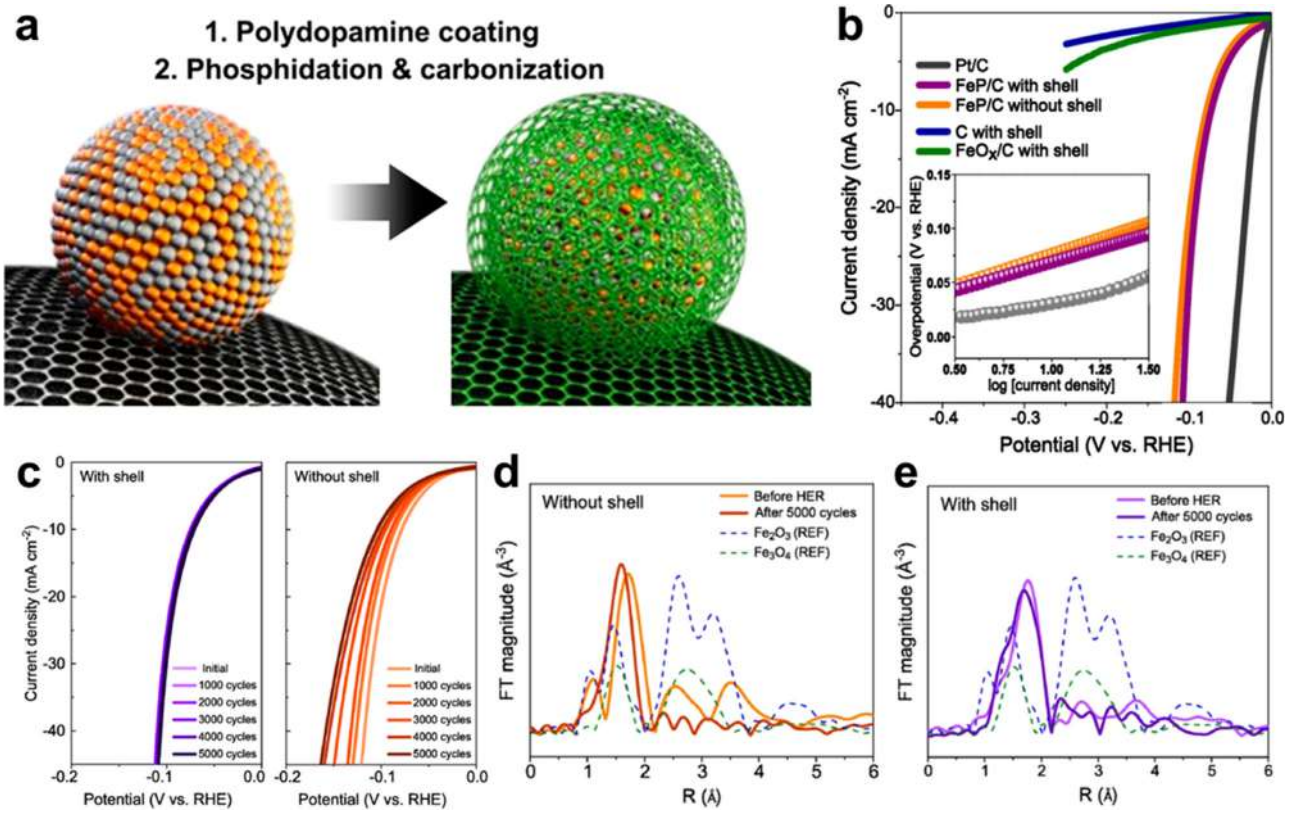

Fig. 10. (a) Schematic representation of carbon-shell-coated FeP nanoparticles preparation. (b-c) Polarization curves of FeP with and without a carbon shell in 0.5 M H_2SO_4. The corresponding Tafel plots are shown in the inset of (b). (d-e) Extended X-ray absorption fine structure (EXAFS) analysis of FeP nanoparticles without and with the carbon shell. (Reproduced from Ref. [139] with permission from American Chemical Society, Copyright 2017).

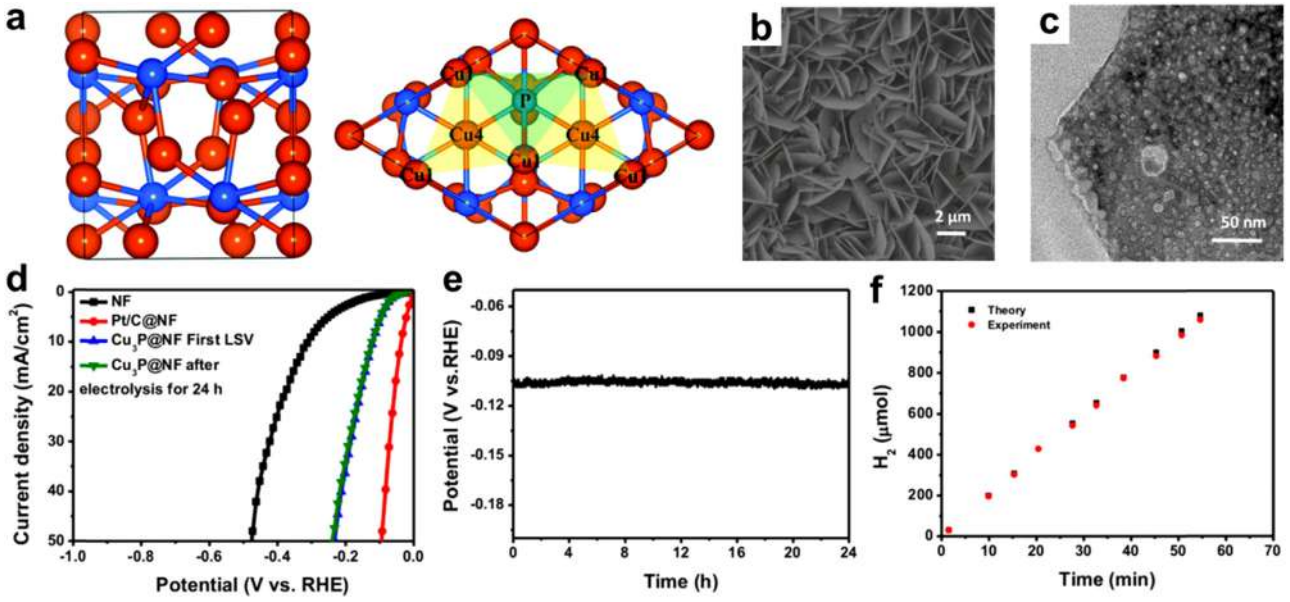

Fig. 11. (a) Side and top views of bulk Cu_3P crystal. Orange and blue spheres denote Cu and P atoms, respectively. (Reproduced from Ref. [140] with permission from The Royal Society of Chemistry, Copyright 2018). (b-c) SEM and TEM images of Cu_3P nanosheet. (d) Polarization curves of various catalysts in 1.0 M KOH. (e) Chronoamperometry measurement of Cu_3P@NF electrode at the current density of 10 mA cm^{-2} in 1.0 M KOH. (f) Hydrogen evolution over time versus theoretical quantities using the Cu_3P@NF electrode for the hydrogen evolution reaction. The applied potential was −0.3 V vs RHE. (Reproduced from Ref. [141] with permission from American Chemical Society, Copyright 2017).

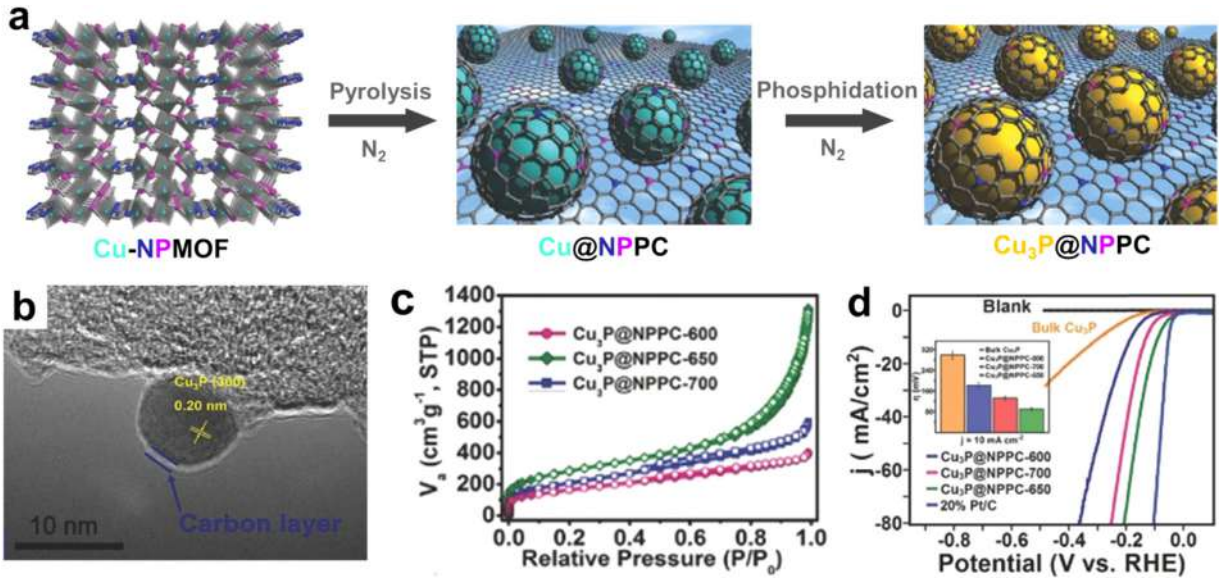

Fig. 12. (a) Schematic illustration of the preparation of the Cu_3P nanoparticles coated by N, P-codoped porous carbon matrix (Cu_3P@NPPC). (b) HRTEM image of Cu_3P@NPPC. (c) N_2 sorption isotherms of the Cu_3P@NPPC catalysts at 77 K. (d) Polarization curves of Cu_3P@NPPC for HER in 0.5 M H_2SO_4. Inset: the error bar of HER activities for Cu_3P@NPPC catalysts. (Reproduced from Ref. [143] with permission from John Wiley & Sons, Inc., Copyright 2018).

still inferior to extensively studied Ni [49], Co [132] or Fe [148] based TMP electrocatalysts. Thus, in order to further enhance the HER activity, S. Zang et al. fabricated hierarchical Cu_3P nanoparticles coated by a N, P-*co*-doped carbon shell (Cu_3P@NPPC) (Fig. 12a-b) to realize the outstanding HER activity [143]. As shown in Fig. 12c, this hierarchical Cu_3P@NPPC structure displayed a large specific surface area of 1004.7 m^2 g^{-1}. Expectedly, Cu_3P@NPPC cathode exhibited excellent HER activity with the overpotential of η_{10} = 89 mV (Fig. 12d) and long-term durability after 3000 potential cycles in 0.5 M H_2SO_4. The porosity of Cu_3P@NPPC could effectively promote the transportation of reactants and products, as well as provide additional active sites for electrocatalytic reaction. Additionally, another heterostructure (i.e., NiCoP@Cu_3P) was constructed for enhancing HER performance by utilizing the synergistic effect between Cu_3P and NiCoP [144].

3.1.5. *Molybdenum phosphides*

Given the superior electrochemical activity for hydrodesulfurization (HDS) reaction [44,45], molybdenum phosphide (MoP_x) has attracted extensive attention as an efficient HER electrocatalyst [100,108,149–157]. Of note, it also possesses Pt-like electronic structure [62,100,158], suggesting that it will be the potential candidates for efficient HER performance. X. Wang's [100] and X. Sun's [108] groups experimentally verified the considerable electrocatalytic activity of MoP compound toward HER. The MoP electrocatalyst was synthesized using phosphate-based reaction strategy (Route *ii*). After evaluating the HER activity of Mo, Mo_3P and MoP [100], they found that the

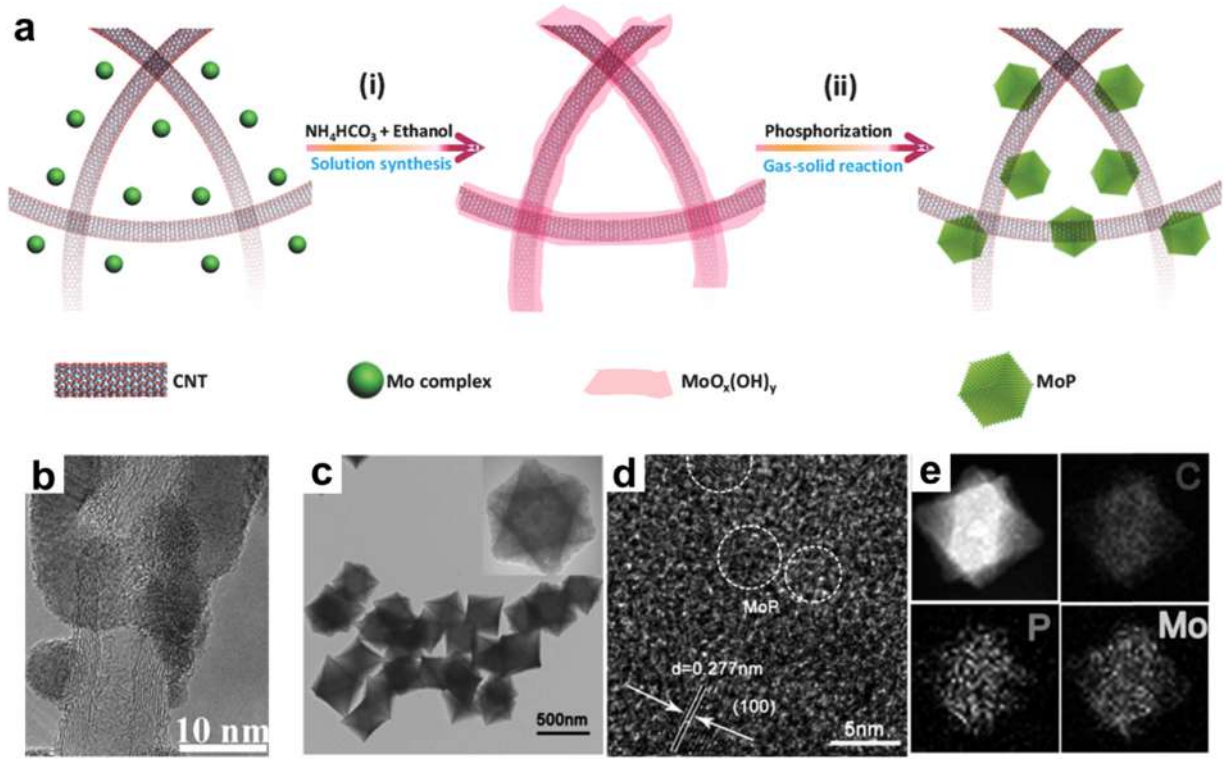

Fig. 13. (a-b)Schematic illustration of the preparation and the TEM image of the MoP/CNT hybrid. (Reproduced from Ref. [149] with permission from John Wiley & Sons, Inc., Copyright 2018). (c-e) TEM, HRTEM images and energy-dispersive X-ray spectroscopy (EDS) elemental mapping of MoP@PC. (Reproduced from Ref. [150] with permission from John Wiley & Sons, Inc., Copyright 2016).

phosphorization could modify the property of Mo metal and lead to the distinct HER performance under various phosphorization degree. DFT calculations indicated that a good "H delivery" system formed on MoP endowed it nearly zero binding to H atoms. The P atoms acted as "hydrogen deliverer", which adsorb hydrogen at low coverage whilst desorb hydrogen at high coverage. Of note, This MoP catalyst showed high activity to HER in both acidic and alkaline media. Coincidentally, the Tafel slope of 54 mV dec^{-1}, along with the overpotential of 180 mV at 30 mA cm^{-2}, in 0.5 M H_2SO_4 was obtained.

Unfortunately, MoP formed at high temperature phosphorization usually cause the agglomeration and sintering of MoP nanostructures [159,160]. To solve this problem, constructing heterstructures based on MoP is a crucial way. For example, Wang et al. used hypophosphite-based reaction strategy (Route *ii*) to successfully fabricate highly dispersed, small-sized, and well-crystallized MoP nanoparticles onto carbon nanotube (CNT) sidewalls [149]. Fig. 13a demonstrates the growth process of MoP/CNT heterostructured catalyst. As shown in Fig. 13b, the well-crystallized MoP nanoparticles were uniformly bonded to the sidewalls of CNT and the introduction of CNT effectively inhibited the aggregation of MoP nanoparticles. The resulting MoP/CNT exhibited superior electrocatalytic activity of HER and excellent stability in pH-universal media. To further improve the electrochemical HER activity and structural stability of MoP, Li and co-workers developed a MOF-assisted strategy to synthesize porous carbon supported MoP nanoparticle (MoP@PC) [150]. The commercial MoO_3 were confined in the ultrafine pores of UIO-66 MOF via simple high-temperature heating process, and sequentially made to pass through in situ carbonization, etching, and phosphorization reactions to form a MoP@PC nano-octahedrons hybrid. As shown in Fig. 13c-e, the well-defined octahedral morphology of MoP@PC was prepared. The lattice fringes of MoP nanoparticles with the *d* spacing distance of its (100) planes are clearly observed. Compared with other catalysts, like MoO_2@PC, Mo_2C@PC, and MoN@PC, as-obtained MoP@PC hybrid not only exhibited excellent HER activity, but also demonstrated outstanding stability emanated from protection of carbon shell.

3.1.6. Tungsten phosphides

Analogous to the molybdenum phosphides, tungsten phosphides are also among the active HDS catalysts reported to date [161]. Thereinto, WP and WP_2 were extensively studied as catalysts for HDS [161]. These works indicate that tungsten phosphides will be the alternatives to electrochemically catalyze the water splitting for hydrogen gas [162,163]. In 2014, Mcenaney et al. reported the amorphous WP nanoparticles deposited onto Ti foil substrates as an efficient HER electrocatalyst [164]. Then, a novel three-dimensional WP nanorod arrays on carbon cloth prepared by Sun's group showed superb stability in HER process [109]. And there was no obvious degradation in activity within continuous testing of 70 h. Under the same situation, Sun's group also synthesized phosphorus-enriched tungsten diphosphide (WP_2) submicroparticles with MoP_2-type structure [116]. It revealed remarkable HER performance with η_{10} = 161 mV in 0.5 M H_2SO_4. Moreover, the self-supported WP_2 nanowires (Fig. 14a) were then synthesized by Wang and co-workers on carbon cloth via in-situ topological transformation with hypophosphite-based reaction strategy (Route *ii*) [119]. As shown in Fig. 14b, this WP_2 crystallize demonstrates the monoclinic $NbAs_2$ structure type. The DFT calculations of its electronic band structure and density of state (DOS, Fig. 14c) showed the overlapped conduction (CB) and valence band (VB) at the Fermi level, suggesting its metallic character and excellent electronic conductivity. The resulting electrode showed superior catalytic activity (Fig. 14d) and stability which can be exemplified from the low overpotentials of η_{10} = 109 mV and a small Tafel slope of 56 mV dec^{-1} in acidic media. What's more, the hybrids based on tungsten phosphides are popular. In this regard, Mu et al. developed a facile synthesis of well-crystallized WP nanoparticles embedded in a nitrogen-doped carbon matrix (WP NPs@NC) by high temperature solid-phase reaction of ammonium phosphate (Route *ii*) to improve HER activity [165]. As demonstrated in Fig. 14e, the WP NPs with the size < 5 nm is

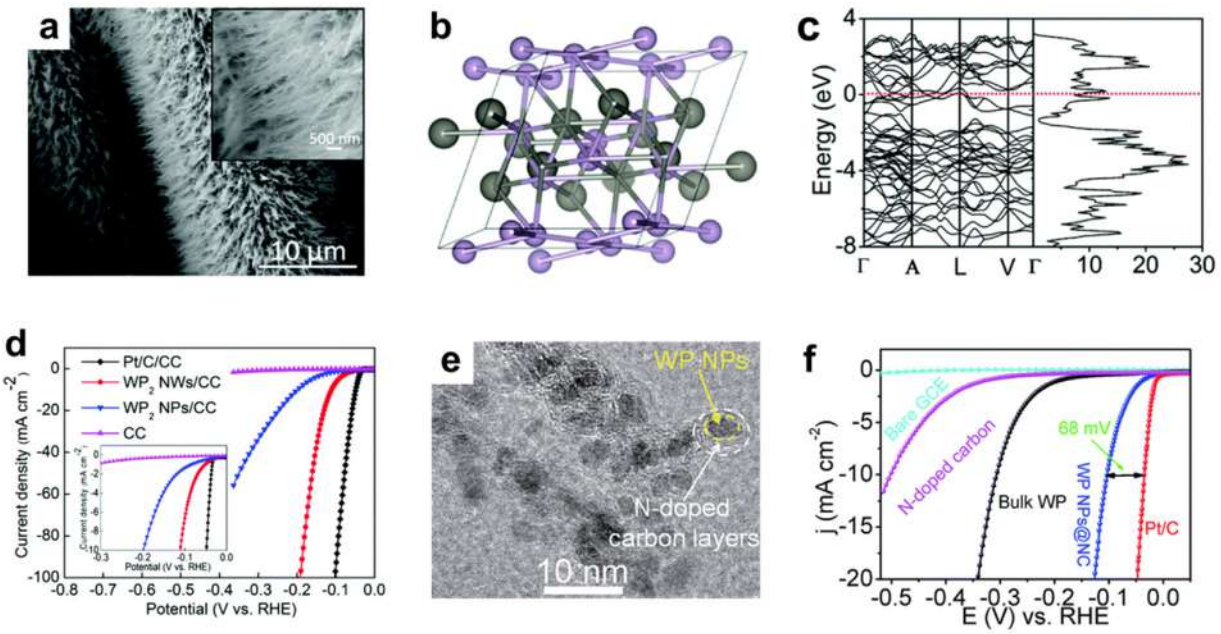

Fig. 14. (a) SEM images of WP_2 nanowires on carbon cloth. (b) Crystal structure of WP_2 (W atom: gray sphere, P atom: purple sphere). (c) Electronic band structure (left) and density of state (right) for WP_2. (d) Polarization curves for various catalysts in 0.5 M H_2SO_4. (Reproduced from Ref. [119] with permission from The Royal Society of Chemistry, Copyright 2016). (e) TEM image of WP NPs@NC. (f) Polarization curves for various catalysts in 0.5 M H_2SO_4. (Reproduced from Ref. [165] with permission from The Royal Society of Chemistry, Copyright 2016).

encapsulated by ultrathin carbon shell. And this electrocatalyst exhibited enhanced HER performance (Fig. 14f) with a low overpotential of η_{10} = 102 mV in 0.5 M H_2SO_4 and superior durability (4 days). More importantly, the WP NPs@NC also showed remarkable electrocatalytic activity and stability toward the HER in both neutral and alkaline conditions.

3.1.7. Other metal phosphides

Based on the aforementioned metal phosphides, the tuning of their component could effectively improve the catalytic activity. In this regard, the cation and anion substitution are widely adopted [166–176]. In order to obtain insights into the trends and guidelines for systematically improving their intrinsic activity, T. F. Jaramillo et al. utilized experimental-theoretical approach to study the relation between HER activities, ΔG_H* and various TMPs [39]. Fig. 15a and b plot the normalized current density of various TMP catalysts measured at the overpotential of 100 mV and the average TOF *vs* the calculated ΔG_H* respectively, yielding volcano shapes. The mixed TMP, $Fe_{0.5}Co_{0.5}P$, showed a near-optimal ΔG_H* with highest current density and average TOF. Their work reveals that the binary metal composition could regulate the electronic structure of the electrocatalysts to boost the intrinsic activity. Later, Chen et al. synthesized a series of bimetallic $Fe_xCo_{1-x}P$ ($0 < x < 1$) nanowire arrays on carbon cloth (Fig. 15c) as HER electrocatalyst and confirmed that $Fe_{0.5}Co_{0.5}P$ possessed Pt-like electrocatalytic performance with the overpotential of only η_{10} = 37 mV in 0.5 M H_2SO_4 (Fig. 15d) and superior long-term electrochemical stability for at least 100 h (Fig. 15e) [177]. Furthermore, they also found that hydrogen production activity of $Fe_xCo_{1-x}P$ nanowire is strongly related to Fe substitution ratio. DFT calculations indicated that the proper Fe substitution in the electrocatalyst would result in more optimal ΔG_H* Fig. 15f). The ΔG_H value of $Fe_{0.5}Co_{0.5}P$ is closest to zero with a highest electrocatalytic activity toward HER, which is consistent with Jaramillo's work.

Additionally, the substitution of phosphorus atoms with sulfur atoms in metal phosphides to form transition metal phosphosulphides (TMPS) is considered to be an effective way to improve the electrocatalytic HER activity. In this regard, some TMPS electrocatalysts, such as CoPS and MoPS [178–181] have been designed and synthesized. The S substitution could induce the shift of *d*-band center due to the difference in electronegativity of S and P atoms. After introducing S into the surface region of MoP films or MoP for getting MoP|S films [180] and $MoS_{2(1-x)}P_x$ solid solution [181], the HER performance is effectively enhanced comparing to the pristine MoP electrocatalyst. To develop a non-noble metal based catalyst with Pt-like electrocatalytic activity for HER, Jin et al. reported a combined experimental and theoretical approach to study highly active nanostructured pyrite-type cobalt phosphosulphide (CoPS) as electrocatalyst [179]. Different with CoS_2 consisting of Co^{2+} octahedral and S_2^{2-} dumbbells, the cubic crystal structure of CoPS has a smaller lattice constant than CoS_2 and a composition of Co^{3+} octahedral and dumbbells with a homogeneous distribution of P^{2-} and S^- atoms (Fig. 16a). From the theoretical calculation, the adsorbed atomic hydrogen at the Co sites of CoPS were more favorable than that of CoS_2, and the ΔG_H of adsorption hydrogen at the adjacent Co sites became spontaneous and almost thermoneutral (Fig. 16b), which is attributed to the reduction of Co^{3+} to Co^{2+} on hydrogen adsorption at adjacent open P sites. Therefore, the resulting CoPS electrocatalyst exhibited superb HER performance with a low overpotential of η_{10} = 48 mV and long-term stability over 36 h in 0.5 M H_2SO_4 (Fig. 16c-d). Similarly, Wang et al. also reported cobalt phosphosulfide nanoparticles (CoP|S) grown on carbon nanotubes with high activity and stability for hydrogen generation [178]. Further study found that the incorporation of P can observably impact the nature of chemical bonding between Co and S/P. As demonstrated in Fig. 16e, the phosphosulfides ($CoS_{2-x}P_x$) were more stable in the cubic structure when the S atoms are replaced by P. And the P substitution could give rise to the depletion of antibonding e_g^*, thereby strengthening the chemical stability of the catalyst during the hydrogen generation (Fig. 16f).

3.2. Transition metal carbides

Transition metal carbides (TMCs) constitute diverse class of materials with a vast interest over the past years due to their appealing properties such as high conductivity, superior chemical stability and

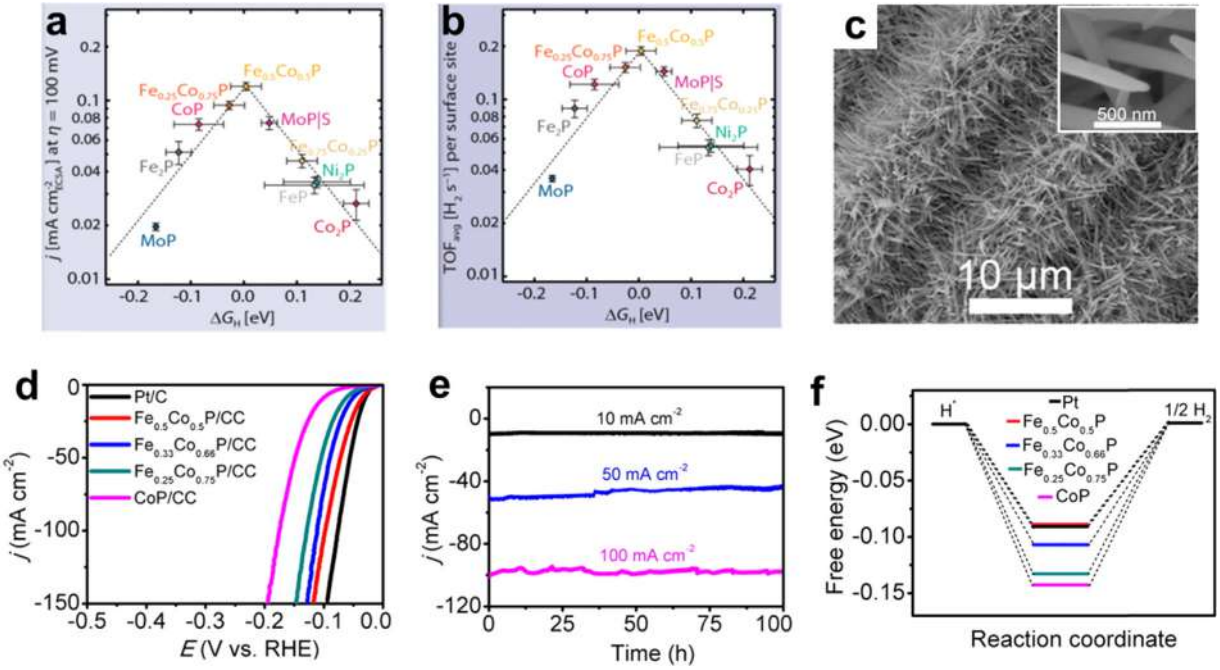

Fig. 15. (a-b) Activity volcano plots of the HER electrocatalysts showing the ECSA normalized current density and the average TOF at Z = 100 mV as a function of ΔG_H. (Reproduced from Ref. [39] with permission from The Royal Society of Chemistry, Copyright 2015). (c) SEM images of $Fe_{0.5}Co_{0.5}P$ on carbon cloth. (d) Polarization curves for various catalysts in 0.5 M H_2SO_4. (e) Time-dependent current density curves of $Fe_{0.5}Co_{0.5}P$ at fixed different overpotentials. (f) Free energy diagram of HER under favorable Co site of hydrogen coverage on surface of $Fe_xCo_{1-x}P$. (Reproduced from Ref. [177] with permission from American Chemical Society, Copyright 2016).

thermal stability [182–189]. These materials are also known as interstitial alloys as the carbon atoms occupy the interstitial positions. Most transition metals, except for the second and third row group 9–10 metals (e.g., Rh, Ir, Pd, and Pt), form carbides with significant variation in their crystal structure. The bonding arises from the interaction of 2*s* and 2*p* orbitals of the carbon with *d* orbital of the transition metal. The parent metal structure varies from body-centered cubic (*bcc*) to hexagonal closed packed (*hcp*) to face-centered cubic (*fcc*) with increasing

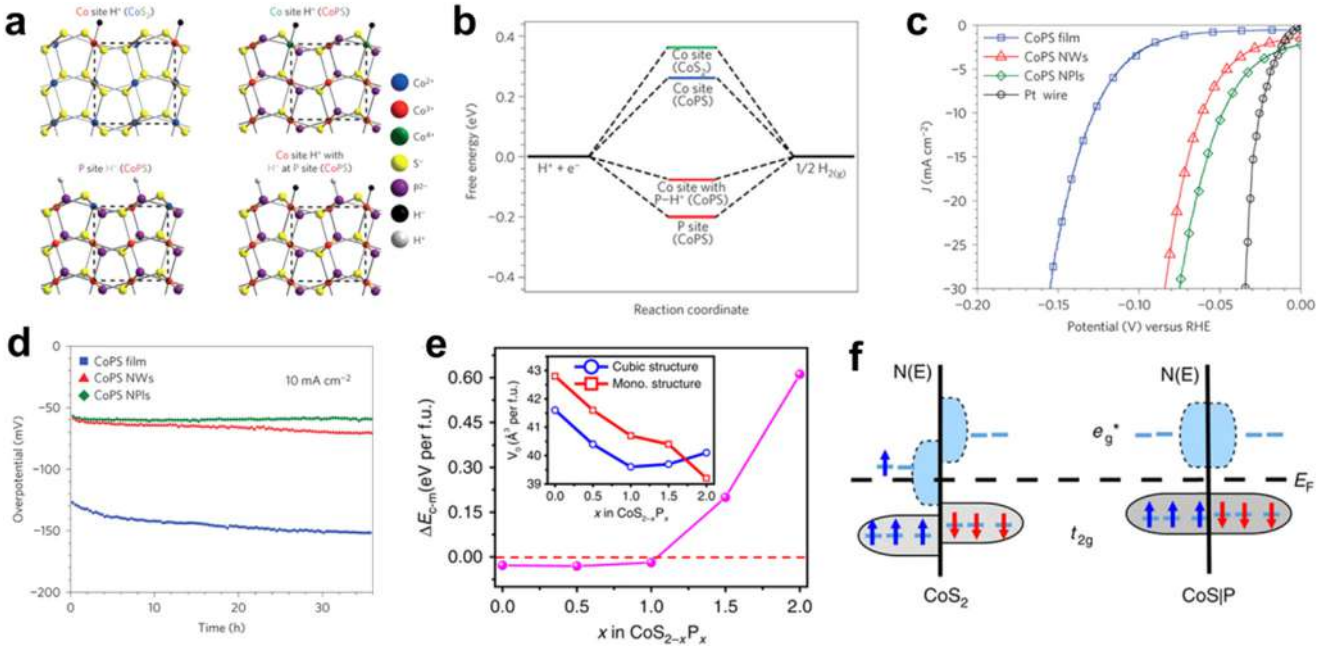

Fig. 16. (a) Schematic structural representations for hydrogen adsorption (H*) at the Co site on the {100} surface of CoS_2, and at the Co site (top left), P site (top right), and Co site (bottom left) after hydrogen adsorption (H*) at the P site (bottom right) on the {100} surface of CoPS. (b) Free-energy diagram of CoPS. (c) Polarization curves after *iR* correction show the catalytic performance of the CoPS electrodes compare that of Pt wire. (d) Long-term stability test for CoPS electrodes at a current density of 10 mA cm^{-2}. (Reproduced from Ref. [179] with permission from Nature Publishing Group, Copyright 2015). (e) The energy difference per formula unit between the cubic and monoclinic phases as a function of the P substitution extent obtained from DFT calculations. (g) Conceptual energy level diagrams of the frontier molecular orbitals of pyrite-phase CoS_2 and CoS|P derived from the calculated electronic structures. Reproduced from Ref. [178] with permission from Nature Publishing Group, Copyright 2016).

Table 3
Crystal structures of reported transition metal carbides and their position in the periodic table.

Position in the periodic table	Parent metal	Carbide	Crystal structure	Ref.
Group 4	Ti	TiC	Cubic	[354–356]
Group 5	V	VC	Cubic	[230]
	Nb	NbC	Cubic	[230]
	Ta	TaC	Cubic	[230]
Group 6	Cr	CrC	Cubic	[357]
		Cr_3C_2	Cubic	[357]
		Cr_7C_3	Orthorhombic	[357]
		$Cr_{23}C_6$	Hexagonal	[357]
	Mo	Mo_2C	Cubic	[224,229,358]
	W	WC	Orthorhombic	[357]
		W_2C	Hexagonal	[229]
		W_3C	Hexagonal	[229]

the *sp* electrons. Elements to the left in the periodic table adopt the *bcc* structure (e.g., Nb, Ta, Mo and W), but those in the center prefer the *hcp* structure (e.g., Tc, Re, Ru and Os) and furthest to the right prefer the *fcc* structure (e.g., Rh, Ir, Pd and Pt) [190–192]. When the carbon atom is made to occupy the interstitial position, it results in the expanding of *d*-orbitals in the metal giving rise to the formation of interstitial alloys [193]. The occupancy of the metal's *d*-band governs the metal-to-carbon ratio of the incoming metal carbide. Accordingly, transition metals in Group 4 and 5 have incompletely filled bands capable of accommodating high amount of *sp*-carbon orbitals mostly resulting in the formation of MC (e.g., TiC, VC, NbC and TaC). As we do the same analysis for other groups, M_2C (e.g., Mo_2C and W_2C) occurs for transition metals in Group 6 while M_3C (e.g., Mn_3C, Fe_3C, Co_3C and Ni_3C) is the preferred stoichiometry for the transition metals in Group 7 and 8. Table 3 shows that there is an increasing trend of M-to-C ratio moving to the right in the periodic table, suggesting the difficulty of accommodating carbon atoms into the metals of the right side. Thus, those metals in Group 9–10 form unstable carbides [182,194].

Many of the reported carbides are of in low surface areas, defying their wide spread applications in catalysis. Moreover, char contamination is the frequently appearing problem in synthesizing metal carbides. Carbides with char contaminants exhibit poor catalytic performance as the impurities would block the cavities and active sites that are essential for catalysis [195]. The synthetic method should enable the utmost exposure of active sites on the surface to realize efficient catalysis. In this regard, pyrolysis of metal carbonyl compounds, or direct reaction of metal/metal oxide with carbon source, as in the chemical vapor deposition (CVD) method, are among the commonly employed methods involving solid-solid reactions or gas-solid reactions to realize high surface area metal carbide catalysts. As mentioned above, the metal to carbon molar ratio is of crucial in determining the stability and catalytic activity of the incoming metal carbide. Thus, governing parameter has to be carefully identified and tuned in the synthesis method to fabricate the desired ratio. As such, the type of precursors used, temperature of the reaction, and gas flow rate are known to be the most prevailing factors in controlling the growth of metal carbides. The work by Loh et al. shows the effect of gas flow rate in tuning the structure and composition of Mo_2C [196]. Different flow rates of methane gas impart different forms of product.

Apart from CVD method, many researchers have utilized the method of carburizing the metal precursors in organic compounds, such as aniline [197], melamine [198], dopamine [199], etc. and inorganic compounds like g-C_3N_4 [200] and carbon nanotube [201]. These strategies involve first formation of a solid solution via dissolving the metal precursors into the selected carbon source followed by calcination at optimum temperature. The diffusion rate of carbon atom away from inorganic sources is relatively slower as compared to organic sources [201]. This can avoid excess carbon deposition and thereby eliminates char contamination. Given the appropriate carbon source and metal precursors used, this approach is preferable to those of gas-phase methods in yielding engineered nanostructured materials and providing a platform to a well dispersed catalyst in supporting substrate [193].

The rationale behind the exploration of HER catalytic activity for

Table 4
Compilation of HER performance based on various transition metal carbide electrocatalysts under different conditions.

Materials	Substrate	Electrolyte	Overpotential (mV)		Tafel slope (mV dec^{-1})	Loading density (mg cm^{-2})	Year	Ref.
			η_{10}	η_{100}				
Mo_2C	CPE	1.0 M KOH	~ 190	–	54	0.8	2012	[224]
Mo_2C nanotubes	GCE	0.1 M KOH	112	–	55	0.75	2015	[61]
MoC_x octahedrons	GCE	0.5 M H_2SO_4	142	~ 240	53	0.8	2015	[51]
MoC_x@C	GCE	0.5 M H_2SO_4	79	–	56	0.354	2015	[50]
MoC_x/C	GCE	0.5 M H_2SO_4	135	–	62	0.6	2018	[198]
Mo_2C/GR	GCE	0.5 M H_2SO_4	236	–	73	–	2017	[196]
Mo_2C/CNT-GR	GCE	0.5 M H_2SO_4	130	–	58	~ 0.65	2014	[63]
Mo_2C NPs@C	GCE	0.5 M H_2SO_4	78	–	41	0.25	2015	[200]
Mo_2C@NC	GCE	0.5 M H_2SO_4	124	–	60	~ 0.28	2015	[50]
Mo_2C/NCF	GCE	1.0 M KOH	100	–	65	~ 0.28	2016	[199]
Mo_2C@C NWs	GCE	0.5 M H_2SO_4	89	–	42	1.3	2017	[359]
Mo_2C@NPC/NPRGO	GCE	0.5 M H_2SO_4	~ 34	–	33.6	0.14	2016	[62]
WC_x NWs	Carbon cloth	0.5 M H_2SO_4	118	~ 175	55	1.08	2017	[360]
N-WC-nanoarray	Carbon fiber	0.5 M H_2SO_4	89	~ 180	75	10	2018	[209]
WC-CNTs	–	0.1 M KOH	103	–	106	–	2015	[213]
WC@NPC	GCE	0.5 M H_2SO_4	51	–	49	0.209	2017	[212]
WC@CNs	Graphite felt	1.0 M H_2SO_4	65	~ 150	61	–	2016	[210]
W_2C@NC	GCE	0.5 M H_2SO_4	89	–	53	3.5	2017	[216]
WC-G	Ga-W foil	0.5 M H_2SO_4	~ 120	–	38	0.00164	2017	[361]
W_2C/MWNT	GCE	0.5 M H_2SO_4	123	–	45	~ 0.56	2016	[201]
Ti_3C_2 NFs	GCE	0.5 M H_2SO_4	169	–	97	~ 0.3	2018	[231]
V_8C_7 @GC NSs	Ni foam	1.0 M KOH	47	131	34.5	–	2018	[233]
Co_2C NPs	GCE	0.1 M KOH	181	–	89	~ 7.1	2017	[236]
Ni_3C NS	GCE	0.5 M H_2SO_4	178	–	36.5	–	2017	[237]
Fe_3C-GNRs	–	0.5 M H_2SO_4	49	–	46	~ 0.14	2015	[235]
Co_3C-GNRs	–	0.5 M H_2SO_4	91	–	57	~ 0.14	2015	[235]
Ni_3C-GNRs	–	0.5 M H_2SO_4	48	–	54	~ 0.14	2015	[235]

Note: GCE, glassy carbon electrode; CPE, carbon paste electrode.

transition metal carbides is associated with the work of R. B. Levy and M. Boudart who for the first time noted the Pt-like catalytic behavior in WC [202]. It has been suggested that carbon *sp* electrons increased the apparent electron to atom ratio thereby producing a more Pt-like electronic structure. Accordingly, the formation of early transition metal carbides involves the *pd* orbitals hybridization to form covalent bond between the metal and carbon. These bonds constitute both σ and π bonds that are characterized by low lying bonding orbitals, separated by a gap from the antibonding orbitals. The metal σ bonds are located in this gap in which the Fermi energy passes through ultimately producing a Pt and Pd like density of states. It is, thus, believed that the catalytic behavior is emanated from these bonds which gives rise to the predicted coincidence with Pt. Up to now, as collected in Table 4, various metal carbide electrocatalysts are studied as HER electrocatalysts under different conditions. In the following subsections, the HER properties of frequently reported metal carbides will be reviewed.

3.2.1. Tungsten carbides

It has been reported that tungsten carbide and platinum behave similarly as catalysts in various chemical reactions [202]. Spectroscopic investigations proved a solid similarity in the Fermi level electronic density of states (DOS) WC and Pt [203,204]. However, this resemblance is not evident for W *vs* Pt or W *vs* WC. This brought a fundamental basis to extensively explore different forms of tungsten carbide to practically mimic the catalytic activity of Pt [205–208]. Of the various forms of tungsten carbide investigated thus far, tremendous amount of interest have been devoted to WC [209,210]. Unfortunately, the obtained WC catalyst usually suffers from uncontrollable particle agglomeration and additional carbon impurities deposition, the presence of which causes fewer active sites on the catalyst surface. Carbon impurities deposited on the surface could block reactants from accessing active sites and conspicuously reduce or eliminate the electrocatalytic activity of WC [211]. Another problem associated with WC for HER electro catalysis is the sluggish kinetics due to a strong tungsten-hydrogen bond formation [209].

Various strategies were adopted to solve these problems (e.g., agglomeration, carbon contamination and sluggish kinetics). In this regard, the size controlled synthesis of tungsten carbide via a cage-confinement pyrolysis strategy can be considered as a vital importance to inhibit crystal aggregation. This was reported by X. Chen et al. who developed a MOFs-based cage-confinement pyrolysis to obtain tungsten carbide nanoclusters/nanoparticles with sizes ca. 2 nm [212]. Benefitting from the ultra-small size, the WC nanopartciales exhibit a platinum-like catalytic activity for the hydrogen evolution reaction in 0.5 M H_2SO_4 solution. Moreover, the growth of WC on tips of vertically aligned carbon nanotube has also been suggested as a way forward to prevent agglomeration [213]. The direct reaction of tungsten metal with carbon source in hot filament chemical vapor deposition led to the synthesis of single crystal WC with small size (4.5–21.6 nm) and uniform distribution on the carbon nanotubes. Although the performance of the obtained sample, WC-CNT, is not yet comparable to that of platinum, the synthesis strategy opens up a very good avenue to prevent aggregation of nanoparticles and even design heterostructures with other functional materials.

As to the carbon contamination, the work by Y. R. Leshkov et al. can be regarded as a rational approach to simultaneously prevent sintering of the WC nanoparticles while also mitigating surface impurity deposition [214]. They introduced a universal method to synthesize metal-terminated WC nanoparticles in the 1–4 nm range on the high-surface-area supports (Fig. 17a). This unique edge termination was obtained through three key steps including the preparation of WO_x NPs encapsulated within SiO_2 matrix followed by carbonization (CH_4/H_2) of composite particles and removal of SiO_2 shell. A roughly 100-fold enhancement in catalytic performance was noted for such the metal terminated carbides as compared to commercial WC. During the electrolysis of water, hydrogen atoms bind strongly in between two W atoms, defying the release of H_2 from WC(001) [209,215]. This gives rise to the sluggish kinetics mentioned earlier in this topic. In the quest for optimum WC surface that binds H^+ neither too strongly nor too weakly, Sun et al. doped nitrogen in WC to tune the surface energy thereby easing the evolution of H_2 gas [209]. This was achieved via simultaneous reduction, carbonization, and N-doping of pre-synthesized WO_3 nanoarrays (Fig. 17b). The doping of N atoms conspicuously boosts the intrinsic activity of the electrocatalyst at atomic level, tackling the problem of sluggish surface. The superaerophobic nanoarray structure not only exposes more active sites for electrochemical hydrogen generation but also weakens bubble adhesion to facilitate hydrogen release with overpotential of only η_{10} = 89 mV and excellent activity in overall water splitting reaction.

The survey on reports related to tungsten carbide reveals that the focus of researchers exclusively devoted to WC. The other carbide compound—W_2C has received far less attention [216] despite the fact that W_2C is potentially more HER-active than WC from the basis of theoretical calculations [201]. It is usually obtained as a by-product of WC [217]. The scarce reports on W_2C is associated with its thermodynamic unaffordability below 1250 °C [218]. It is the work of Lee's group that communicated the controllable synthesis of W_2C and evaluated the HER performance inspired by the theoretical simulations [201], there are a higher electronic density of states (DOS) at the Fermi level W_2C than WC. They followed in-situ carburization strategy in the presence of multi-walled carbon nanotubes (MWNT) and WO_x precursors under high temperature and low pressure (Fig. 17c). This gave rise to slow diffusion of carbon atom from MWCNT to WO_x thereby ensuring a carbon deficient product (it means favoring the formation of W_2C over that of WC). This material exhibits an excellent HER catalytic activity as can be corroborated from the small onset overpotential of 50 mV and Tafel slope of 45 mV dec^{-1} in 0.5 M H_2SO_4.

It is, therefore, evident that tungsten carbide compounds (W_2C and WC) are among the most promising alternatives to platinum as a HER catalyst. Promising strategies including nanostructuring, optimizing hydrogen binding energy, designing supporting material, etc. have been reported so far for improving their efficiency and reliability.

3.2.2. Molybdenum carbides

Apart from tungsten carbides, molybdenum carbides are among the most extensively investigated for HER with varying properties associated with their phases [186,198,219–223]. Particularly, β-Mo_2C exhibits appealing catalytic properties even in their bulk states [224]. It is also noted that the investigation of four types different phases, derived from their amine–metal oxide derivatives, imparts a trend of β-Mo_2C > γ-MoC > η-MoC > α-MoC_{1-x} in catalytic activities [225]. The performance could be further improved by constructing various nanostructures. Ma et al. reported excellent electrocatalytic activities of β-Mo_2C nanotube and nanosheet architectures, from which maximal utilization of active sites and rapid transport of electrons, were observed [61]. The uniform β-Mo_2C nanocrystallites embedded in a carbon matrix owns porous hierarchical hollow structure in one dimensional network ensuring the enlarged contact surface and facilitates charge/mass transfer during the electrochemical reactions. These features can ultimately be corroborated from the excellent electrocatalytic activity toward HER in both acidic and alkaline solution. Other morphologies, like nanowires [226], have also been reported to demonstrate a remarkably high electrocatalytic activity with their porous surface. For instance, the work by Girault et al. substantiates the prominent role of the nanoporous cavities on Mo_2C nanowires [226]. The hollow nanoporous structure was obtained without aggregation on individual nanowires to ensure a shortened electron transfer distance in the catalytic reaction. Utilizing metal organic frameworks as a precursor to synthesize porous metal carbides (even other porous materials) is emerging strategy offering unique benefits for a wide spread applications. Inspired by this, a remarkably efficient electrocatalysis of HER was observed from porous MoC_x nano-octahedrons obtained via

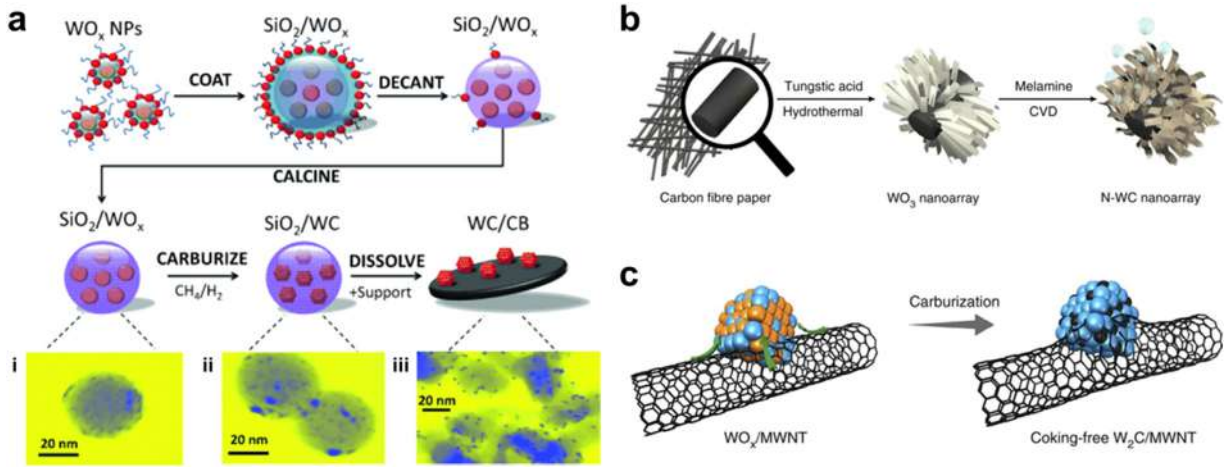

Fig. 17. (a) Representation of the removable ceramic coating method for the synthesis of WC/CB. i-iii) STEM images of silica-encapsulated tungsten oxide NPs, WC NPs and WC NPs supported on carbon black. (Reproduced from Ref. [214] with permission from John Wiley & Sons, Inc., Copyright 2014). (b) Fabrication schematic of N-WC nanoarray electrode for HER. (Reproduced from Ref. [209] with permission from Nature Publishing Group, Copyright 2018). (c) The synthesis of coking-free W_2C/MWNT from WO_x/MWNT for carburization at high temperature and low pressure. (Reproduced from Ref. [201] with permission from Nature Publishing Group, Copyright 2016).

MOFs assisted synthesis method [51]. Interestingly, a uniform porous structure was obtained that are largely originated from the ordered and porous structure of MOFs. The current scenario in this research endeavor focuses on designing appropriate supports for the metal carbides [222,226,227]. The supports provide a vital role in electrocatalytic activities for metal carbides. Of the frequently employed materials as supports, carbon nanotube and graphene are acknowledged for stabilizing the metal carbides nanostructures, providing a large surface area for facile contact with electrolyte and ensuring excellent electron pathway to and from the surface of the metal carbides [63]. In this premises, Lee and co-workers reported a highly active and stable HER electrocatalyst based on carbon nanotube (CNT)-graphene hybrid support for Mo_2C nanoparticles [63]. The structure of the hybrid support not only efficiently alleviates the aggregation of Mo_2C nanocrystals, but also significantly improves the electrical conductivity therein. As a result, the supported Mo_2C exhibited excellent HER performance with a low overpotential of η_{10} = 62 mV and a small Tafel slope of 58 mV dec^{-1} as well as the long-term stability in 0.5 M H_2SO_4. Theoretically, it is believed that super active nonmetal catalytic sites are created following the synergistic interaction between the metal carbide matrix and the adjacent carbon atoms in the support. The emerged catalytic sites are more active than those in the constituents. Theoretical calculations [50] show that the Mo_2C and N dopants in the material synergistically co-activate adjacent C atoms on the carbon nanolayers, creating superactive nonmetallic catalytic sites for HER that are more active than those in the constituents. This was observed in ultrasmall Mo_2C nanoparticles wrapped in N-rich carbon nanolayers (Mo_2C@NC) [50]. Some components from the support material are doped into the metal carbide and initiate electronic coupling leading to a developed synergism. This can be exemplified from the work of Lan and co-workers [62], who fabricated 2D coupled hybrid composed of Mo_2C nanoparticles encapsulated by N, P-codoped carbon shells and N, P-codoped reduced graphene oxide (Mo_2C@NPC/NPRGO). Taking advantage of the synergistic catalytic effects of carbon shell coated Mo_2C NPs, heteroatoms (N, P) are doped into the carbon matrix and unique 2D coupled composite structure (Fig. 18a-d), the resulting catalyst exhibited superb electrocatalytic performance for HER. Similar to commercial Pt/C, only 0 mV for onset overpotential and a low overpotential of η_{10} = 34 mV are required (Fig. 18e), as well as a small Tafel slope of 33.6 mV dec^{-1} in acidic media is recorded.

Furthermore, carbides of molybdenum can, along with those of tungsten based carbides, can be regarded as one of the representative catalysts to replace Pt-group metals. From the basis of their thin film studies, it is observed that pristine Mo_2C is more active towards HER than pristine WC. However, Mo_2C is limited by low electrochemical stability than WC [228,229]. A strategy is, therefore, required to combine these advantageous features (stability from W-C and activity from Mo-C) and realize efficient catalysis. Fabrication of bimetallic $Mo_xW_{1-x}C$ is reported [214]. Owing to its larger Wigner-Seitz radius, Mo atoms compresses the lattice of WC after being inserted to form $Mo_xW_{1-x}C$. This gives rise to modulation of the *d*-band surface DOS and hence establishing enhanced catalysis [214].

3.2.3. Other metal carbides

The fourth period (3*d*) metal elements are known to be the highest abundance and lowest-priced elements. Thus, their corresponding carbide compounds should be worthy of more attention as the HER catalysts. However, very few investigations have been carried out on fourth period metal carbides (e.g., Ti, V, Cr, Fe, Co, Ni) due to their poor electrochemical activity and instability, as well as limited synthetic approaches [230]. Starting our discussion with Ti based carbides, one can see that MXene nanofibers of Ti_3C_2 has been elucidated as high surface area electrocatalyst [231]. Compared to traditional Ti_3C_2 flakes, the as-synthesized Ti_3C_2 nanofiber delivered a much higher specific surface area and exposed more active sites for HER activity. As a result, the obtained Ti_3C_2 nanofiber exhibited an enhanced hydrogen production activity with an overpotential of η_{10} = 169 mV in 0.5 M H_2SO_4 solution. Moreover, the comparison made among nine carbides of transition metals, including TiC, V_8C_7, HfC, ZrC, Cr_3C_2, Nb_4C_3, WC, Mo_2C, reveals that Mo_2C, WC, and V_8C_7 deliver particularly enhanced HER activity compared with others [232]. Inspired by this, Y. Wang et al. designed a graphited-carbon enveloped single-crystal interweaved V_8C_7 nanosheets on nickel foam (V_8C_7 @GC NSs) as an efficient HER electrocatalyst (Fig. 19a-c) [233]. In contrast with conventional pure vanadium carbide [230], V_8C_7 @GC NSs contains a 12.5% of carbon sites that are not filled. Therefore, in and around the defect of carbon sites, the redundant electrons are delocalized among the neighboring V atoms and the electron-enrich carbon vacancy serves as an active center. Furthermore, highly active crystal face (110) exposed and confinement effect of double-deck carbon coating contributes to further enhance the electrocatalytic performance. Consequently, the single-crystal interweaved V_8C_7 nanosheets exhibits electrocatalytic performance comparable to those of Pt over wide pH range, with overpotential of η_{10} = 38 mV, η_{10} = 77 mV, and η_{10} = 47 mV and Tafel

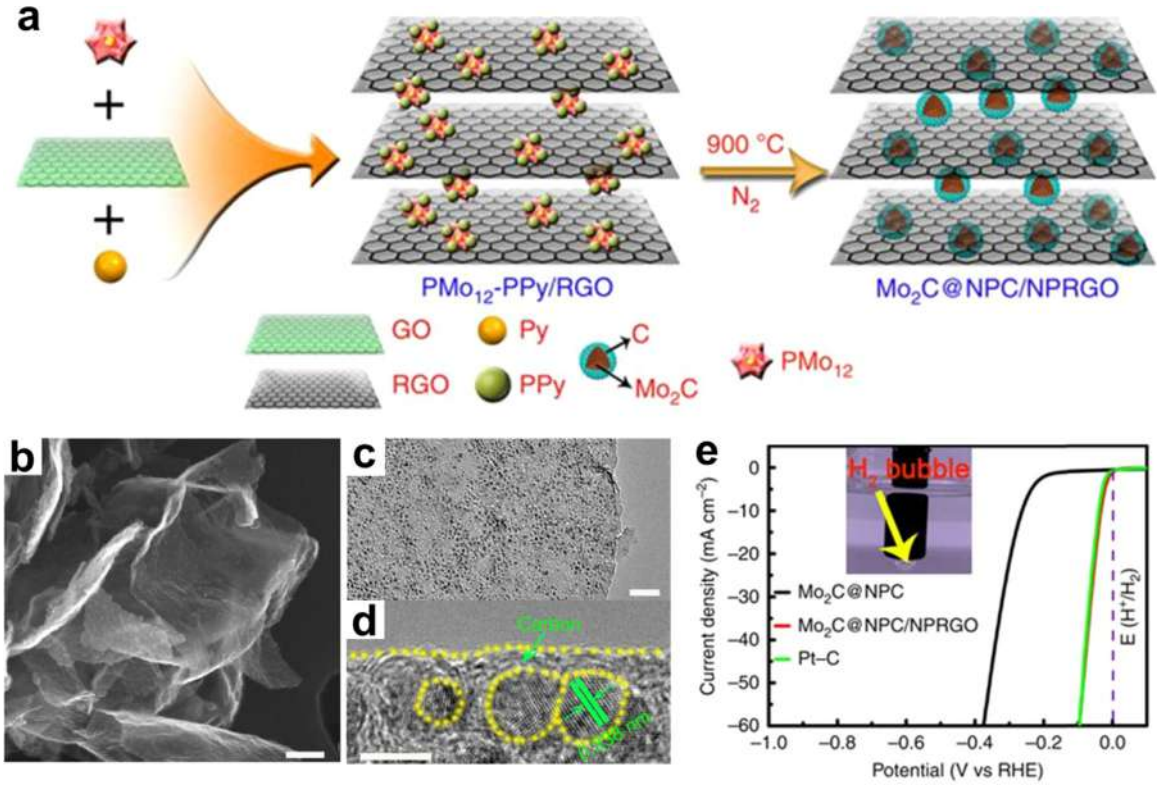

Fig. 18. (a) Schematic illustration of the synthetic process of Mo_2C@NPC/NPRGO. (b-d) SEM and TEM images of Mo_2C@NPC/NPRGO. Scale bar, (b) 200 nm; (c) 100 nm; (d) 5 nm. (e) HER activity of Mo_2C@NPC/NPRGO compared with Mo_2C@NPC and Pt-C catalyst in 0.5 M H_2SO_4. Inset: the production of H_2 bubbles on the surface of Mo_2C@NPC/NPRGO. (Reproduced from Ref. [62] with permission from Nature Publishing Group, Copyright 2016).

slope of 34.5, 64 and 44 mV dec^{-1} in 0.5 M H_2SO_4, 1.0 M PBS, and 1.0 M KOH, respectively [233].

As to the chromium based carbides, the work of B. Leonard et al. can be regarded as a very good example to demonstrate the HER activity trend across various ratios [234]. They reported a low temperature salt flux synthesis route for preparing pure phase chromium carbide with five different crystal structures as the HER electrocatalysts, including three common phases, Cr_3C_2, Cr_7C_3, and $Cr_{23}C_6$, and two rarely studied meta-stable phases, Cr_2C and CrC. All of the five phases of Cr-C were synthesized and isolated thoroughly via facilely tuning the chromium/carbon ratio, reaction temperature and annealing time. It was further observed that the electrocatalytic HER activity of Cr-C can be correlated

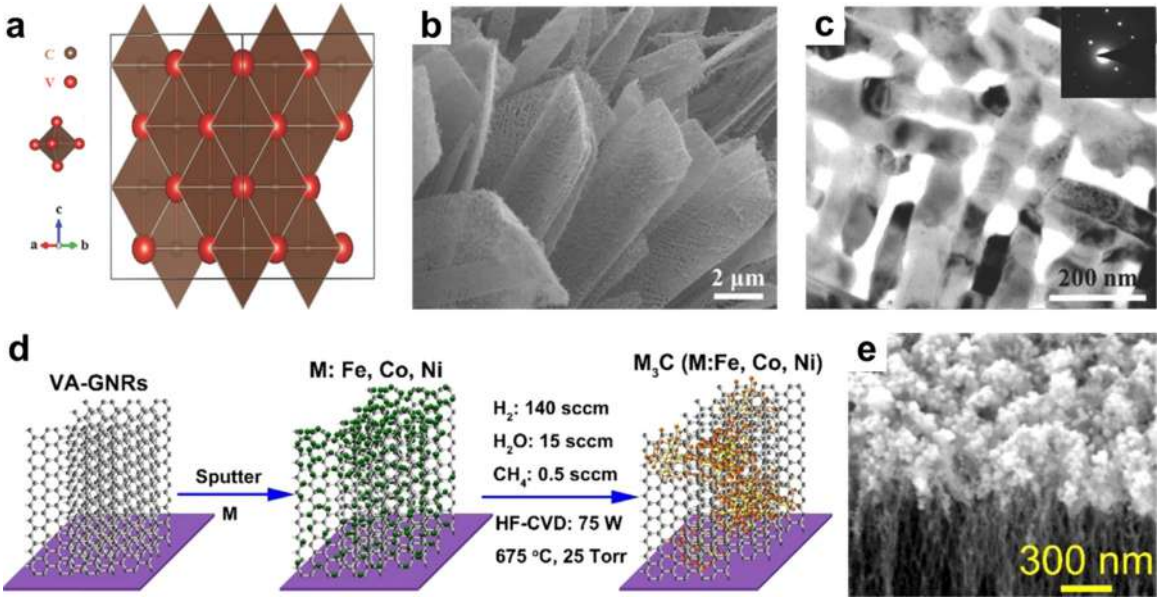

Fig. 19. (a) The structure of V_8C_7, brown and red spheres denote C and V atoms, respectively. (b-c) SEM and TEM images of V_8C_7@GC nanosheets. (Reproduced from Ref. [233] with permission from John Wiley & Sons, Inc., Copyright 2018). (d) Schematic illustration of the formation mechanism of nanocrystalline M_3C (M = Fe, Co, Ni) on VA-GNRs. (e) SEM image of M_3C nanocrystals grown on the tips of VA-GNRs. (Reproduced from Ref. [235] with permission from American Chemical Society, Copyright 2015).

well with differences in the density of states (DOS) at the Fermi level and types of bonding in each structure. With this premises, the most active phase is Cr_7C_3, which has the highest DOS at the Fermi level.

Promising results have also been found from Fe [235], Co [236], and Ni [237] based carbides in the last few years. To further enhance the electrochemical hydrogen evolution activity, Q. Yan et al. doped optimum amount of Fe into Ni_3C nanodots to optimize the electronic structure and surface composition of the electrocatalyst [237]. As a result, the Fe-Ni_3C exhibits better electrocatalytic activity (overpotential of η_{10} = 178 mV) than that of bare Ni_3C (overpotential of η_{10} = 235 mV). Notably, the work of X. Gou's group [235] provides a comprehensive analysis over M_3C (M = Fe, Co, Ni) grown on vertically aligned graphene nanoribbons via hot filament CVD method Fig. 19d-e. The graphene nanoribbon support plays a vital role in the design of these M_3C catalysts. It does not only provide high surface area for M_3C growth without aggregation, but also significantly enhance the conductivity of the obtained electrocatalyst to facilitate charge/proton transfer along the basal surfaces. As a result, the synergistic effect between 1D M_3C and 2D graphene nanoribbons gives the M_3C-GNRs superior HER performance as exemplified from the result of Fe_3C HER performance (overpotential of η_{10} = 49 mV and Tafel slope of 46 mV dec^{-1} in 0.5 M H_2SO_4).

3.3. Transition metal nitrides

Resembling TMCs, transition metal nitrides (TMNs) are also referred to as interstitial alloys. The nitrogen atoms, being small size, are inserted into the interstices of the metal lattice thereby resulting in the modification of the metal's *d*-band electronic structure [191,238]. To this end, the nitride surface usually displays an electron donating characteristics [239]. Further studies have found that the electronic structure of metal nitrides is remarkably different from those of the parent metal. The introduction of nitrogen will endow the electronic structure of TMNs with Pt-like behavior [193,194,240,241]. These promising features, coupled with their low electrical resistance and good corrosion resistance, give rise to the fact that TMNs have potential to replace Pt in the field of electrocatalysis [194]. For electrochemical hydrogen evolution reaction, metal nitrides exhibit outstanding activity that can be ascribed to the appropriate (neither to strong nor too weak) adsorption energy of H^+ on their active sites.

To date, the synthesis of metal nitrides are largely made through the high-temperature (500–800 °C) nitridation routes. The commonly involved reactions include gas-solid reactions (e.g., the reaction between metal precursor and ammonia gas [65,66,242,243]) or solid-solid reactions (e.g., the reaction between metal precursor and nitrogen-containing organic compounds [244,245]) to realize the controllable synthesis of metal nitrides. But, the contamination of carbon and oxygen will be introduced in this synthesis method and gave rise to the deteriorating the expected catalytic activity. For instance, some metal nitrides (Ni_3FeN and NiMoN) were obtained via nitridation of metal hydroxide with ammonia [246] or N_2 plasma treatment of the parent metal [247], both of which are known to be limited by weak controllability over shape and the preferred crystalline phase. And their HER catalytic activities recorded are not as such impressive. In the following subsections, the HER properties of frequently reported metal nitrides will be reviewed.

Up to now, different kinds of TMNs, like molybdenum nitride (MoN) [65,66], tungsten nitride (WN) [248,249], nickel nitride (Ni_3N) [242,250] and cobalt nitride (Co_4N) [251], have been discovered to be electrocatalysts for hydrogen production (Table 5). Among these metal nitrides, the Mo and W based nitrides are attracting considerable attention owing to their tendency to mimic catalytic behavior to precious metals. Yet, there is still a concern of susceptibility to poisoning and deactivation [193,252]. The mechanism of HER electrocatalysis relied on these nitrides has remained debatable till the work of Xie et al., who prepared MoN nanosheets with atomic thickness (1.3 nm) via liquid exfoliation of MoN bulk (Fig. 20a-b) for theoretical and experimental elucidation of the active sites [253]. The calculated DOS of the single layer MoN slab demonstrated that the metallic MoN (Fig. 20c) nanosheets possess higher charge density than that of bulk material (Fig. 20d), which means that MoN nanosheets can effectively facilitate electron transfer during the electrocatalytic HER process. The exposed apical Mo atoms on the surface of MoN nanosheets can serve as active site in HER. With such a unique atom alignment and improved conductivity, excellent catalytic activity has been realized from MoN.

In order to improve the HER catalytic activity of metal nitrides, various approaches have been suggested to tune the electronic and hence ultimately optimizing the H ion adsorption and H_2 molecule desorption [53,254–256]. In one hand, bimetallic nitrides (e.g., NiMoN [53,247], CoMoN [257] and NiFeN [246]) have been widely studied owing to their tendency to introduce such electronic perturbations following the interaction between the two dissimilar transition metals. For example, R. Adzic et al. have successfully realized the optimum Mo-H binding energy after introducing Ni atom into MoN to form $NiMoN_x$ nanosheet with the thickness of 4–15 nm [243]. They confirmed the strong interaction between Mo and Ni atoms through EXAFS analysis, revealing an increment in Ni-Ni distance and a decrement in Ni-Mo distance with the nitridation process. As a result, the HER activity of the obtained $NiMoN_x$ (onset overpotential of 78 mV and Tafel slope of 35.9 mV dec^{-1}) is much higher than that of MoN (onset overpotential of 157 mV and Tafel slope of 54.5 mV dec^{-1}). In another study, T. Zhang et al. prepared Ni_3FeN nanoparticles (NPs) with a particle size of 100 nm as an efficient and durable HER electrocatalyst [246]. Its electrocatalytic activity outperformed the bulk Ni_3FeN, the monometallic nitride (Ni_3N) and mixed metal oxide (NiFe-MMO) in alkaline media (1.0 M KOH). In the other hand, constructing heterostructure of metal nitrides with nanocarbon or/and other transition metal-based compounds is considered as an effective way to improve the electrocatalytic hydrogen production activity [52,54,64,242,244,258]. S. Qiao's group synthesized a nanohybrid catalyst of 2D molybdenum nitride and 2D carbon nitride (MoN@C_3N_4) through an interface engineering strategy [66]. The SEM and TEM images (Fig. 21a) of MoN@C_3N_4 demonstrate the 2D morphology with the g-C_3N_4 growing on the surface of MoN nanosheets. From the DFT calculations and the corresponding projected density of states (PDOS) spectra (Fig. 21b), a charge redistribution occurs at the interlayer between MoN and C_3N_4 with the accumulation of electrons. Meanwhile, the electrons are transferred from the inner MoN layer to the outer g-C_3N_4 layer (Fig. 21c). As a result, the well-designed MoN@C_3N_4 nanosheets exhibits excellent electrochemical activity for HER with an overpotential η_{10} = 110 mV in 1.0 M KOH, which is remarkably lower than that of the single component counterpart and the physical mixture MoN@C_3N_4 (Fig. 21d). The work of Fu et al. was another exemplary report to elucidate the benefit of heterostructures based on metal nitrides for enhancing the catalytic activity [54]. They fabricated a heterostructure of holey reduced graphene (HGr) oxide coupled with small-sized Mo_2N-Mo_2C (Mo_2N-Mo_2C/HGr) (Fig. 21e-f). Benefiting from the excellent charge/mass transfer ability of HGr, the high dispersion of small-sized nanoparticles and the intimate contact between Mo_2C and Mo_2N, the resulting Mo_2N-Mo_2C/HGr heterojunction exhibited enhanced electrocatalytic hydrogen generation performance over a series of control samples in both acidic and alkaline electrolytes. The DFT calculations showed that the ΔG_H^* appeared to have its smallest value on the N site of the N-Mo-C interface (Fig. 21g-h), indicating that the N site should be the main active center in the Mo_2N-Mo_2C/HGr heterostructure. It can be seen that transition metal nitrides are promising electrocatalysts for HER, though so far hampered by the inefficient exposure of active sites. Thus, the development of novel synthetic methods (or improvement of the existing ones) is considered as the prerequisite for further insight into the designing advanced HER electrocatalysts.

Table 5
Compilation of HER performance based on various transition metal nitride electrocatalysts under different conditions.

Materials	Substrate	Electrolyte	Overpotential (mV)		Tafel slope (mV dec^{-1})	Loading density (mg cm^{-2})	Year	Ref.
			η_{10}	η_{100}				
WN NA	Carbon cloth	0.5 M H_2SO_4	198	~ 340	92	2.5	2015	[248]
WN NW	Carbon cloth	1 M KOH	130	~ 245	57.1	–	2017	[362]
MoN nanosheet	GCE	0.5 M H_2SO_4	~ 220	–	90	0.285	2014	[253]
γ-Mo_2N	GCE	0.5 M H_2SO_4	381	–	108	0.102	2015	[64]
Ni_3N NSs	GCE	0.5 M H_2SO_4	59	~ 100	59.8	0.32	2016	[342]
MoN-NC	GCE	0.5 M H_2SO_4	62	–	54	0.154	2017	[65]
Ni_3N@CQDs	GCE	1 M KOH	69	–	108	~ 0.18	2018	[242]
CoN_x/C	GCE	0.5 M H_2SO_4	133		57	2.0	2015	[52]
WN_x-NRPGC	GCE	0.5 M H_2SO_4	132	–	86	0.362	2018	[363]
δ-WN/Co	GCE	1 M KOH	76	~ 285	98	1.12	2018	[249]
Co-Ni_3N	Carbon cloth	1 M KOH	194	~ 280	156	2.91	2018	[364]
Mo_2N@NC	GCE	1 M KOH	85	–	54	–	2017	[245]
MoN@C_3N_4	GCE	1 M KOH	110	–	57.8	0.41	2018	[66]
Fe-WCN	GCE	0.1 M H_2SO_4	220	–	47	0.4	2013	[365]
P-WN/rGO	GCE	0.5 M H_2SO_4	85	~ 260	54	0.337	2015	[366]
V-Co_4N NS	Ni foam	1 M KOH	37	–	44	–	2018	[251]
NiMoN	Carbon cloth	1 M KOH	109	~ 165	95	~ 2.5	2016	[247]
$Co_{0.6}Mo_{1.4}N_2$	GCE	0.1 M $HClO_4$	~ 290	–	–	0.342	2013	[257]
Ni-C-N NSs	GCE	1 M KOH	~ 31	–	40	0.2	2016	[367]
$Cu_xNi_{4-x}N$	Ni foam	1 M KOH	12	111	86	0.815	2017	[368]
Ni-Mo-N	GCE	0.5 M H_2SO_4	~ 40	–	39	1.0	2016	[53]
Ni_3FeN-NPs	GCE	1 M KOH	158	~ 300	42	~ 0.35	2016	[246]
$NiMoN_x$/C	GCE	0.1 M $HClO_4$	–	–	35.9	0.25	2012	[243]
Mo_2N-Mo_2C/HGr	GCE	0.5 M H_2SO_4	157	320	55	0.337	2018	[54]

Note: GCE, glassy carbon electrode.

3.4. Transition metal oxides

Transition metal oxides (TMOs) have been widely used in fields of oxygen evolution reaction (OER) [259–261], oxygen reduction reaction (ORR) [262–264], and photochemical reduction reaction [265–267] owing to their environmentally benignity, stability and cost-effective characteristics. Unfortunately, most metal oxides fail to electrocatalyze hydrogen evolution reaction due to their low intrinsic electrical conductivity and inappropriate free energy of hydrogen adsorption [268–273]. Considering their considerable OER performance, it is of immense importance to develop TMO-based HER catalyst to form a bifunctional catalyst for overall water splitting. To date, substantial efforts, e.g., nanostructuring [274], creating oxygen vacancies [35], constructing heterostructure of TMO with carbon materials [67] or metal [68,275] and doping the heteroatom into TMO crystal [276], have been made to improve the hydrogen production activity of TMO-based electrocatalysts. As collected in Table 6, various metal oxide electrocatalysts are designed and used as electrocatalysts for HER under different conditions.

Usually, TMO materials acted as HER electrocatalysts in alkaline electrolytes because they are unstable in acidic solution, especially iron group metal oxides [277–280]. Very recently, S. Qiao's group reported

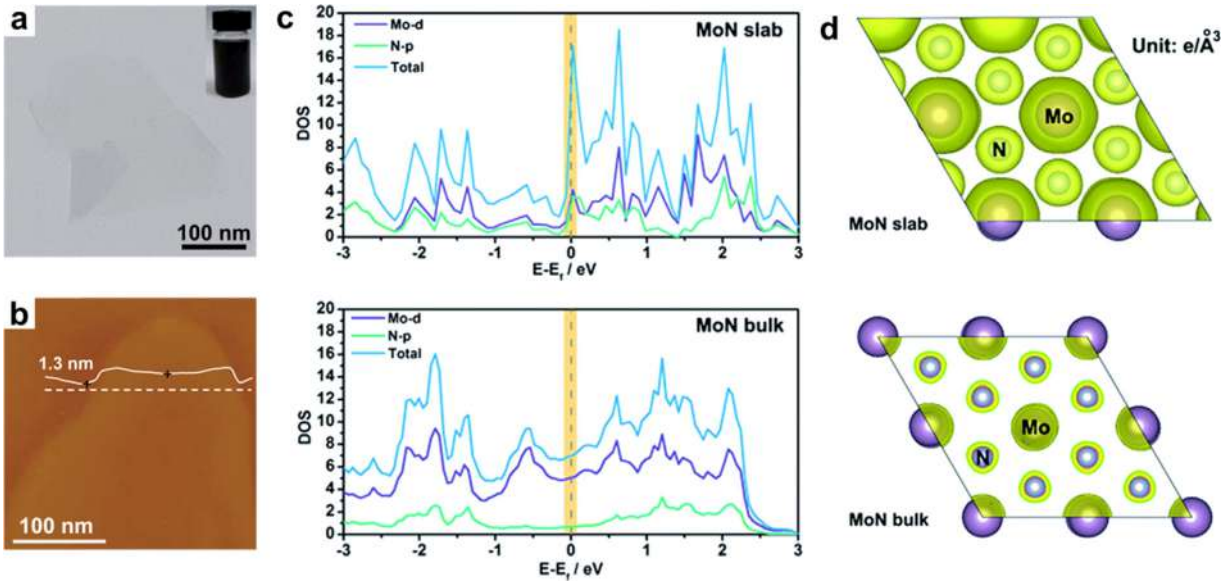

Fig. 20. (a-b) TEM and AFM images of MoN nanosheet. Inset of (a): homogeneous colloidal dispersion of the atomically-thin MoN nanosheets. (c) Calculated density of states (DOS) of the single-layered MoN slab (top) and the bulk MoN (bottom). The orange shaded areas highlight the DOS contribution near the Fermi level. (d) Charge density distributions of the single-layered MoN slab (top) and the bulk MoN (bottom) near the Fermi level based on a specific equal value, respectively. (Reproduced from Ref. [253] with permission from The Royal Society of Chemistry, Copyright 2014).

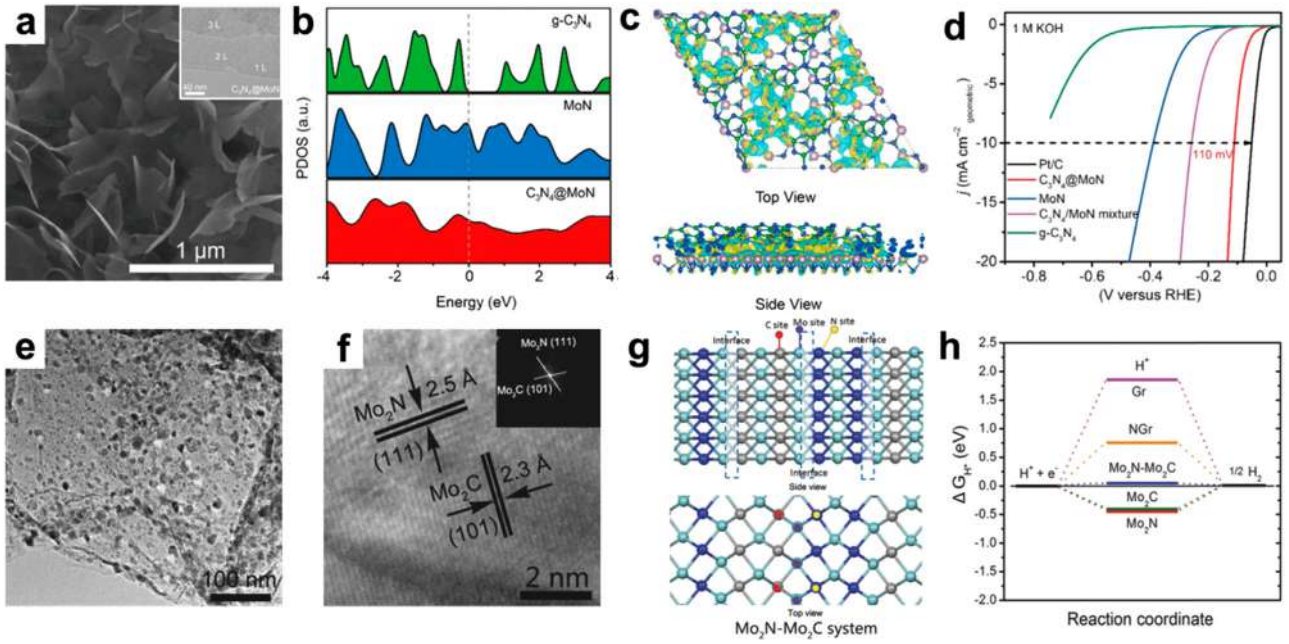

Fig. 21. (a) SEM and TEM images of C_3N_4@MoN nanosheets. (b) The density of state (DOS) spectra of g-C_3N_4, MoN, and C_3N_4@MoN. (c) Interfacial electron transfer in C_3N_4@MoN. Yellow and cyan iso-surface represents electron accumulation and electron depletion. Pink, blue, and green spheres represent Mo, N, and C atoms, respectively. (d)Linear sweep voltammetry curves of the different catalysts measured in 1.0 M KOH. (Reproduced from Ref. [66] with permission from Elsevier, Copyright 2018). (e-f) STEM and HRTEM images of the Mo_2N-Mo_2C/HGr hybrid. (g) Possible adsorption sites of H* on the Mo_2N-Mo_2C system. (h) Calculated free-energy diagram for HER based on the various studied systems. (Reproduced from Ref. [54] with permission from John Wiley & Sons, Inc., Copyright 2018).

Table 6
Compilation of HER performance based on various transition metal oxide electrocatalysts under different conditions.

Materials	Substrate	Electrolyte	Overpotential (mV)		Tafel slope (mV dec^{-1})	Loading density (mg cm^{-2})	Year	Ref.
			η_{10}	η_{100}				
WO_{3-x}	Carbon nanofiber	0.5 M H_2SO_4	185	–	89	0.21	2016	[282]
WO_3	GCE	0.5 M H_2SO_4	38	–	38	0.285	2017	[284]
$WO_3 \cdot H_2O$	GCE	0.5 M H_2SO_4	66	–	34.8	–	2017	[283]
NiO NRs	Carbon fiber	1.0 M KOH	110	~ 280	100	~ 0.2	2018	[281]
$WO_{2.9}$	GCE	0.5 M H_2SO_4	70	–	50	0.285	2015	[35]
δ-MnO_2 NSs	Ni foam	1.0 M KOH	197	~ 350	66	~ 1.59	2017	[369]
$NiFeO_x$	Carbon fiber	1.0 M KOH	88	~ 220	150	3.0	2015	[274]
Ni/NiO	Ni foam	1.0 M KOH	145	–	43	~ 0.3	2015	[370]
Co/Co_3O_4	Ni foam	1.0 M KOH	~ 90	~ 240	44	0.85	2015	[275]
Mo-$W_{18}O_{49}$	GCE	0.5 M H_2SO_4	45	–	54	~ 0.16	2016	[276]
N-MoO_3	GCE	0.5 M H_2SO_4	–	~ 540	101	0.694	2016	[371]
WO_2-carbon NWs	GCE	0.5 M H_2SO_4	56	–	44	0.35	2015	[86]
CoO_x@CN	GCE	1.0 M KOH	232	–	–	~ 0.12	2015	[279]
WO_x@C/C	GCE	0.5 M H_2SO_4	15	–	19.2	~ 0.375	2018	[67]
NiO/Ni-CNT	GCE	1.0 M KOH	80	–	82	0.40	2014	[68]
Fe_2O_3/Fe@CN	GCE	1.0 M KOH	330	–	114	0.28	2015	[278]
MoO_2@PC-RGO	GCE	0.5 M H_2SO_4	64	–	41	0.14	2015	[70]

Note: GCE, glassy carbon electrode.

the synthesis of NiO nanorods (NRs) (Fig. 22a) with ample oxygen vacancies [281]. And then, they explored the relationship between oxygen vacancy concentration and the corresponding electrocatalytic activity. As seen in Fig. 22b, the introduction of oxygen-vacancy in NiO NRs lead to the emergence of some new electronic states close to the Fermi level, which directly result in higher electron transfer rate of oxygen vacancy-enriched NiO nanorods and enhancement of HER performance. The largest carrier concentration, obtained from their Mott-Schottky plots in Fig. 22c, was achieved when the appropriate oxygen vacancies were introduced. Likewise, tungsten oxide (WO_x) has attracted extensive research interests in electrocatalysis because it is much more thermodynamically stable in acidic solution than most metal oxides [35,276,282–284]. In this regard, H. Yang et al. prepared oxygen-defect tungsten oxide ($WO_{2.9}$), as the HER electrocatalyst in acidic media, through a facile thermal treatment of commercial WO_3 nanoparticles [35]. From Fig. 22d-e, $WO_{2.9}$ exhibits ordered defect structure with regularly stair-step shape, whereas the WO_3 exhibits continuous regular lattice fringes. Subsequent DFT calculations confirmed that the (010) and (001) were the most stable crystal faces for $WO_{2.9}$ and WO_3, respectively. And the new characteristic configuration was observed on the $WO_{2.9}$(010). Furthermore, the hydrogen adsorption energy on $WO_{2.9}$(010) is close to thermodynamic neutral ($\Delta G_H \approx 0$ eV), suggesting the improvement of HER activity relative to that of WO_3(001). As expected, the oxygen-defect $WO_{2.9}$ (overpotential of $\eta_{10} = 70$ mV and Tafel slope of 50 mV dec^{-1}) displays better electrochemical hydrogen generation activity compared to pristine WO_3 in acidic solution (overpotential of $\eta_{10} = 637$ mV and Tafel slope of 120 mV dec^{-1}) (Fig. 22f). On this basis, Zeng and co-workers

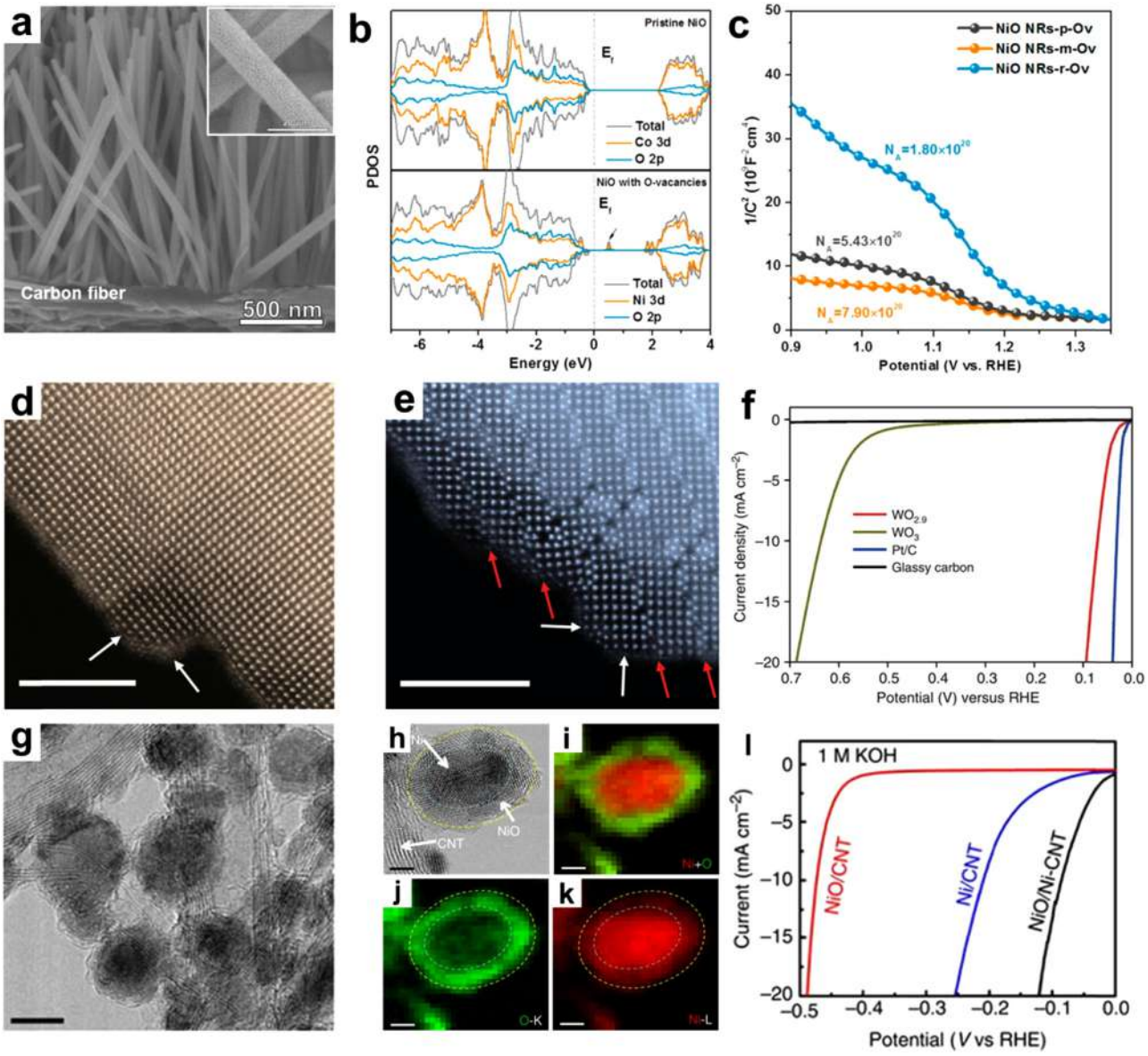

Fig. 22. (a) SEM images of NiO nanorod arrays on carbon fibers. (b) The projected density of states on pristine NiO and NiO with oxygen-vacancies. (c) Mott-Schottky plots of NiO NRs with varied amounts of oxygen-vacancies. (Reproduced from Ref. [281] with permission from Elsevier, Copyright 2018). (d-e) HAADF-STEM images of WO_3 and $WO_{2.9}$. Scale bar, 5 nm, (f) HER activity of various catalysts in 0.5 M H_2SO_4. (Reproduced from Ref. [35] with permission from Nature Publishing Group, Copyright 2015). (g-h) STEM bright-field images of the NiO/Ni-CNT. Scale bar, 2 nm. (i-k) Chemical maps for the spatial distribution of Ni and O and their overlay, from the whole area shown in (h). (l) Linear sweep voltametry curves of the three hybrid materials in 1.0 M KOH. (Reproduced from Ref. [68] with permission from Nature Publishing Group, Copyright 2014).

introduced ample oxygen vacancies into WO_3 nanosheets and realized superior electrocatalytic activity for hydrogen evolution in acidic media (overpotential of η_{10} = 38 mV and Tafel slope of 38 mV dec^{-1}) [284]. In addition, heterogeneous atom doping can also remarkably improved electrocatalytic performance of tungsten oxide via manipulating the electronic and geometric structure to increase the number of active sites [276]. And constructing heterostructure is also an effective way to enhance the HER performance of TMO-based catalysts. For a instance, a novel NiO-Ni/carbon nanotube nanohybrid (NiO-Ni/CNT) was designed by Dai's group [68]. Fig. 22g-k shows the presence of approximately 10 nm NiO/Ni nanoparticles with a core shell-like structure anchored to multi-walled carbon nanotube network. The as-obtained NiO-Ni/CNT electrocatalyst exhibits hydrogen evolution activity close to that of Pt (Fig. 22i) in alkaline media as a result of the synergetic effect of the metal, metal oxide, and nanocarbon.

3.5. Transition metal borides

Transition metal borides (TMBs) are exceptionally stable over a wide pH range, revealing their potential ability to serve as alternative HER electrocatalysts [285]. As early as decades ago, L. Kuznetsova et al. studied the HER kinetics on some metal borides in acidic media (1.0 M H_2SO_4) and found that their hydrogen generation activity increases in the order of $ZrB_2 < NbB_2 < TaB_2 < W_2B_5$ [286]. In 2012, Hu et al. reported that the commercially available molybdenum boride (α-MoB) is a highly active HER electrocatalyst both in acidic and alkaline media [224]. But, it is a challenge to synthesize the pure metal borides [10,69,287–293]. And the search for appropriate and reliable synthetic methods is of great significance in promoting the development of TMBs in electrochemical hydrogen evolution.

Recently, some TMB materials have been explored to be HER electrocatalysts (Table 7). A multi-step arc-melting approach was adopted

Table 7
Compilation of HER performance based on various transition metal boride electrocatalysts under different conditions.

Materials	Substrate	Electrolyte	Overpotential (mV)		Tafel slope (mV dec^{-1})	Loading density (mg cm^{-2})	Year	Ref.
			η_{10}	η_{100}				
MoB	CPE	1.0 M KOH	~ 210	–	59	2.3	2012	[224]
MoB_2	Carbon sheet	0.5 M H_2SO_4	–	–	100	~ 0.25	2017	[71]
Mo_2B_4	Carbon sheet	0.5 M H_2SO_4	310	–	80	~ 0.65	2017	[294]
Mo_3B film	Mo foil	0.5 M H_2SO_4	~ 230	–	52	–	2017	[372]
FeB_2	GCE	1.0 M KOH	61	~ 170	87.5	0.2	2017	[296]
Co-B	Ni foil	1.0 M KOH	70	270	68	–	2018	[69]
Co-B NPs	–	0.5 M PBS	251	–	75	–	2015	[373]
Ni-B	GCE	1.0 M $HClO_4$	~ 90	–	53/112	–	2016	[288]
Ni-B_x	Cu plate	0.5 M H_2SO_4	45	~ 125	43	–	2016	[10]
MoAlB	–	0.5 M H_2SO_4	301	–	68	–	2017	[374]
CoNiB	Ni foam	1.0 M KOH	205	–	–	–	2017	[375]
CoNiB	GCE	0.5 M PBS	170	–	51	~ 2.1	2016	[376]
Co_2B/NG	GCE	1.0 M KOH	127	–	92.4	0.21	2016	[377]

Note: GCE, glassy carbon electrode; CPE, carbon paste electrode.

by P T Fokwa's group to prepare Mo_2B, α-MoB, β-MoB, and MoB_2 [71]. Fig. 23a shows the crystal structures of tetragonal Mo_2B and α-MoB, orthorhombic β-MoB, and hexagonal MoB_2. Their electrocatalytic activity in acidic electrolyte (0.5 M H_2SO_4) are demonstrated in Fig. 23b, revealing that the hydrogen evolution activity increases with increasing boron content and the boron-rich MoB_2 possesses the highest activity for hydrogen generation. This result is similar to the recently reported nickel phosphides [100]. The introduction of non-metal elements could facilitate the trapping of the positively charged protons and enhance the hydrogen adsorption on TMBs for subsequent reaction steps [25,100]. Therefore, inspired by the original aforementioned work, the focus of future electrochemical hydrogen production research should be on boron-rich TMBs. In connection to this, Fokwa's group [294] also successfully prepared single-phase bulk of Mo_2B_4 for hydrogen generation by tin flux synthesis [295]. Fig. 23c shows the crystal structure of Mo_2B_4 with two types of boron layers alternating along [001], a flat layer (graphene-like) and a puckered layer (phosphorene-like). Significantly, the ΔG_H^* values (Fig. 23d) on two different boron layers are not the same, indicating their different HER activities. The ΔG_H^* on flat boron layer (flat B-T) reaches zero at around 50% H coverage, whereas that value on the puckered boron layer is far away zero at all H coverage. Additionally, Geyer et al. prepared the boron-rich iron diboride nanoparticles (FeB_2 NPs) through a facile chemical reduction of Fe^{2+} using $LiBH_4$ in an organic solvent [296]. The TEM image of FeB_2 NPs in Fig. 23e displays their size in the range of 20–50 nm. Surprisingly, the as-synthesized FeB_2 NP catalyst exhibited remarkable electrocatalytic performance for HER (Fig. 23f), requiring the overpotential of only η_{10} = 61 mV and maintaining stability over long-term electrolysis tests in alkaline solution (1.0 M KOH). Fig. 23g shows four typical hydrogen adsorption sites with relatively low ΔG_H^* on the (001) and (110) surfaces of FeB_2. The B sites act as the active sites for HER and the low-index (001) is largely responsible for hydrogen generation on FeB_2

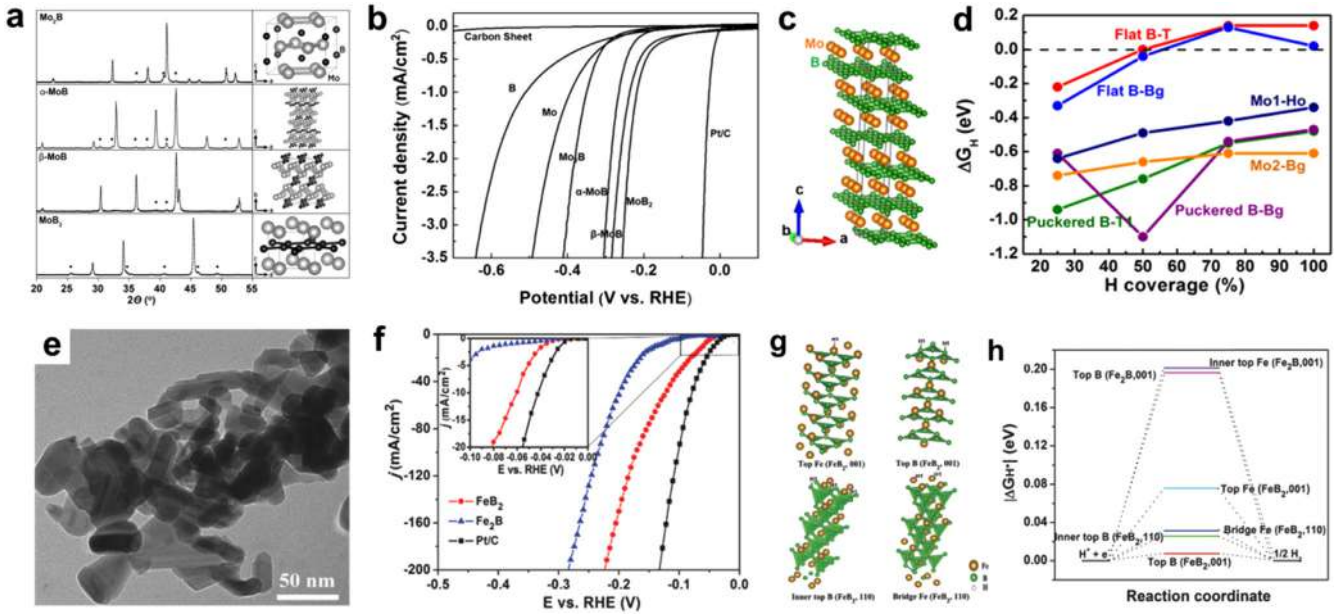

Fig. 23. (a) Left: X-ray powder diffraction patterns, Right: crystal structures of Mo_2B, α-MoB, β-MoB, and MoB_2. (b) Polarization curves of the different catalysts measured in 0.5 M H_2SO_4. (Reproduced from Ref. [71] with permission from John Wiley & Sons, Inc., Copyright 2017). (c) Crystal structure of Mo_2B_4 showing two types of boron layers alternating along [001]. (d) Gibbs free energy (ΔG_H) for H adsorption on different surfaces plotted as a function of hydrogen coverage. (Reproduced from Ref. [294] with permission from American Chemical Society, Copyright 2017). (e) TEM image of FeB_2 nanoparticles. (f) Electrochemical performance of FeB_2 and Fe_2B electrodes for HER in 1.0 M KOH. (g) Four typical H* adsorption sites with relatively low ΔG_H^* on the (001) and (110) surfaces of FeB_2. (h) Calculated free-energy diagram of HER over low-index (001) and high-index (110) surfaces of FeB_2 and Fe_2B at equilibrium potential. (Reproduced from Ref. [296] with permission from John Wiley & Sons, Inc., Copyright 2017).

(Fig. 23h). As comparison, FeB_2 possesses higher hydrogen evolution ability than Fe_2B under the same conditions.

4. Other non-noble metal electrocatalysts

In addition to earth-abundant transition metal based compounds as potential replacements of precious metal for HER electrocatalysis, non-noble transition metals (TMs, i.e., Ni, Co, Fe, Cu etc.) and their alloys are also the focus of recent research. Generally, the research conducted based on TMs is, therefore, limited to only alkaline electrolytes due to their instability in acidic electrolytes [297–300]. Very recently, a variety of TMs nanoparticles encapsulated in carbon nanomaterials (TM@C) including nitrogen-doped graphene [76,301–303] and nitrogen-doped carbon nanotubes [75,304–306] are of particular interest. The synergistic effect [75,76,305,307,308] between TMs cores and N-doped carbon shell contributes to the enhancement of HER electrocatalytic performance. In this section, we focus on the non-precious transition metal catalysts for electrochemical HER.

Generally, various synthetic methods were utilized to prepare TM electrocatalyst. For pure TMs without the support of carbon nanomaterials, wet-chemical reaction route is usually employed to grow self-supporting metal precursors, followed by reduction process through electrochemical reduction [298], solvothermal reduction [299,309], and gas-phase reduction [18]. For instance, Sun's group reported the synthesis of ultrathin nickel nanosheet array (Ni-NSA) via mildly reducing $Ni(OH)_2$ nanosheet arrays in ethylene glycol solution assisted by NaOH [299]. The resulting Ni nanosheets possessed ten atomic layers in thickness owing to the slow reaction kinetics. While, when preparing carbon nanomaterials supported TM electracatalysts, the simultaneous pyrolysis of nanostructured transition-metal precursors and carbon source [72,75,304,306,310] or pre-prepared MOFs precursors [76,305,311] were used. For example, Hu et al. synthesized a 3D copper-encased N-doped carbon nanotube arrays grown on copper foam (Cu@N-CNT) via the pyrolysis of polydopamine (PDA)-coated Cu_2O nanowire arrays [304]. The carbonization of PDA shell and the reduction of Cu_2O core are occurred simultaneously. Moreover, the morphology and thickness of N-doped carbon nanotubes can be controlled by the thickness of PDA shells. To date, kinds of non-noble transition metals have been reported in this field (Table 8).

4.1. Single metal electrocatalysts

Researches on non-precious single metal catalysts for HER have focused exclusively on 3*d* transition metals, such as Fe [312], Co [301,305,306,313] and Ni [298,299,314] owing to their earth abundance, high electrical conductivity and electrochemical activity. They are usually used to catalyze electrochemical hydrogen evolution in neutral or alkaline media [298,299,313,314]. M. Ma et al. designed Co nanocrystal assembled hollow nanoparticles (Co-HNP) as an electrocatalyst for hydrogen production from neutral-pH water [313]. The results indicated that the catalyst exhibited remarkable HER activity with overpotential of η_{10} = 85 mV and Tafel slope of 38 mV dec^{-1}. Sun's group reported an ultrathin Ni nanosheet arrays (Ni-NSAs) grown on nickel foam [299]. They found that the partial oxidized Ni-NSAs could significantly improve the HER activity in alkaline media. Such superior HER activity was ascribed to the synergistic effect of the Ni/Ni^{2+} interface [68]. The strong electrostatic affinity of Ni^{2+} site for OH^- generated via water dissociation is beneficial to the adsorption of protons by nearby Ni site for successive H_2 generation. Inspired by these pioneering studies, Zheng's group also successfully synthesized ultrathin Ni nanosheets (ca. 1.6 nm thickness) with trace sulfur adsorbed on their surface by electrochemically activating 2D nanosheets of Ni-S coordination polymer (ca. 16 nm thickness) [298]. Fig. 24a-b shows the SEM images of 1, 4-benzenedithiol (BDT) coordinated Ni nanosheets (Ni-BDT) and the Ni-BDT nanosheets after electrochemical activation (Ni-BDT-A). From the EXAFS spectra in Fig. 24c, the relatively low coordination number of Ni-Ni and similar Ni-Ni bond length with Ni foil verified the formation of ultrathin Ni nanosheets (Ni NSs). Meanwhile, the XPS analysis also revealed that the content of S in the electrocatalyst surface was greatly decreased after electrochemical activation and the Ni species detected were predominately Ni^0 with only trace amount of Ni^{2+} coordinated by S [298]. Theoretical results

Table 8
Compilation of HER Performance based on various non-noble metal electrocatalysts under different conditions.

Materials	Substrate	Electrolyte	Overpotential (mV)		Tafel slope (mV dec^{-1})	Loading density (mg cm^{-2})	Year	Ref
			η_{10}	η_{100}				
Co-HNP	Carbon cloth	1.0 M PBS	85	237	38	1.0	2016	[313]
Ni-NSA	Ni foam	0.1 M KOH	~ 120	~ 260	114	–	2015	[299]
Ni NSs	Carbon cloth	1.0 M KOH	80	150	70	0.3	2017	[298]
Fe/SWCNTs	GCE	0.5 M H_2SO_4	77	–	40	0.18	2015	[312]
Co-NRCNTs	GCE	0.5 M H_2SO_4	260	–	80	~ 0.28	2015	[306]
Co@NG	GCE	0.5 M H_2SO_4	265	–	98	0.285	2015	[301]
Co@BCN	GCE	0.5 M H_2SO_4	96	–	63.7	–	2016	[311]
Co@N-CNTs@rGO	GCE	0.5 M H_2SO_4	87	~ 170	52	~ 0.5	2018	[305]
Co@N-C	GCE	1.0 M $HClO_4$	200	–	100	~ 4.5	2014	[310]
Co@NGF	–	0.5 M H_2SO_4	125	–	93.9	0.28	2015	[302]
Cu@NC NT	Cu foam	1.0 M KOH	123	–	61	–	2017	[304]
SA-Ni-G	GCE	0.5 M H_2SO_4	~ 180		45	–	2015	[327]
SA-Mo-NC	GCE	0.1 M KOH	132	–	90	0.408	2017	[378]
SA-Ni-C	GCE	0.5 M H_2SO_4	34	112	41	0.283	2016	[325]
SA-Co-NG	GCE	0.5 M H_2SO_4	147	–	82	0.285	2015	[326]
NiW	Ni foam	1.0 M KOH	36	–	43	~ 2.8	2018	[335]
NiMo NWs	Ni foam	1.0 M KOH	~ 30	–	86	0.41	2016	[18]
NiCo NWs	–	1.0 M KOH	36	143	34.1	~ 7.5	2018	[297]
$MoNi_4$	Ni foam	1.0 M KOH	15	–	30	–	2017	[73]
NiMo NSs	Ni foam	1.0 M KOH	35	136	45	–	2017	[309]
NiMo-NHG	GCE	0.5 M H_2SO_4	30	~ 125	41	–	2018	[307]
NiMo-NGTs	GCE	0.5 M H_2SO_4	65	~ 225	67	2.0	2016	[72]
NiCu@C	Graphite plate	0.5 M H_2SO_4	48	~ 160	63.2	~ 0.385	2017	[334]
NiCo@NC	GCE	0.1 M H_2SO_4	142	–	105	1.6	2015	[303]
FeCo@NCNTs	GCE	0.1 M H_2SO_4	~ 280	–	74	0.32	2014	[75]
FeCo@NG	GCE	0.5 M H_2SO_4	262	–	74	0.285	2015	[76]

Note: GCE, glassy carbon electrode.

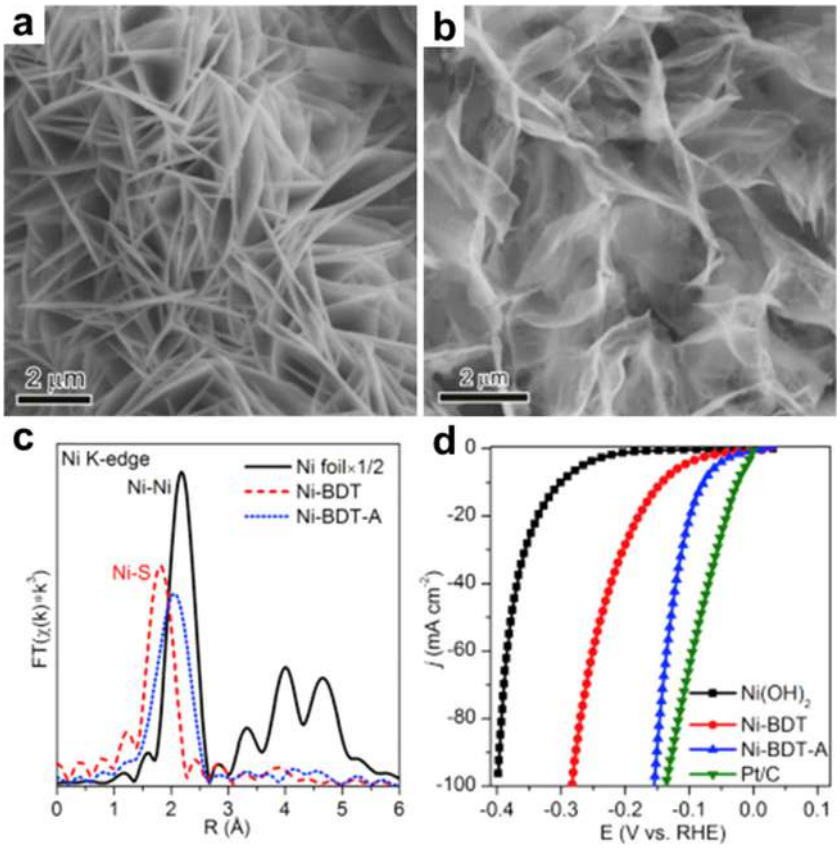

Fig. 24. (a-b) SEM images of Ni-BDT NSs and ultrathin Ni NSs, respectively. (c) EXAFS spectra of Ni foil and Ni-BDT before and after electrochemical activation. (d) Polarization curves for various catalysts in 1 M KOH. (Reproduced from Ref. [298] with permission from Elsevier, Copyright 2017).

demonstrated that Ni^0 served as the actual catalytically active sites for hydrogen production, and very small amount of $S_{ad}^{\delta-}$ remaining on the Ni nanosheets surface promoted the formation of the H_{ads} at the Ni^0 sites via forming $S_{ad}^{\delta-}$-hydrated cation networks. The promotion effect imparts in-situ-generated ultrathin Ni NSs superior electrochemical performance toward the HER with a low overpotential of η_{10} = 80 mV in 1.0 M KOH (Fig. 24d).

To realize the stable HER electrocatalysis in all-pH range, carbon nanomaterials have been extensively used. In this respect, Co encapsulated nitrogen-rich carbon nanotubes (Co-NRCNTs) [306] and Co nanoparticles embedded into the interlamination of N-doped graphene (Co@NGF) [302] were successfully constructed to electrolyze water in acidic, neutral and basic media. Recently, a novel strategy was reported by F. Fang et al. to prepare ultrafine Co nanoparticles (NPs) encapsulated in N-doped carbon nanotubes (N-CNTs) grafted on reduced graphene oxide (rGO) surface (Co@N-CNTs@rGO) (Fig. 25) [305]. The unique 3D hierarchical architecture composed of 0D Co NPs, 1D N-CNTs and 2D rGO, which endowed the Co@N-CNTs@rGO with more exposed active sites and enhanced mass transfer diffusion kinetics. The as-obtained hybrid electrocatalysts exhibited outstanding electrochemical activity toward HER with a low overpotential of η_{10} = 87 mV in 0.5 M H_2SO_4 and η_{10} = 108 mV in 1.0 M KOH.

To enhance the electrocatalytic activity and atomic utility, successful strategies, downsizing the metal nanoparticles into isolated single atoms for more exposed active sites, are usually employed [315–317]. Isolated metal atoms demonstrate more electrocatalytically

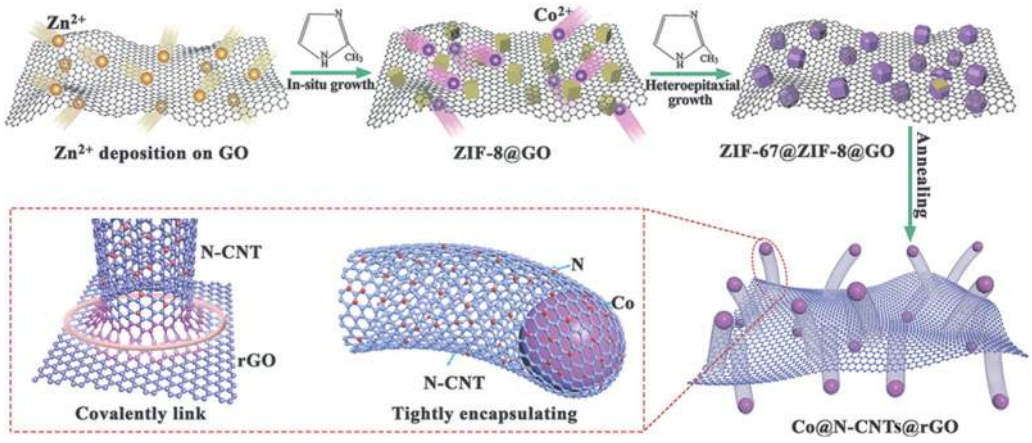

Fig. 25. Synthetic process of Co@N-CNTs@rGO nanohybrid. (Reproduced from Ref. [305] with permission from John Wiley & Sons, Inc., Copyright 2018).

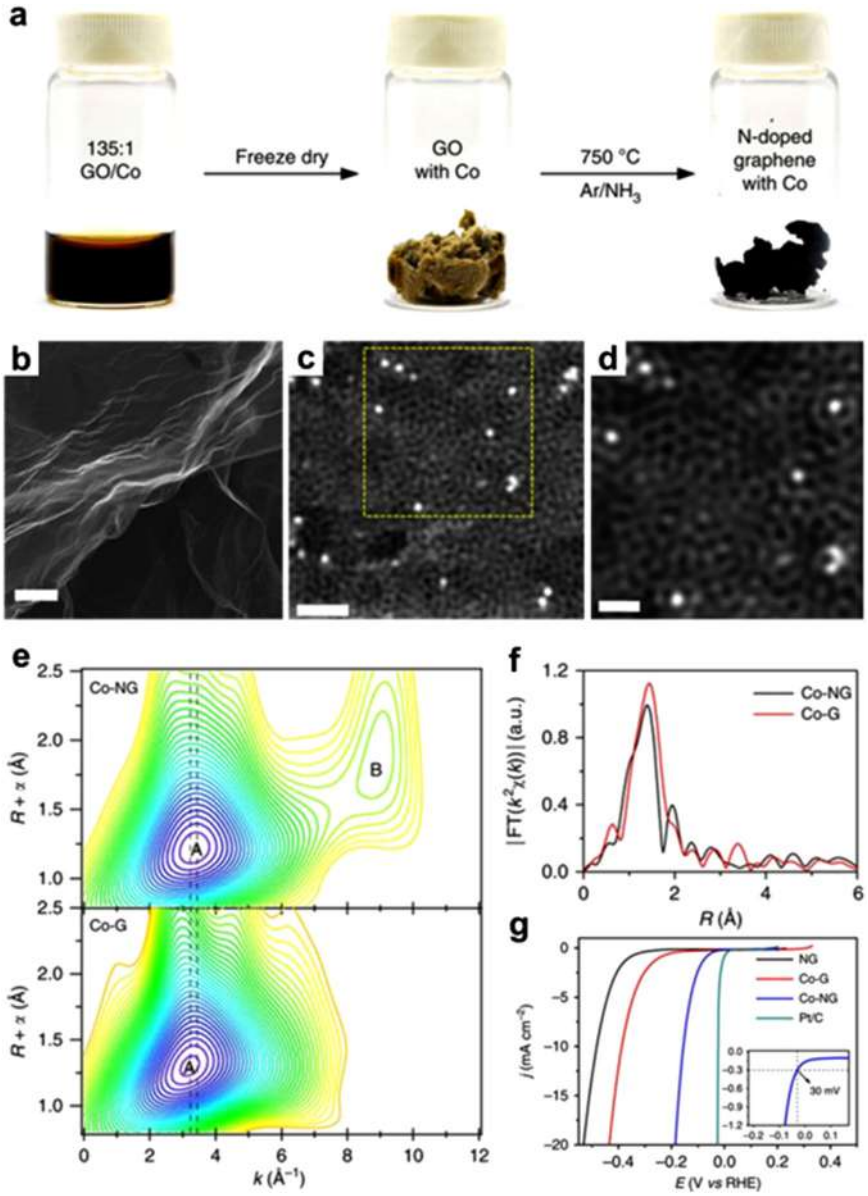

Fig. 26. (a) Schematic illustration of the synthetic procedure of the Co-NG catalyst. (b-c) SEM and HAADF-STEM images of the Co-NG nanosheets. Scale bar, (b) 2 μm, (c) 1 nm. (d) The enlarged view of the selected area in (c). Scale bar, 0.5 nm. (e) Wavelet transforms for the Co-NG and Co-G. (f) Fourier transformation of the EXAFS spectra in R space for the Co-NG and Co-G, respectively. (g) Liner sweep voltammetry (LSV) curves of various catalysts in 0.5 M H_2SO_4. The inset shows the enlarged view of the LSV for the Co-NG near the onset region. (Reproduced from Ref. [326] with permission from Nature Publishing Group, Copyright 2015).

active than others due to the low-coordination and unsaturated atoms containing valence electrons. But the surface free energy of metals increases remarkably as the particle size decreases, which would promote aggregation of small particles or clusters. Thus, using a suitable support material that strongly interacts with metal atoms to prevent this aggregation, and produces stable, finely dispersed metal atoms is a helpful method [63]. Lots of noble metal atoms, such as Pt [318–320], Au [321,322], and Pd [323,324], were supported on carbon nanomaterials for high electrocatalytic activity. A few studies about earth abundant transition metals were also conducted [325–327]. Among them, X. Yao et al. synthesized atomically isolated Ni species dispersed on graphitized carbon matrix through electrochemical activation [325]. The individual Ni atoms were anchored on the partially graphitized carbon. The activated-Ni-Carbon (A-Ni-C) electrocatalyst with a low overpotential of only η_{10} = 34 mV in 0.5 M H_2SO_4 was eventually obtained. Besides, Tour and co-workers reported isolated Co atoms dispersed on nitrogen-doped graphene (Co-NG) via facile heat treatment with the assistance of NH_3 atmosphere (Fig. 26a) [326]. As shown in Fig. 26b-d, the STEM images demonstrated the defective structures of the graphitic carbon support and the size of these bright dots is in the range of 2–3 Å. Based on the EXAFS analysis in Fig. 26f, no observed Co-Co interaction appeared in Co-NG, otherwise Co-N bond was detected. These results confirm that the light spot corresponds to isolated Co atoms, and the Co atoms were anchored on graphene surface by the bonding with nitrogen. Compared with the wavelet transform contour plots of Co-G in Fig. 26e, there was a small shift on the location of the maximum occurred on Co-NG, suggesting the presence of Co-N bonding. As expected, this catalyst is robust and highly active in aqueous media with low overpotential (Fig. 26g). The trends observed so far were focused on implanting single metal atoms (Ni, Co etc.) in 2D platforms such as graphene, g-C_3N_4, etc. Nowadays, substituting isolated metal atoms in the lattice of another metal atom has been introduced as plausible approach to accelerate water dissociation kinetics. Li and co-workers successfully synthesized atomically dispersed Co into Ru nanosheets

lattice as highly efficient HER electrocatalysts in alkaline solution [175]. Theoretical calculations indicated that single Co atom substitution in Ru lattice dramatically lower energy barrier of water decomposition. This electrocatalyst exhibited the superb HER performance in 1.0 M KOH (the overpotential of η_{10} = 13 mV and Tafel slope of 29 mV dec^{-1}), far superior than mere of CoRu alloy.

4.2. Binary and ternary alloys electrocatalysts

Previous studies have suggested that a combination of two or more non-noble metals from the two branches of the volcano curve (Fig. 4) could give rise to the enhancement in electrocatalytic activity [76,78,243,307,328–331]. The incorporation of other transition metals can modify the lattice parameters and electron density states of the metal catalyst to change the adsorption energies on the metal surface toward the optimal electrocatalytic activity [75,303,332,333]. Some recent advances also confirmed the remarkable electrochemical activity of binary and ternary alloys for hydrogen gas [307,309,334]. It is impressive that alloying nickel with other non-noble metals (e.g., Mo, W, Co etc.) have been commercialized as the cathodes for water electrolysis arising from their low cost, tunable electrocatalytic activity, favorable electrical conductivity, and excellent anti-corrosion capability [297,307,334–337]. Especially, Ni-Mo alloys [73,74,243,328,338,339] have been reported as the most active electrocatalysts for HER in alkaline electrolytes arising from the interaction between Ni and Mo via the *d*-orbital electron transfer, which made its surface electronic state similar to precious metal Pt. X. Sun and co-workers successfully synthesized ultrathin Ni-Mo alloy nanosheets by reducing the $NiMoO_4$ nanosheets array precursors under gentle conditions [309]. Benefiting from its ultrathin nanostructure and tailored composition, the as-obtained Ni-Mo nanosheets exhibited electrocatalytic activity almost similar with that of commercial Pt/C, requiring an overpotential of only η_{10} = 35 mV and Tafel slope of 45 mV dec^{-1} in 1 M KOH. Later, Feng et al. developed a highly active and stable $MoNi_4$ electrocatalyst supported by MoO_2 cuboids on nickel foam ($MoNi_4/MoO_2$@Ni), which was constructed by controlling the outward diffusion of Ni atoms on annealing $NiMoO_4$ precursor in H_2/Ar mixed atmosphere at 500 °C [73]. Fig. 27a-c reveals the SEM and HRTEM images of the heterostructured cuboids. The theoretical calculations revealed that the role of $NiMoO_4$ is the actual active center and can largely reduce energy barrier of the Volmer step (Fig. 27d). As a result, the as-prepared electrocatalyst exhibited superb electrocatalytic performance for HER, requiring zero onset overpotential and overpotential of only η_{10} = 15 mV, as well as a low Tafel slope of 30 mV dec^{-1} in alkaline electrolytes (Fig. 27e-f). Very recently, Adschiri et al. reported the synthesis of a porous Ni-Mo alloy covered by nanohole-sized holey nitrogen-doped graphene layers for HER in acidic electrolyte [307]. The nanohole fringes of the holey graphene enhance electrochemical activity and electrochemical stability.

What's more, the multi-metal alloys are also considered and studied. In this regard, F. Besenbacher et al. reported a composition-controlled Ni-Mo-Zn ternary alloy electrocatalyst via electrochemical deposition method [329]. Optimum amount (1–3 at%) of Zn was added to Ni-Mo in order to boost the intrinsic electrochemical activity of the electrocatalyst and efficiently facilitate the mass/electron transfer process. And Q. Chen et al. developed a universal method for synthesizing Fe-Co-Ni ternary alloys encapsulated in N-doped graphene via direct annealing of different MOFs [336]. They found that the variation of metal proportion in alloy would change the number of transferred electrons between alloy and graphene and the degree of freedom of alloys could affect their electrocatalytic properties.

5. Summary and outlook

In conclusion, continuing breakthroughs have been achieved for constructing non-noble metal based electrocatalysts beyond TMDs toward efficient electrochemical HER process in past few years. Experimental and theoretical works conducted so far in this particular

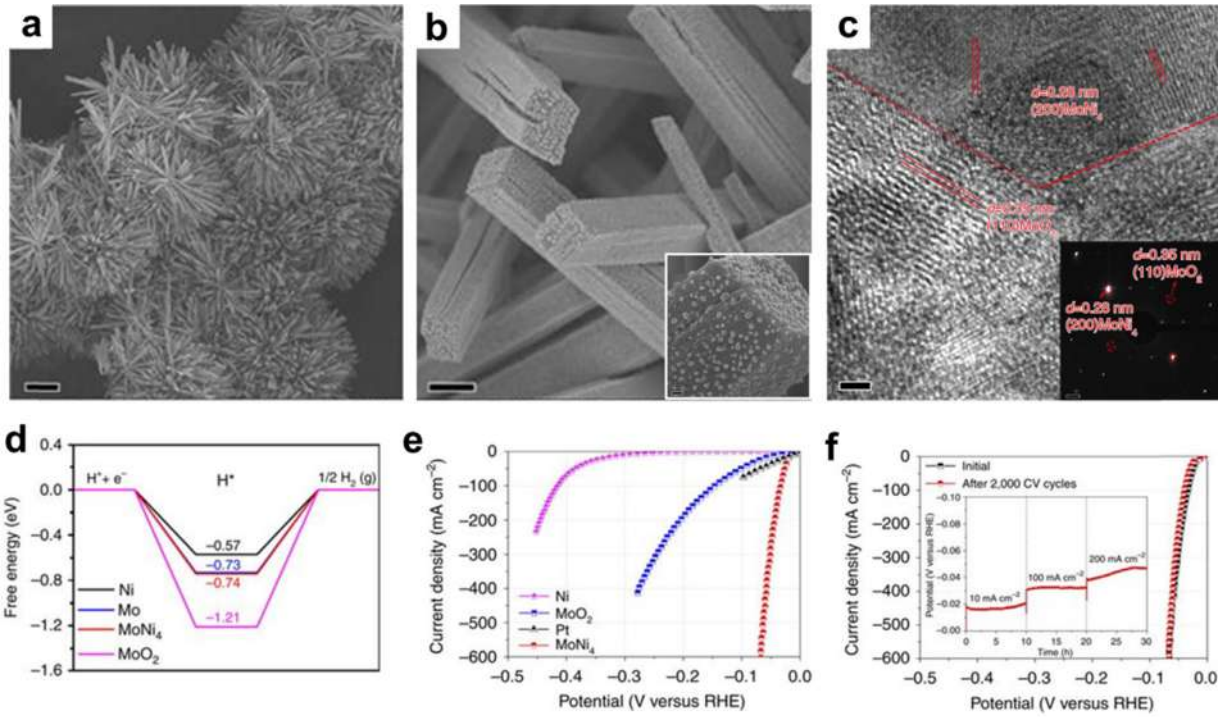

Fig. 27. (a-c) SEM and HRTEM images of $MoNi_4/MoO_2$@Ni. Scale bars, (a) 20 μm, (b) 1 μm, (c) 2 nm. (d) Calculated adsorption free energy diagram for the Tafel step. (e) Polarization curves of the $MoNi_4$ electrocatalyst supported by the MoO_2 cuboids, pure Ni nanosheets and MoO_2 cuboids on the nickel foam. (f) Polarization curves of the $MoNi_4$ electrocatalyst before and after 2000 cyclic voltammetry cycles. The inset shows the long-term stability tests of the $MoNi_4$ electrocatalyst at different current densities: 10, 100, and 200 mA cm^{-2}. (Reproduced from Ref. [73] with permission from Nature Publishing Group, Copyright 2017).

field reveal that the performance of a given catalyst depends on the extent of exposing active sites on the surface. In this context, the design of nanostructured materials finds a promising way for excellent performance in activity, stability and selectivity toward a given reaction. Moreover, catalysts should also be built from elementally abundant and less expensive materials for a wide-spread application. Maximal exposure of active sites based on entirely Earth abundant elements with controllability and large-area uniformity is an essential requirement for practical applications. This greatly depends on the development of facile and reliable synthesis methods; and (of course) adequate characterization tools. Tables 2–8 show different kinds of electrocatalysts based on transition metal phosphides (TMPs), carbides (TMCs), nitrides (TMNs), borides (TMBs), oxides (TMOs) and pure non-precious metal electrocatalysts for generating hydrogen gas. Inspired by the superior catalytic activity of platinum and the bio-enzymes, the prediction and regulation of HER electrocatalysts focus on resembling their electronic structure with that of platinum and active sites of bio-enzyme via DFT simulations and calculations. To this end, some experimental approaches, e.g., heteroatom doping, constructing heterostructures etc. were widely welcomed. Unfortunately, few studies have concentrated on the exploration and systematically understanding the intrinsic catalytic activity of these materials on atomic-scale level, which have been accomplished on Pt surface.

Under this condition, more attention should be devoted to gain further insight into these non-noble metal based electrocatalyst for a HER process. i) Some in-situ techniques, for example in-situ Raman and X-ray absorption spectra, should be developed to probe the interfacial structure and reconstructed surface during the electrochemical HER measurements. Notably, these novel techniques are powerful tool to detect the active sites experimentally. In this regard, the commonly employed electrolytes, including acidic, neutral and alkaline solution, also make a non-negligible difference owing to the existence of various intermediates (H_3O^+ or H_2O). For effectively realizing the establishment of HER routes on these non-noble metal based materials, the exposed facet and crystal structure have to be controlled. ii) Relying on the DFT calculations and in-situ experimental results, the reasonable models, which are closer to the real reaction systems, should be built to predict the reaction intermediates and HER mechanism on these electrocatalysts. Such fundamental understandings will be helpful for designing and optimizing these catalysts with more efficiency, as well as establishing structure-reactivity relationship on them. iii) From the perspective of practical application, the development of efficient HER electrocatalyst utilized in given electrolyte should be carefully considered. After comparing the catalytic activity of various materials in electrochemical hydrogen evolution, it is easy to find that the TMPs, TMCs, TMNs and TMBs are active and stable electrocatalysts for HER in a wide pH range. While, TMOs are usually used in alkaline electrolyte. iv) To integrate HER devices into other renewable power resource, such as solar energy, wind energy or tidal energy, careful design of setup configuration will have a profound industrial application value.

Acknowledgements

This work was supported by the National Natural Science Foundation of China (Nos. 61625401, 61474033, 61574050, 11674071, 21525523, 21722507 and 21805057), Ministry of Science and Technology of China (No. 2016YFA0200700), Strategic Priority Research Program of the Chinese Academy of Sciences (Grant No. XDA09040201), and CAS Key Laboratory of Nanosystem and Hierarchical Fabrication.

References

[1] M.S. Dresselhaus, I.L. Thomas, Nature 414 (2001) 332.
[2] J.A. Turner, Science 305 (2004) 972.
[3] H.B. Gray, Nat. Chem. 1 (2009) 7.
[4] N.S. Lewis, D.G. Nocera, Proc. Natl. Acad. Sci. USA 103 (2006) 15729.
[5] Y. Jiao, Y. Zheng, M. Jaroniec, S.Z. Qiao, Chem. Soc. Rev. 44 (2015) 2060–2086.
[6] D.G. Nocera, Acc. Chem. Res. 45 (2012) 767–776.
[7] L. Zhang, Q. Chang, H. Chen, M. Shao, Nano Energy 29 (2016) 198–219.
[8] R. Subbaraman, D. Tripkovic, K.C. Chang, D. Strmcnik, A.P. Paulikas, P. Hirunsit, M. Chan, J. Greeley, V. Stamenkovic, N.M. Markovic, Nat. Mater. 11 (2012) 550.
[9] M. Gong, D.Y. Wang, C.C. Chen, B.J. Hwang, H. Dai, Nano Res. 9 (2016) 28–46.
[10] P. Zhang, M. Wang, Y. Yang, T. Yao, H. Han, L. Sun, Nano Energy 19 (2016) 98–107.
[11] M.G. Walter, E.L. Warren, J.R. McKone, S.W. Boettcher, Q. Mi, E.A. Santori, N.S. Lewis, Chem. Rev. 110 (2010) 6446–6473.
[12] J.H. Wee, Renew Sust, Energy Rev. 11 (2007) 1720–1738.
[13] Z. Kang, G. Yang, J. Mo, Y. Li, S. Yu, D.A. Cullen, S.T. Retterer, T.J. Toops, G. Bender, B.S. Pivovar, J.B. Green, F.Y. Zhang, Nano Energy 47 (2018) 434–441.
[14] L. Pan, J.H. Kim, M.T. Mayer, M.K. Son, A. Ummadisingu, J.S. Lee, A. Hagfeldt, J. Luo, M. Grätzel, Nat. Catal. 1 (2018) 412–420.
[15] Y. Liu, C. Xiao, P. Huang, M. Cheng, Y. Xie, Chem 4 (2018) 1263–1283.
[16] H.I. Karunadasa, C.J. Chang, J.R. Long, Nature 464 (2010) 1329.
[17] D. Strmcnik, P.P. Lopes, B. Genorio, V.R. Stamenkovic, N.M. Markovic, Nano Energy 29 (2016) 29–36.
[18] M. Fang, W. Gao, G. Dong, Z. Xia, S. Yip, Y. Qin, Y. Qu, J.C. Ho, Nano Energy 27 (2016) 247–254.
[19] M. Chhowalla, H.S. Shin, G. Eda, L.J. Li, K.P. Loh, H. Zhang, Nat. Chem. 5 (2013) 263.
[20] X. Zou, Y. Zhang, Chem. Soc. Rev. 44 (2015) 5148–5180.
[21] F. Wang, T.A. Shifa, X. Zhan, Y. Huang, K. Liu, Z. Cheng, C. Jiang, J. He, Nanoscale 7 (2015) 19764–19788.
[22] S. Jiang, Z. Zhang, N. Zhang, Y. Huan, Y. Gong, M. Sun, J. Shi, C. Xie, P. Yang, Q. Fang, H. Li, L. Tong, D. Xie, L. Gu, P. Liu, Y. Zhang, Nano Res. 11 (2018) 1787–1797.
[23] S. Jiang, M. Hong, W. Wei, L. Zhao, N. Zhang, Z. Zhang, P. Yang, N. Gao, X. Zhou, C. Xie, J. Shi, Y. Huan, L. Tong, J. Zhao, Q. Zhang, Q. Fu, Y. Zhang, Commun. Chem. 1 (2018) 17.
[24] T.F. Jaramillo, K.P. Jørgensen, J. Bonde, J.H. Nielsen, S. Horch, I. Chorkendorff, Science 317 (2007) 100.
[25] B. Hinnemann, P.G. Moses, J. Bonde, K.P. Jørgensen, J.H. Nielsen, S. Horch, I. Chorkendorff, J.K. Nørskov, J. Am. Chem. Soc. 127 (2005) 5308–5309.
[26] D. Voiry, J. Yang, M. Chhowalla, Adv. Mater. 28 (2016) 6197–6206.
[27] Z. Zhang, W. Li, M.F. Yuen, T.W. Ng, Y. Tang, C.S. Lee, X. Chen, W. Zhang, Nano Energy 18 (2015) 196–204.
[28] Q. Wang, Z.L. Zhao, S. Dong, D. He, M.J. Lawrence, S. Han, C. Cai, S. Xiang, P. Rodriguez, B. Xiang, Z. Wang, Y. Liang, M. Gu, Nano Energy 53 (2018) 458–467.
[29] Y.R. An, X.L. Fan, Z.F. Luo, W.M. Lau, Nano Lett. 17 (2017) 368–376.
[30] H. Wang, Q. Zhang, H. Yao, Z. Liang, H.W. Lee, P.C. Hsu, G. Zheng, Y. Cui, Nano Lett. 14 (2014) 7138–7144.
[31] X. Wang, X. Liu, D. Yin, Y. Ke, M.T. Swihart, Chem. Mater. 27 (2015) 3378–3388.
[32] K. Chang, X. Hai, H. Pang, H. Zhang, L. Shi, G. Liu, H. Liu, G. Zhao, M. Li, J. Ye, Adv. Mater. 28 (2016) 10033–10041.
[33] B. Seo, D.S. Baek, Y.J. Sa, S.H. Joo, CrystEngComm 18 (2016) 6083–6089.
[34] G. Ye, Y. Gong, J. Lin, B. Li, Y. He, S.T. Pantelides, W. Zhou, R. Vajtai, P.M. Ajayan, Nano Lett. 16 (2016) 1097–1103.
[35] Y.H. Li, P.F. Liu, L.F. Pan, H.F. Wang, Z.Z. Yang, L.R. Zheng, P. Hu, H.J. Zhao, L. Gu, H.G. Yang, Nat. Commun. 6 (2015) 8064.
[36] C. Tsai, H. Li, S. Park, J. Park, H.S. Han, J.K. Nørskov, X. Zheng, F. Abild-Pedersen, Nat. Commun. 8 (2017) 15113.
[37] Y. Tong, Y. Guo, K. Mu, H. Shan, J. Dai, Y. Liu, Z. Sun, A. Zhao, X.C. Zeng, C. Wu, Y. Xie, Adv. Mater. 29 (2017) 1703123.
[38] D. Voiry, H. Yamaguchi, J. Li, R. Silva, D.C.B. Alves, T. Fujita, M. Chen, T. Asefa, V.B. Shenoy, G. Eda, M. Chhowalla, Nat. Mater. 12 (2013) 850.
[39] J. Kibsgaard, C. Tsai, K. Chan, J.D. Benck, J.K. Nørskov, F. Abild-Pedersen, T.F. Jaramillo, Energy Environ. Sci. 8 (2015) 3022–3029.
[40] J. Xie, J. Zhang, S. Li, F. Grote, X. Zhang, H. Zhang, R. Wang, Y. Lei, B. Pan, Y. Xie, J. Am. Chem. Soc. 135 (2013) 17881–17888.
[41] J. Pető, T. Ollár, P. Vancsó, Z.I. Popov, G.Z. Magda, G. Dobrik, C. Hwang, P.B. Sorokin, L. Tapasztó, Nat. Chem. (2018), https://doi.org/10.1038/s41557-018-0136-2.
[42] Y. Zhou, E. Song, J. Zhou, J. Lin, R. Ma, Y. Wang, W. Qiu, R. Shen, K. Suenaga, Q. Liu, J. Wang, Z. Liu, J. Liu, ACS Nano 12 (2018) 4486–4493.
[43] Q. Ji, Y. Zhang, J. Shi, J. Sun, Y. Zhang, Z. Liu, Adv. Mater. 28 (2016) 6207–6212.
[44] D.C. Phillips, S.J. Sawhill, R. Self, M.E. Bussell, J. Catal. 207 (2002) 266–273.
[45] V.M.L. Whiffen, K.J. Smith, Energy Fuel. 24 (2010) 4728–4737.
[46] L. Lukovstev, Acta Physicochim. USSR 11 (1939) 21.
[47] I. Paseka, Electrochim. Acta 40 (1995) 1633–1640.
[48] P. Liu, J.A. Rodriguez, J. Am. Chem. Soc. 127 (2005) 14871–14878.
[49] A.B. Laursen, K.R. Patraju, M.J. Whitaker, M. Retuerto, T. Sarkar, N. Yao, K.V. Ramanujachary, M. Greenblatt, G.C. Dismukes, Energy Environ. Sci. 8 (2015) 1027–1034.
[50] Y. Liu, G. Yu, G.D. Li, Y. Sun, T. Asefa, W. Chen, X. Zou, Angew. Chem. Int. Ed. 127 (2015) 10902–10907.
[51] H.B. Wu, B.Y. Xia, L. Yu, X.Y. Yu, X.W. Lou, Nat. Commun. 6 (2015) 6512.
[52] H.W. Liang, S. Brüller, R. Dong, J. Zhang, X. Feng, K. Müllen, Nat. Commun. 6 (2015) 7992.
[53] T. Wang, X. Wang, Y. Liu, J. Zheng, X. Li, Nano Energy 22 (2016) 111–119.
[54] H. Yan, Y. Xie, Y. Jiao, A. Wu, C. Tian, X. Zhang, L. Wang, H. Fu, Adv. Mater. 30 (2017) 1704156.

[55] J.E. Houston, G.E. Laramore, R.L. Park, Science 185 (1974) 258.
[56] A. Taylor, M. Mamelak, E. Reaven, R. Maffly, Science 181 (1973) 347.
[57] L.I. Johansson, Surf. Sci. Rep. 21 (1995) 177–250.
[58] M. Rosenbaum, F. Zhao, U. Schröder, F. Scholz, Angew. Chem. Int. Ed. 45 (2006) 6658–6661.
[59] A. Kundu, J.N. Sahu, G. Redzwan, M.A. Hashim, Int. J. Hydrog. Energy 38 (2013) 1745–1757.
[60] Y. Zhao, K. Kamiya, K. Hashimoto, S. Nakanishi, J. Am. Chem. Soc. 137 (2015) 110–113.
[61] F.X. Ma, H.B. Wu, B.Y. Xia, C.Y. Xu, X.W. Lou, Angew. Chem. Int. Ed. 127 (2015) 15615–15619.
[62] J.S. Li, Y. Wang, C.H. Liu, S.L. Li, Y.G. Wang, L.Z. Dong, Z.H. Dai, Y.F. Li, Y.Q. Lan, Nat. Commun. 7 (2016) 11204.
[63] D.H. Youn, S. Han, J.Y. Kim, J.Y. Kim, H. Park, S.H. Choi, J.S. Lee, ACS Nano 8 (2014) 5164–5173.
[64] L. Ma, L.R.L. Ting, V. Molinari, C. Giordano, B.S. Yeo, J. Mater. Chem. A 3 (2015) 8361–8368.
[65] Y. Zhu, G. Chen, X. Xu, G. Yang, M. Liu, Z. Shao, ACS Catal. 7 (2017) 3540–3547.
[66] H. Jin, X. Liu, Y. Jiao, A. Vasileff, Y. Zheng, S.Z. Qiao, Nano Energy 53 (2018) 690–697.
[67] S. Jing, J. Lu, G. Yu, S. Yin, L. Luo, Z. Zhang, Y. Ma, W. Chen, P.K. Shen, Adv. Mater. 30 (2018) 1705979.
[68] M. Gong, W. Zhou, M.C. Tsai, J. Zhou, M. Guan, M.C. Lin, B. Zhang, Y. Hu, D.Y. Wang, J. Yang, S.J. Pennycook, B.J. Hwang, H. Dai, Nat. Commun. 5 (2014) 4695.
[69] W. Hao, R. Wu, R. Zhang, Y. Ha, Z. Chen, L. Wang, Y. Yang, X. Ma, D. Sun, F. Fang, Y. Guo, Adv. Energy Mater. 8 (2018) 1801372.
[70] Y.J. Tang, M.R. Gao, C.H. Liu, S.L. Li, H.L. Jiang, Y.Q. Lan, M. Han, S.H. Yu, Angew. Chem. Int. Ed. 127 (2015) 13120–13124.
[71] H. Park, A. Encinas, J.P. Scheifers, Y. Zhang, B.P.T. Fokwa, Angew. Chem. Int. Ed. 56 (2017) 5575–5578.
[72] T. Wang, Y. Guo, Z. Zhou, X. Chang, J. Zheng, X. Li, ACS Nano 10 (2016) 10397–10403.
[73] J. Zhang, T. Wang, P. Liu, Z. Liao, S. Liu, X. Zhuang, M. Chen, E. Zschech, X. Feng, Nat. Commun. 8 (2017) 15437.
[74] P.M. Csernica, J.R. McKone, C.R. Mulzer, W.R. Dichtel, H.D. Abruña, F.J. DiSalvo, ACS Catal. 7 (2017) 3375–3383.
[75] J. Deng, P. Ren, D. Deng, L. Yu, F. Yang, X. Bao, Energy Environ. Sci. 7 (2014) 1919–1923.
[76] Y. Yang, Z. Lun, G. Xia, F. Zheng, M. He, Q. Chen, Energy Environ. Sci. 8 (2015) 3563–3571.
[77] B.E. Conway, B.V. Tilak, Electrochim. Acta 47 (2002) 3571–3594.
[78] C.G. Morales-Guio, L.A. Stern, X. Hu, Chem. Soc. Rev. 43 (2014) 6555–6569.
[79] W. Sheng, H.A. Gasteiger, Y. Shao-Horn, J. Electrochem. Soc. 157 (2010) B1529–B1536.
[80] Y. Zheng, Y. Jiao, M. Jaroniec, S.Z. Qiao, Angew. Chem. Int. Ed. 54 (2014) 52–65.
[81] Y. Zheng, Y. Jiao, A. Vasileff, S.Z. Qiao, Angew. Chem. Int. Ed. 57 (2017) 7568–7579.
[82] G. Chen, T. Wang, J. Zhang, P. Liu, H. Sun, X. Zhuang, M. Chen, X. Feng, Adv. Mater. 30 (2018) 1706279.
[83] P. Sabatier, Ber. Dtsch. Chem. Ges. 44 (1911) 1984–2001.
[84] J.X. Feng, J.Q. Wu, Y.X. Tong, G.R. Li, J. Am. Chem. Soc. 140 (2018) 610–617.
[85] E.M. Fernández, P.G. Moses, A. Toftelund, H.A. Hansen, J.I. Martínez, F. Abild-Pedersen, J. Kleis, B. Hinnemann, J. Rossmeisl, T. Bligaard, J.K. Nørskov, Angew. Chem. Int. Ed. 120 (2008) 4761–4764.
[86] R. Wu, J. Zhang, Y. Shi, D. Liu, B. Zhang, J. Am. Chem. Soc. 137 (2015) 6983–6986.
[87] J.K. Nørskov, T. Bligaard, A. Logadottir, J.R. Kitchin, J.G. Chen, S. Pandelov, U. Stimming, J. Electrochem. Soc. 152 (2005) J23–J26.
[88] D. Voiry, M. Chhowalla, Y. Gogotsi, N.A. Kotov, Y. Li, R.M. Penner, R.E. Schaak, P.S. Weiss, ACS Nano 12 (2018) 9635–9638.
[89] J. Greeley, T.F. Jaramillo, J. Bonde, I. Chorkendorff, J.K. Nørskov, Nat. Mater. 5 (2006) 909.
[90] J. Wang, F. Xu, H. Jin, Y. Chen, Y. Wang, Adv. Mater. 29 (2017) 1605838.
[91] Y. Shi, B. Zhang, Chem. Soc. Rev. 45 (2016) 1529–1541.
[92] J.O.M. Bockris, E.C. Potter, J. Electrochem. Soc. 99 (1952) 169–186.
[93] S. Fletcher, J. Solid, State Electr. 13 (2009) 537–549.
[94] S. Trasatti, O.A. Petrii, J. Electroanal. Chem. 327 (1992) 353–376.
[95] Y.Y. Ma, C.X. Wu, X.J. Feng, H.Q. Tan, L.K. Yan, Y. Liu, Z.H. Kang, E.B. Wang, Y.G. Li, Energy Environ. Sci. 10 (2017) 788–798.
[96] T. Zhang, K. Yang, C. Wang, S. Li, Q. Zhang, X. Chang, J. Li, S. Li, S. Jia, J. Wang, L. Fu, Adv. Energy Mater. 8 (2018) 1801690.
[97] Z. Fang, L. Peng, Y. Qian, X. Zhang, Y. Xie, J.J. Cha, G. Yu, J. Am. Chem. Soc. 140 (2018) 5241–5247.
[98] F. Yu, H. Zhou, Y. Huang, J. Sun, F. Qin, J. Bao, W.A. Goddard Iii, S. Chen, Z. Ren, Nat. Commun. 9 (2018) 2551.
[99] P. Xiao, W. Chen, X. Wang, Adv. Energy Mater. 5 (2015) 1500985.
[100] P. Xiao, M.A. Sk, L. Thia, X. Ge, R.J. Lim, J.Y. Wang, K.H. Lim, X. Wang, Energy Environ. Sci. 7 (2014) 2624–2629.
[101] Y. Pan, Y. Liu, J. Zhao, K. Yang, J. Liang, D. Liu, W. Hu, D. Liu, Y. Liu, C. Liu, J. Mater. Chem. A 3 (2015) 1656–1665.
[102] J.F. Callejas, C.G. Read, E.J. Popczun, J.M. McEnaney, R.E. Schaak, Chem. Mater. 27 (2015) 3769–3774.
[103] P.E.R. Blanchard, A.P. Grosvenor, R.G. Cavell, A. Mar, Chem. Mater. 20 (2008) 7081–7088.
[104] X. Wang, Y.V. Kolen'ko, X.Q. Bao, K. Kovnir, L. Liu, Angew. Chem. Int. Ed. 127 (2015) 8306–8310.
[105] E. Muthuswamy, P.R. Kharel, G. Lawes, S.L. Brock, ACS Nano 3 (2009) 2383–2393.
[106] P. Jiang, Q. Liu, C. Ge, W. Cui, Z. Pu, A.M. Asiri, X. Sun, J. Mater. Chem. A 2 (2014) 14634–14640.
[107] H. Yang, Y. Zhang, F. Hu, Q. Wang, Nano Lett. 15 (2015) 7616–7620.
[108] Z. Xing, Q. Liu, A.M. Asiri, X. Sun, Adv. Mater. 26 (2014) 5702–5707.
[109] Z. Pu, Q. Liu, A.M. Asiri, X. Sun, ACS Appl. Mater. Interfaces 6 (2014) 21874–21879.
[110] T. Wu, M. Pi, X. Wang, W. Guo, D. Zhang, S. Chen, J. Alloy. Compd. 729 (2017) 203–209.
[111] J.F. Callejas, J.M. McEnaney, C.G. Read, J.C. Crompton, A.J. Biacchi, E.J. Popczun, T.R. Gordon, N.S. Lewis, R.E. Schaak, ACS Nano 8 (2014) 11101–11107.
[112] E.J. Popczun, C.G. Read, C.W. Roske, N.S. Lewis, R.E. Schaak, Angew. Chem. Int. Ed. 53 (2014) 5427–5430.
[113] E.J. Popczun, J.R. McKone, C.G. Read, A.J. Biacchi, A.M. Wiltrout, N.S. Lewis, R.E. Schaak, J. Am. Chem. Soc. 135 (2013) 9267–9270.
[114] P. Jiang, Q. Liu, Y. Liang, J. Tian, A.M. Asiri, X. Sun, Angew. Chem. Int. Ed. 126 (2014) 13069–13073.
[115] Q. Liu, J. Tian, W. Cui, P. Jiang, N. Cheng, A.M. Asiri, X. Sun, Angew. Chem. Int. Ed. 53 (2014) 6710–6714.
[116] Z. Xing, Q. Liu, A.M. Asiri, X. Sun, ACS Catal. 5 (2015) 145–149.
[117] J. Jiang, C. Wang, J. Zhang, W. Wang, X. Zhou, B. Pan, K. Tang, J. Zuo, Q. Yang, J. Mater. Chem. A 3 (2015) 499–503.
[118] A.B. Laursen, R.B. Wexler, M.J. Whitaker, E.J. Izett, K.U.D. Calvinho, S. Hwang, R. Rucker, H. Wang, J. Li, E. Garfunkel, M. Greenblatt, A.M. Rappe, G.C. Dismukes, ACS Catal. 8 (2018) 4408–4419.
[119] M. Pi, T. Wu, D. Zhang, S. Chen, S. Wang, Nanoscale 8 (2016) 19779–19786.
[120] J.F. Callejas, C.G. Read, C.W. Roske, N.S. Lewis, R.E. Schaak, Chem. Mater. 28 (2016) 6017–6044.
[121] M. Chen, J. Qi, W. Zhang, R. Cao, Chem. Commun. 53 (2017) 5507–5510.
[122] M. Ledendecker, H. Schlott, M. Antonietti, B. Meyer, M. Shalom, Adv. Energy Mater. 7 (2016) 1601735.
[123] P. Jiang, Q. Liu, X. Sun, Nanoscale 6 (2014) 13440–13445.
[124] Z. Huang, Z. Chen, Z. Chen, C. Lv, H. Meng, C. Zhang, ACS Nano 8 (2014) 8121–8129.
[125] C.H. Lin, C.L. Chen, J.H. Wang, J. Phys. Chem. C 115 (2011) 18582–18588.
[126] J. Tian, Q. Liu, A.M. Asiri, X. Sun, J. Am. Chem. Soc. 136 (2014) 7587–7590.
[127] C. Zhang, Y. Huang, Y. Yu, J. Zhang, S. Zhuo, B. Zhang, Chem. Sci. 8 (2017) 2769–2775.
[128] C. Ye, M.Q. Wang, G. Chen, Y.H. Deng, L.J. Li, H.Q. Luo, N.B. Li, J. Mater. Chem. A 5 (2017) 7791–7795.
[129] J. Wang, W. Yang, J. Liu, J. Mater. Chem. A 4 (2016) 4686–4690.
[130] T. Wu, M. Pi, X. Wang, D. Zhang, S. Chen, Phys. Chem. Chem. Phys. 19 (2017) 2104–2110.
[131] Z. Jin, P. Li, D. Xiao, Green Chem. 18 (2016) 1459–1464.
[132] J.X. Feng, S.Y. Tong, Y.X. Tong, G.R. Li, J. Am. Chem. Soc. 140 (2018) 5118–5126.
[133] E.J. Popczun, C.W. Roske, C.G. Read, J.C. Crompton, J.M. McEnaney, J.F. Callejas, N.S. Lewis, R.E. Schaak, J. Mater. Chem. A 3 (2015) 5420–5425.
[134] T. Liu, X. Ma, D. Liu, S. Hao, G. Du, Y. Ma, A.M. Asiri, X. Sun, L. Chen, ACS Catal. 7 (2017) 98–102.
[135] Z. Huang, Z. Chen, Z. Chen, C. Lv, M.G. Humphrey, C. Zhang, Nano Energy 9 (2014) 373–382.
[136] D. Voiry, H.S. Shin, K.P. Loh, M. Chhowalla, Nat. Rev. Chem. 2 (2018) 0105.
[137] Y. Xu, R. Wu, J. Zhang, Y. Shi, B. Zhang, Chem. Commun. 49 (2013) 6656–6658.
[138] D.E. Schipper, Z. Zhao, H. Thirumalai, A.P. Leitner, S.L. Donaldson, A. Kumar, F. Qin, Z. Wang, L.C. Grabow, J. Bao, K.H. Whitmire, Chem. Mater. 30 (2018) 3588–3598.
[139] D.Y. Chung, S.W. Jun, G. Yoon, H. Kim, J.M. Yoo, K.S. Lee, T. Kim, H. Shin, A.K. Sinha, S.G. Kwon, K. Kang, T. Hyeon, Y.E. Sung, J. Am. Chem. Soc. 139 (2017) 6669–6674.
[140] Z. Zhang, G. Yu, H. Li, J. Liu, X. Huang, W. Chen, Phys. Chem. Chem. Phys. 20 (2018) 10407–10417.
[141] A. Han, H. Zhang, R. Yuan, H. Ji, P. Du, ACS Appl. Mater. Interfaces 9 (2017) 2240–2248.
[142] J. Tian, Q. Liu, N. Cheng, A.M. Asiri, X. Sun, Angew. Chem. Int. Ed. 126 (2014) 9731–9735.
[143] R. Wang, X.Y. Dong, J. Du, J.Y. Zhao, S.Q. Zang, Adv. Mater. 30 (2017) 1703711.
[144] X. Ma, Y. Chang, Z. Zhang, J. Tang, J. Mater. Chem. A 6 (2018) 2100–2106.
[145] L. Ma, X. Shen, H. Zhou, J. Zhu, C. Xi, Z. Ji, L. Kong, RSC Adv. 6 (2016) 9672–9677.
[146] J. Hao, W. Yang, Z. Huang, C. Zhang, Adv. Mater. Interfaces 3 (2016) 1600236.
[147] H. Du, X. Zhang, Q. Tan, R. Kong, F. Qu, Chem. Commun. 53 (2017) 12012–12015.
[148] D. Li, Q. Liao, B. Ren, Q. Jin, H. Cui, C. Wang, J. Mater. Chem. A 5 (2017) 11301–11308.
[149] X. Zhang, X. Yu, L. Zhang, F. Zhou, Y. Liang, R. Wang, Adv. Funct. Mater. 28 (2018) 1706523.
[150] J. Yang, F. Zhang, X. Wang, D. He, G. Wu, Q. Yang, X. Hong, Y. Wu, Y. Li, Angew. Chem. Int. Ed. 55 (2016) 12854–12858.
[151] J.S. Li, J.Q. Sha, B. Du, B. Tang, Chem. Commun. 53 (2017) 12576–12579.
[152] X. Liu, L. Zhang, M. Li, X. Hu, Chem. Commun. 54 (2018) 2502–2505.
[153] J.M. McEnaney, J.C. Crompton, J.F. Callejas, E.J. Popczun, A.J. Biacchi, N.S. Lewis, R.E. Schaak, Chem. Mater. 26 (2014) 4826–4831.
[154] G. Zhang, G. Wang, Y. Liu, H. Liu, J. Qu, J. Li, J. Am. Chem. Soc. 138 (2016)

14686–14693.
[155] Z. Pu, I. Saana Amiinu, M. Wang, Y. Yang, S. Mu, Nanoscale 8 (2016) 8500–8504.
[156] C. Huang, C. Pi, X. Zhang, K. Ding, P. Qin, J. Fu, X. Peng, B. Gao, P.K. Chu, K. Huo, Small 14 (2018) 1870115.
[157] J. Jia, W. Zhou, G. Li, L. Yang, Z. Wei, L. Cao, Y. Wu, K. Zhou, S. Chen, ACS Appl. Mater. Interfaces 9 (2017) 8041–8046.
[158] C. Deng, F. Ding, X. Li, Y. Guo, W. Ni, H. Yan, K. Sun, Y.M. Yan, J. Mater. Chem. A 4 (2016) 59–66.
[159] R. Prins, M.E. Bussell, Catal. Lett. 142 (2012) 1413–1436.
[160] Q. Guan, W. Li, J. Catal. 271 (2010) 413–415.
[161] S.T. Oyama, J. Catal. 216 (2003) 343–352.
[162] Y. Ma, G. Yu, T. Wang, C. Zhang, X. Huang, W. Chen, Phys. Chem. Chem. Phys. 20 (2018) 13757–13764.
[163] H. Du, S. Gu, R. Liu, C.M. Li, J. Power Sources 278 (2015) 540–545.
[164] J.M. McEnaney, J. Chance Crompton, J.F. Callejas, E.J. Popczun, C.G. Read, N.S. Lewis, R.E. Schaak, Chem. Commun. 50 (2014) 11026–11028.
[165] Z. Pu, X. Ya, I.S. Amiinu, Z. Tu, X. Liu, W. Li, S. Mu, J. Mater. Chem. A 4 (2016) 15327–15332.
[166] Z. Wu, X. Li, W. Liu, Y. Zhong, Q. Gan, X. Li, H. Wang, ACS Catal. 7 (2017) 4026–4032.
[167] J. Zhuo, M. Cabán-Acevedo, H. Liang, L. Samad, Q. Ding, Y. Fu, M. Li, S. Jin, ACS Catal. 5 (2015) 6355–6361.
[168] N.Q. Tran, V.Q. Bui, H.M. Le, Y. Kawazoe, H. Lee, Adv. Energy Mater. 8 (2018) 1702139.
[169] W. Gu, L. Gan, X. Zhang, E. Wang, J. Wang, Nano Energy 34 (2017) 421–427.
[170] J. Hu, C. Zhang, X. Meng, H. Lin, C. Hu, X. Long, S. Yang, J. Mater. Chem. A 5 (2017) 5995–6012.
[171] T. Wu, M.L. Stone, M.J. Shearer, M.J. Stolt, I.A. Guzei, R.J. Hamers, R. Lu, K. Deng, S. Jin, J.R. Schmidt, ACS Catal. 8 (2018) 1143–1152.
[172] J.L. Lado, X. Wang, E. Paz, E. Carbó-Argibay, N. Guldris, C. Rodríguez-Abreu, L. Liu, K. Kovnir, Y.V. Kolen'ko, ACS Catal. 5 (2015) 6503–6508.
[173] T.A. Shifa, F. Wang, K. Liu, Z. Cheng, K. Xu, Z. Wang, X. Zhan, C. Jiang, J. He, Small 13 (2017) 1603706.
[174] K. Liu, F. Wang, T.A. Shifa, Z. Wang, K. Xu, Y. Zhang, Z. Cheng, X. Zhan, J. He, Nanoscale 9 (2017) 3995–4001.
[175] F. Wang, T.A. Shifa, P. Yu, P. He, Y. Liu, F. Wang, Z. Wang, X. Zhan, X. Lou, F. Xia, J. He, Adv. Funct. Mater. 28 (2018) 1802151.
[176] J. Mao, C.T. He, J. Pei, W. Chen, D. He, Y. He, Z. Zhuang, C. Chen, Q. Peng, D. Wang, Y. Li, Nat. Commun. 9 (2018) 4958.
[177] C. Tang, L. Gan, R. Zhang, W. Lu, X. Jiang, A.M. Asiri, X. Sun, J. Wang, L. Chen, Nano Lett. 16 (2016) 6617–6621.
[178] W. Liu, E. Hu, H. Jiang, Y. Xiang, Z. Weng, M. Li, Q. Fan, X. Yu, E.I. Altman, H. Wang, Nat. Commun. 7 (2016) 10771.
[179] M. Cabán-Acevedo, M.L. Stone, J.R. Schmidt, J.G. Thomas, Q. Ding, H.C. Chang, M.L. Tsai, J.H. He, S. Jin, Nat. Mater. 14 (2015) 1245.
[180] J. Kibsgaard, T.F. Jaramillo, Angew. Chem. Int. Ed. 53 (2014) 14433–14437.
[181] R. Ye, P. del Angel-Vicente, Y. Liu, M.J. Arellano-Jimenez, Z. Peng, T. Wang, Y. Li, B.I. Yakobson, S.H. Wei, M.J. Yacaman, J.M. Tour, Adv. Mater. 28 (2015) 1427–1432.
[182] Y. Liu, T.G. Kelly, J.G. Chen, W.E. Mustain, ACS Catal. 3 (2013) 1184–1194.
[183] S. Meyer, A.V. Nikiforov, I.M. Petrushina, K. Köhler, E. Christensen, J.O. Jensen, N.J. Bjerrum, Int. J. Hydrog. Energy 40 (2015) 2905–2911.
[184] Z.W. Seh, K.D. Fredrickson, B. Anasori, J. Kibsgaard, A.L. Strickler, M.R. Lukatskaya, Y. Gogotsi, T.F. Jaramillo, A. Vojvodic, ACS Energy Lett. 1 (2016) 589–594.
[185] Y. Huang, J. Ge, J. Hu, J. Zhang, J. Hao, Y. Wei, Adv. Energy Mater. 8 (2017) 1701601.
[186] P. Xiao, X. Ge, H. Wang, Z. Liu, A. Fisher, X. Wang, Adv. Funct. Mater. 25 (2015) 1520–1526.
[187] X. Wu, Z. Wang, M. Yu, L. Xiu, J. Qiu, Adv. Mater. 29 (2017) 1607017.
[188] H. Wang, Y. Wu, X. Yuan, G. Zeng, J. Zhou, X. Wang, J.W. Chew, Adv. Mater. 30 (2018) 1704561.
[189] H. Zhang, Z. Ma, G. Liu, L. Shi, J. Tang, H. Pang, K. Wu, T. Takei, J. Zhang, Y. Yamauchi, J. Ye, NPG Asia Mater. 8 (2016) e293.
[190] M.G. Quesne, A. Roldan, N.H. de Leeuw, C.R.A. Catlow, Phys. Chem. Chem. Phys. 20 (2018) 6905–6916.
[191] S.T. Oyama, Catal. Today 15 (1992) 179–200.
[192] H.H. Hwu, J.G. Chen, Chem. Rev. 105 (2005) 185–212.
[193] W.F. Chen, J.T. Muckerman, E. Fujita, Chem. Commun. 49 (2013) 8896–8909.
[194] J.D. Ham, S.J. Lee, Energies 2 (2009) 873–899.
[195] E.V. Matus, I.Z. Ismagilov, O.B. Sukhova, V.I. Zaikovskii, L.T. Tsikoza, Z.R. Ismagilov, J.A. Moulijn, Ind. Eng. Chem. Res. 46 (2007) 4063–4074.
[196] D. Geng, X. Zhao, Z. Chen, W. Sun, W. Fu, J. Chen, W. Liu, W. Zhou, K.P. Loh, Adv. Mater. 29 (2017) 1700072.
[197] H. Lin, N. Liu, Z. Shi, Y. Guo, Y. Tang, Q. Gao, Adv. Funct. Mater. 26 (2016) 5590–5598.
[198] L. Zhang, H. Yang, D.K.J.A. Wanigarathna, B. Liu, Small Methods 2 (2018) 1700353.
[199] Y. Huang, Q. Gong, X. Song, K. Feng, K. Nie, F. Zhao, Y. Wang, M. Zeng, J. Zhong, Y. Li, ACS Nano 10 (2016) 11337–11343.
[200] R. Ma, Y. Zhou, Y. Chen, P. Li, Q. Liu, J. Wang, Angew. Chem. Int. Ed. 127 (2015) 14936–14940.
[201] Q. Gong, Y. Wang, Q. Hu, J. Zhou, R. Feng, P.N. Duchesne, P. Zhang, F. Chen, N. Han, Y. Li, C. Jin, Y. Li, S.T. Lee, Nat. Commun. 7 (2016) 13216.
[202] R.B. Levy, M. Boudart, Science 181 (1973) 547.
[203] Z. Pu, I.S. Amiinu, S. Mu, Energy Technol. 4 (2016) 1030–1034.
[204] X.D. Wang, Y.F. Xu, H.S. Rao, W.J. Xu, H.Y. Chen, W.X. Zhang, D.B. Kuang, C.Y. Su, Energy Environ. Sci. 9 (2016) 1468–1475.
[205] M.L. Frauwallner, F. López-Linares, J. Lara-Romero, C.E. Scott, V. Ali, E. Hernández, P. Pereira-Almao, Appl. Catal. A 394 (2011) 62–70.
[206] N. Ji, T. Zhang, M. Zheng, A. Wang, H. Wang, X. Wang, J.G. Chen, Angew. Chem. Int. Ed. 120 (2008) 8638–8641.
[207] D.V. Esposito, S.T. Hunt, A.L. Stottlemyer, K.D. Dobson, B.E. McCandless, R.W. Birkmire, J.G. Chen, Angew. Chem. Int. Ed. 49 (2010) 9859–9862.
[208] G. Bianchi, F. Mazza, S. Trasatti, Z. Phys. Chem. 226 (1964) 40–58.
[209] N. Han, K.R. Yang, Z. Lu, Y. Li, W. Xu, T. Gao, Z. Cai, Y. Zhang, V.S. Batista, W. Liu, X. Sun, Nat. Commun. 9 (2018) 924.
[210] Y. Shen, L. Li, J. Xi, X. Qiu, J. Mater. Chem. A 4 (2016) 5817–5822.
[211] X. Yang, Y.C. Kimmel, J. Fu, B.E. Koel, J.G. Chen, ACS Catal. 2 (2012) 765–769.
[212] Y.T. Xu, X. Xiao, Z.M. Ye, S. Zhao, R. Shen, C.T. He, J.P. Zhang, Y. Li, X.M. Chen, J. Am. Chem. Soc. 139 (2017) 5285–5288.
[213] X. Fan, H. Zhou, X. Guo, ACS Nano 9 (2015) 5125–5134.
[214] S.T. Hunt, T. Nimmanwudipong, Y. Román-Leshkov, Angew. Chem. Int. Ed. 53 (2014) 5131–5136.
[215] F. Wang, P. He, Y. Li, T.A. Shifa, Y. Deng, K. Liu, Q. Wang, F. Wang, Y. Wen, Z. Wang, X. Zhan, L. Sun, J. He, Adv. Funct. Mater. 27 (2017) 1605802.
[216] G. Yan, C. Wu, H. Tan, X. Feng, L. Yan, H. Zang, Y. Li, J. Mater. Chem. A 5 (2017) 765–772.
[217] P.K. Shen, S. Yin, Z. Li, C. Chen, Electrochim. Acta 55 (2010) 7969–7974.
[218] A.S. Kurlov, A.I. Gusev, Inorg. Mater. 42 (2006) 121–127.
[219] S. Wang, J. Wang, M. Zhu, X. Bao, B. Xiao, D. Su, H. Li, Y. Wang, J. Am. Chem. Soc. 137 (2015) 15753–15759.
[220] C. Wan, B.M. Leonard, Chem. Mater. 27 (2015) 4281–4288.
[221] X. Xu, F. Nosheen, X. Wang, Chem. Mater. 28 (2016) 6313–6320.
[222] L.F. Pan, Y.H. Li, S. Yang, P.F. Liu, M.Q. Yu, H.G. Yang, Chem. Commun. 50 (2014) 13135–13137.
[223] P. Li, J. Zhu, A.D. Handoko, R. Zhang, H. Wang, D. Legut, X. Wen, Z. Fu, Z.W. She, Q. Zhang, J. Mater. Chem. A 6 (2018) 4271–4278.
[224] H. Vrubel, X. Hu, Angew. Chem. Int. Ed. 124 (2012) 12875–12878.
[225] C. Wan, Y.N. Regmi, B.M. Leonard, Angew. Chem. Int. Ed. 126 (2014) 6525–6528.
[226] L. Liao, S. Wang, J. Xiao, X. Bian, Y. Zhang, M.D. Scanlon, X. Hu, Y. Tang, B. Liu, H.H. Girault, Energy Environ. Sci. 7 (2014) 387–392.
[227] W.F. Chen, C.H. Wang, K. Sasaki, N. Marinkovic, W. Xu, J.T. Muckerman, Y. Zhu, R.R. Adzic, Energy Environ. Sci. 6 (2013) 943–951.
[228] T.G. Kelly, S.T. Hunt, D.V. Esposito, J.G. Chen, Int. J. Hydrog. Energy 38 (2013) 5638–5644.
[229] M.C. Weidman, D.V. Esposito, Y.C. Hsu, J.G. Chen, J. Power Sources 202 (2012) 11–17.
[230] S. Wirth, F. Harnisch, M. Weinmann, U. Schröder, Appl. Catal. B 126 (2012) 225–230.
[231] W. Yuan, L. Cheng, Y. An, H. Wu, N. Yao, X. Fan, X. Guo, A.C.S. Sustain, Chem. Eng. 6 (2018) 8976–8982.
[232] Y.N. Regmi, G.R. Waetzig, K.D. Duffee, S.M. Schmuecker, J.M. Thode, B.M. Leonard, J. Mater. Chem. A 3 (2015) 10085–10091.
[233] H. Xu, J. Wan, H. Zhang, L. Fang, L. Liu, Z. Huang, J. Li, X. Gu, Y. Wang, Adv. Energy Mater. 8 (2018) 1800575.
[234] S.M. Schmuecker, D. Clouser, T.J. Kraus, B.M. Leonard, Dalton T 46 (2017) 13524–13530.
[235] X. Fan, Z. Peng, R. Ye, H. Zhou, X. Guo, ACS Nano 9 (2015) 7407–7418.
[236] S. Li, C. Yang, Z. Yin, H. Yang, Y. Chen, L. Lin, M. Li, W. Li, G. Hu, D. Ma, Nano Res. 10 (2017) 1322–1328.
[237] H. Fan, H. Yu, Y. Zhang, Y. Zheng, Y. Luo, Z. Dai, B. Li, Y. Zong, Q. Yan, Angew. Chem. Int. Ed. 56 (2017) 12566–12570.
[238] D.A. Papaconstantopoulos, W.E. Pickett, B.M. Klein, L.L. Boyer, Phys. Rev. B 31 (1985) 752–761.
[239] J.G. Chen, Chem. Rev. 96 (1996) 1477–1498.
[240] Y.S. Jun, W.H. Hong, M. Antonietti, A. Thomas, Adv. Mater. 21 (2009) 4270–4274.
[241] W.F. Chen, S. Iyer, S. Iyer, K. Sasaki, C.H. Wang, Y. Zhu, J.T. Muckerman, E. Fujita, Energy Environ. Sci. 6 (2013) 1818–1826.
[242] M. Zhou, Q. Weng, Z.I. Popov, Y. Yang, L.Y. Antipina, P.B. Sorokin, X. Wang, Y. Bando, D. Golberg, ACS Nano 12 (2018) 4148–4155.
[243] W.F. Chen, K. Sasaki, C. Ma, A.I. Frenkel, N. Marinkovic, J.T. Muckerman, Y. Zhu, R.R. Adzic, Angew. Chem. Int. Ed. 51 (2012) 6131–6135.
[244] W.F. Chen, J.M. Schneider, K. Sasaki, C.H. Wang, J. Schneider, S. Iyer, Y. Zhu, J.T. Muckerman, E. Fujita, ChemSusChem 7 (2014) 2414–2418.
[245] Z. Lv, M. Tahir, X. Lang, G. Yuan, L. Pan, X. Zhang, J.J. Zou, J. Mater. Chem. A 5 (2017) 20932–20937.
[246] X. Jia, Y. Zhao, G. Chen, L. Shang, R. Shi, X. Kang, G.I.N. Waterhouse, L.Z. Wu, C.H. Tung, T. Zhang, Adv. Energy Mater. 6 (2016) 1502585.
[247] Y. Zhang, B. Ouyang, J. Xu, S. Chen, R.S. Rawat, H.J. Fan, Adv. Energy Mater. 6 (2016) 1600221.
[248] J. Shi, Z. Pu, Q. Liu, A.M. Asiri, J. Hu, X. Sun, Electrochim. Acta 154 (2015) 345–351.
[249] H. Jin, H. Zhang, J. Chen, S. Mao, Z. Jiang, Y. Wang, J. Mater. Chem. A 6 (2018) 10967–10975.
[250] M. Shalom, D. Ressnig, X. Yang, G. Clavel, T.P. Fellinger, M. Antonietti, J. Mater. Chem. A 3 (2015) 8171–8177.
[251] Z. Chen, Y. Song, J. Cai, X. Zheng, D. Han, Y. Wu, Y. Zang, S. Niu, Y. Liu, J. Zhu, X. Liu, G. Wang, Angew. Chem. Int. Ed. 57 (2018) 5076–5080.
[252] A.L. Stottlemyer, E.C. Weigert, J.G. Chen, Ind. Eng. Chem. Res. 50 (2011) 16–22.
[253] J. Xie, S. Li, X. Zhang, J. Zhang, R. Wang, H. Zhang, B. Pan, Y. Xie, Chem. Sci. 5

(2014) 4615–4620.
[254] Y. Zheng, Y. Jiao, S.Z. Qiao, Adv. Mater. 27 (2015) 5372–5378.
[255] M.R. Gao, J.X. Liang, Y.R. Zheng, Y.F. Xu, J. Jiang, Q. Gao, J. Li, S.H. Yu, Nat. Commun. 6 (2015) 5982.
[256] Y. Jiao, Y. Zheng, P. Chen, M. Jaroniec, S.Z. Qiao, J. Am. Chem. Soc. 139 (2017) 18093–18100.
[257] B. Cao, G.M. Veith, J.C. Neuefeind, R.R. Adzic, P.G. Khalifah, J. Am. Chem. Soc. 135 (2013) 19186–19192.
[258] G. Zhao, K. Rui, S.X. Dou, W. Sun, Adv. Funct. Mater. 28 (2018) 1803291.
[259] L. Zhuang, L. Ge, Y. Yang, M. Li, Y. Jia, X. Yao, Z. Zhu, Adv. Mater. 29 (2017) 1606793.
[260] Y. Tong, P. Chen, T. Zhou, K. Xu, W. Chu, C. Wu, Y. Xie, Angew. Chem. Int. Ed. 129 (2017) 7227–7231.
[261] S. Dou, C.L. Dong, Z. Hu, Y.C. Huang, Jl Chen, L. Tao, D. Yan, D. Chen, S. Shen, S. Chou, S. Wang, Adv. Funct. Mater. 27 (2017) 1702546.
[262] Y. Liang, Y. Li, H. Wang, J. Zhou, J. Wang, T. Regier, H. Dai, Nat. Mater. 10 (2011) 780.
[263] L. Trotochaud, J.K. Ranney, K.N. Williams, S.W. Boettcher, J. Am. Chem. Soc. 134 (2012) 17253–17261.
[264] B.P. Chhetri, C.M. Parnell, H. Wayland, A.B. RanguMagar, G. Kannarpady, F. Watanabe, Y.M. Albkuri, A.S. Biris, A. Ghosh, ChemistrySelect 3 (2018) 922–932.
[265] A. Iwase, S. Yoshino, T. Takayama, Y.H. Ng, R. Amal, A. Kudo, J. Am. Chem. Soc. 138 (2016) 10260–10264.
[266] H.Q. Xu, J. Hu, D. Wang, Z. Li, Q. Zhang, Y. Luo, S.H. Yu, H.L. Jiang, J. Am. Chem. Soc. 137 (2015) 13440–13443.
[267] J.C. Wang, L. Zhang, W.X. Fang, J. Ren, Y.Y. Li, H.C. Yao, J.S. Wang, Z.J. Li, ACS Appl. Mater. Interfaces 7 (2015) 8631–8639.
[268] R. Subbaraman, D. Tripkovic, D. Strmcnik, K.C. Chang, M. Uchimura, A.P. Paulikas, V. Stamenkovic, N.M. Markovic, Science 334 (2011) 1256.
[269] X. Li, S. Ci, J. Jia, Z. Wen, Int. J. Hydrog. Energy 41 (2016) 21246–21250.
[270] A. Phuruangrat, D.J. Ham, S.J. Hong, S. Thongtem, J.S. Lee, J. Mater. Chem. 20 (2010) 1683–1690.
[271] Z. Chen, D. Cummins, B.N. Reinecke, E. Clark, M.K. Sunkara, T.F. Jaramillo, Nano Lett. 11 (2011) 4168–4175.
[272] X. Xie, W. Mu, X. Li, H. Wei, Y. Jian, Q. Yu, R. Zhang, K. Lv, H. Tang, S. Luo, Electrochim. Acta 134 (2014) 201–208.
[273] H. Zheng, M. Mathe, Int. J. Hydrog. Energy 36 (2011) 1960–1964.
[274] H. Wang, H.W. Lee, Y. Deng, Z. Lu, P.C. Hsu, Y. Liu, D. Lin, Y. Cui, Nat. Commun. 6 (2015) 7261.
[275] X. Yan, L. Tian, M. He, X. Chen, Nano Lett. 15 (2015) 6015–6021.
[276] X. Zhong, Y. Sun, X. Chen, G. Zhuang, X. Li, J.G. Wang, Adv. Funct. Mater. 26 (2016) 5778–5786.
[277] Y. Zhao, C. Chang, F. Teng, Y. Zhao, G. Chen, R. Shi, G.I.N. Waterhouse, W. Huang, T. Zhang, Adv. Energy Mater. 7 (2017) 1700005.
[278] D. Su, J. wang, H. Jin, Y. Gong, M. Li, Z. Pang, Y. Wang, J. Mater. Chem. A 3 (2015) 11756–11761.
[279] H. Jin, J. Wang, D. Su, Z. Wei, Z. Pang, Y. Wang, J. Am. Chem. Soc. 137 (2015) 2688–2694.
[280] Y.F. Xu, M.R. Gao, Y.R. Zheng, J. Jiang, S.H. Yu, Angew. Chem. Int. Ed. 125 (2013) 8708–8712.
[281] T. Zhang, M.Y. Wu, D.Y. Yan, J. Mao, H. Liu, W.B. Hu, X.W. Du, T. Ling, S.Z. Qiao, Nano Energy 43 (2018) 103–109.
[282] J. Chen, D. Yu, W. Liao, M. Zheng, L. Xiao, H. Zhu, M. Zhang, M. Du, J. Yao, ACS Appl. Mater. Interfaces 8 (2016) 18132–18139.
[283] A.K. Nayak, M. Verma, Y. Sohn, P.A. Deshpande, D. Pradhan, ACS Omega 2 (2017) 7039–7047.
[284] T. Zheng, W. Sang, Z. He, Q. Wei, B. Chen, H. Li, C. Cao, R. Huang, X. Yan, B. Pan, S. Zhou, J. Zeng, Nano Lett. 17 (2017) 7968–7973.
[285] B. Albert, H. Hillebrecht, Angew. Chem. Int. Ed. 48 (2009) 8640–8668.
[286] V.A. Lavrenko, L.N. Yagupol'skaya, L.I. Kuznetsova, Ehlektrokhimiya 10 (1974) 1078–1081.
[287] B. Albert, H. Hillebrecht, Angew. Chem. Int. Ed. 121 (2009) 8794–8824.
[288] M. Zeng, H. Wang, C. Zhao, J. Wei, K. Qi, W. Wang, X. Bai, ChemCatChem 8 (2016) 708–712.
[289] G.X. Cao, N. Xu, Z.J. Chen, Q. Kang, H.B. Dai, P. Wang, ChemistrySelect 2 (2017) 6187–6193.
[290] C. Adán, F.J. Pérez-Alonso, S. Rojas, M.A. Peña, J.L.G. Fierro, Int. J. Hydrog. Energy 37 (2012) 14984–14991.
[291] F. Baydaroglu, E. Özdemir, A. Hasimoglu, Int. J. Hydrog. Energy 39 (2014) 1516–1522.
[292] P. Los, A. Lasia, J. Electroanal. Chem. 333 (1992) 115–125.
[293] R. Chen, L. Liu, J. Zhou, L. Hou, F. Gao, J. Power Sources 341 (2017) 75–82.
[294] H. Park, Y. Zhang, J.P. Scheifers, P.R. Jothi, A. Encinas, B.P.T. Fokwa, J. Am. Chem. Soc. 139 (2017) 12915–12918.
[295] M. Frotscher, W. Klein, J. Bauer, C.M. Fang, J.F. Halet, A. Senyshyn, C. Baehtz, B. Albert, Z. Anorg. Allg. Chem. 633 (2007) 2626–2630.
[296] H. Li, P. Wen, Q. Li, C. Dun, J. Xing, C. Lu, S. Adhikari, L. Jiang, D.L. Carroll, S.M. Geyer, Adv. Energy Mater. 7 (2017) 1700513.
[297] P. Zou, J. Li, Y. Zhang, C. Liang, C. Yang, H.J. Fan, Nano Energy 51 (2018) 349–357.
[298] C. Hu, Q. Ma, S.F. Hung, Z.N. Chen, D. Ou, B. Ren, H.M. Chen, G. Fu, N. Zheng, Chem 3 (2017) 122–133.
[299] Y. Kuang, G. Feng, P. Li, Y. Bi, Y. Li, X. Sun, Angew. Chem. Int. Ed. 55 (2015) 693–697.
[300] N. Danilovic, R. Subbaraman, D. Strmcnik, K.C. Chang, A.P. Paulikas, V.R. Stamenkovic, N.M. Markovic, Angew. Chem. Int. Ed. 124 (2012) 12663–12666.
[301] H. Fei, Y. Yang, Z. Peng, G. Ruan, Q. Zhong, L. Li, E.L.G. Samuel, J.M. Tour, ACS Appl. Mater. Interfaces 7 (2015) 8083–8087.
[302] D. Hou, W. Zhou, K. Zhou, Y. Zhou, J. Zhong, L. Yang, J. Lu, G. Li, S. Chen, J. Mater. Chem. A 3 (2015) 15962–15968.
[303] J. Deng, P. Ren, D. Deng, X. Bao, Angew. Chem. Int. Ed. 54 (2015) 2100–2104.
[304] Y. Zhang, Y. Ma, Y.Y. Chen, L. Zhao, L.B. Huang, H. Luo, W.J. Jiang, X. Zhang, S. Niu, D. Gao, J. Bi, G. Fan, J.S. Hu, ACS Appl. Mater. Interfaces 9 (2017) 36857–36864.
[305] Z. Chen, R. Wu, Y. Liu, Y. Ha, Y. Guo, D. Sun, M. Liu, F. Fang, Adv. Mater. 30 (2018) 1802011.
[306] X. Zou, X. Huang, A. Goswami, R. Silva, B.R. Sathe, E. Mikmeková, T. Asefa, Angew. Chem. Int. Ed. 53 (2014) 4372–4376.
[307] Y. Ito, T. Ohto, D. Hojo, M. Wakisaka, Y. Nagata, L. Chen, K. Hu, M. Izumi, Ji Fujita, T. Adschiri, ACS Catal. 8 (2018) 3579–3586.
[308] H. Su, H.H. Wang, B. Zhang, K.X. Wang, X.H. Li, J.S. Chen, Nano Energy 22 (2016) 79–86.
[309] Q. Zhang, P. Li, D. Zhou, Z. Chang, Y. Kuang, X. Sun, Small 13 (2017) 1701648.
[310] J. Wang, D. Gao, G. Wang, S. Miao, H. Wu, J. Li, X. Bao, J. Mater. Chem. A 2 (2014) 20067–20074.
[311] H. Zhang, Z. Ma, J. Duan, H. Liu, G. Liu, T. Wang, K. Chang, M. Li, L. Shi, X. Meng, K. Wu, J. Ye, ACS Nano 10 (2016) 684–694.
[312] M. Tavakkoli, T. Kallio, O. Reynaud, A.G. Nasibulin, C. Johans, J. Sainio, H. Jiang, E.I. Kauppinen, K. Laasonen, Angew. Chem. Int. Ed. 54 (2015) 4535–4538.
[313] B. Liu, L. Zhang, W. Xiong, M. Ma, Angew. Chem. Int. Ed. 55 (2016) 6725–6729.
[314] L. Wang, Y. Li, M. Xia, Z. Li, Z. Chen, Z. Ma, X. Qin, G. Shao, J. Power Sources 347 (2017) 220–228.
[315] X.F. Yang, A. Wang, B. Qiao, J. Li, J. Liu, T. Zhang, Acc. Chem. Res. 46 (2013) 1740–1748.
[316] E.C. Tyo, S. Vajda, Nat. Nanotechnol. 10 (2015) 577.
[317] H. Fei, J. Dong, Y. Feng, C.S. Allen, C. Wan, B. Volosskiy, M. Li, Z. Zhao, Y. Wang, H. Sun, P. An, W. Chen, Z. Guo, C. Lee, D. Chen, I. Shakir, M. Liu, T. Hu, Y. Li, A.I. Kirkland, X. Duan, Y. Huang, Nat. Catal. 1 (2018) 63–72.
[318] S. Wei, A. Li, J.C. Liu, Z. Li, W. Chen, Y. Gong, Q. Zhang, W.C. Cheong, Y. Wang, L. Zheng, H. Xiao, C. Chen, D. Wang, Q. Peng, L. Gu, X. Han, J. Li, Y. Li, Nat. Nanotechnol. 13 (2018) 856–861.
[319] N. Cheng, S. Stambula, D. Wang, M.N. Banis, J. Liu, A. Riese, B. Xiao, R. Li, T.K. Sham, L.M. Liu, G.A. Botton, X. Sun, Nat. Commun. 7 (2016) 13638.
[320] J. Deng, H. Li, J. Xiao, Y. Tu, D. Deng, H. Yang, H. Tian, J. Li, P. Ren, X. Bao, Energy Environ. Sci. 8 (2015) 1594–1601.
[321] M. Yang, L.F. Allard, M. Flytzani-Stephanopoulos, J. Am. Chem. Soc. 135 (2013) 3768–3771.
[322] G. Li, R. Jin, Acc. Chem. Res. 46 (2013) 1749–1758.
[323] G. Kyriakou, M.B. Boucher, A.D. Jewell, E.A. Lewis, T.J. Lawton, A.E. Baber, H.L. Tierney, M. Flytzani-Stephanopoulos, E.C.H. Sykes, Science 335 (2012) 1209.
[324] P. Liu, Y. Zhao, R. Qin, S. Mo, G. Chen, L. Gu, D.M. Chevrier, P. Zhang, Q. Guo, D. Zang, B. Wu, G. Fu, N. Zheng, Science 352 (2016) 797.
[325] L. Fan, P.F. Liu, X. Yan, L. Gu, Z.Z. Yang, H.G. Yang, S. Qiu, X. Yao, Nat. Commun. 7 (2016) 10667.
[326] H. Fei, J. Dong, M.J. Arellano-Jiménez, G. Ye, N. Dong Kim, E.L.G. Samuel, Z. Peng, Z. Zhu, F. Qin, J. Bao, M.J. Yacaman, P.M. Ajayan, D. Chen, J.M. Tour, Nat. Commun. 6 (2015) 8668.
[327] H.J. Qiu, Y. Ito, W. Cong, Y. Tan, P. Liu, A. Hirata, T. Fujita, Z. Tang, M. Chen, Angew. Chem. Int. Ed. 54 (2015) 14031–14035.
[328] J.R. McKone, E.L. Warren, M.J. Bierman, S.W. Boettcher, B.S. Brunschwig, N.S. Lewis, H.B. Gray, Energy Environ. Sci. 4 (2011) 3573–3583.
[329] X. Wang, R. Su, H. Aslan, J. Kibsgaard, S. Wendt, L. Meng, M. Dong, Y. Huang, F. Besenbacher, Nano Energy 12 (2015) 9–18.
[330] J. Duan, S. Chen, C. Zhao, Nat. Commun. 8 (2017) 15341.
[331] D.E. Brown, M.N. Mahmood, M.C.M. Man, A.K. Turner, Electrochim. Acta 29 (1984) 1551–1556.
[332] Q. Lu, G.S. Hutchings, W. Yu, Y. Zhou, R.V. Forest, R. Tao, J. Rosen, B.T. Yonemoto, Z. Cao, H. Zheng, J.Q. Xiao, F. Jiao, J.G. Chen, Nat. Commun. 6 (2015) 6567.
[333] Z. Xing, D. Wang, Q. Li, A.M. Asiri, X. Sun, Electrochim. Acta 210 (2016) 729–733.
[334] Y. Shen, Y. Zhou, D. Wang, X. Wu, J. Li, J. Xi, Adv. Energy Mater. 8 (2017) 1701759.
[335] J.M.V. Nsanzimana, Y. Peng, M. Miao, V. Reddu, W. Zhang, H. Wang, B.Y. Xia, X. Wang, A.C.S. Appl, Nano Mater. 1 (2018) 1228–1235.
[336] Y. Yang, Z. Lin, S. Gao, J. Su, Z. Lun, G. Xia, J. Chen, R. Zhang, Q. Chen, ACS Catal. 7 (2017) 469–479.
[337] Y. Feng, X.Y. Yu, U. Paik, Sci. Rep. 6 (2016) 34004.
[338] J.R. McKone, B.F. Sadtler, C.A. Werlang, N.S. Lewis, H.B. Gray, ACS Catal. 3 (2013) 166–169.
[339] L. Zhang, K. Xiong, Y. Nie, X. Wang, J. Liao, Z. Wei, J. Power Sources 297 (2015) 413–418.
[340] G. Bianchi, F. Mazza, S. Trasatti, Z. Phys. Chem. 226 (1964) 40–58.
[341] P. Rüetschi, J. Ockerman, R. Amlie, J. Electrochem. Soc. 107 (1960) 325–332.
[342] D. Gao, J. Zhang, T. Wang, W. Xiao, K. Tao, D. Xue, J. Ding, J. Mater. Chem. A 4 (2016) 17363–17369.
[343] X. Wang, W. Li, D. Xiong, D.Y. Petrovykh, L. Liu, Adv. Funct. Mater. 26 (2016) 4067–4077.
[344] Z. Jin, P. Li, X. Huang, G. Zeng, Y. Jin, B. Zheng, D. Xiao, J. Mater. Chem. A 2 (2014) 18593–18599.
[345] C. Wang, T. Ding, Y. Sun, X. Zhou, Y. Liu, Q. Yang, Nanoscale 7 (2015)

19241–19249.
[346] N. Jiang, B. You, M. Sheng, Y. Sun, Angew. Chem. Int. Ed. 127 (2015) 6349–6352.
[347] Z. Pu, Q. Liu, P. Jiang, A.M. Asiri, A.Y. Obaid, X. Sun, Chem. Mater. 26 (2014) 4326–4329.
[348] Y. Liang, Q. Liu, A.M. Asiri, X. Sun, Y. Luo, ACS Catal. 4 (2014) 4065–4069.
[349] L. Tian, X. Yan, X. Chen, ACS Catal. 6 (2016) 5441–5448.
[350] C.Y. Son, I.H. Kwak, Y.R. Lim, J. Park, Chem. Commun. 52 (2016) 2819–2822.
[351] X. Wang, W. Ma, Z. Xu, H. Wang, W. Fan, X. Zong, C. Li, Nano Energy 48 (2018) 500–509.
[352] M. Pi, W. Guo, T. Wu, X. Wang, D. Zhang, S. Wang, S. Chen, J. Power Sources 364 (2017) 253–257.
[353] R. Zhang, X. Wang, S. Yu, T. Wen, X. Zhu, F. Yang, X. Sun, X. Wang, W. Hu, Adv. Mater. 29 (2016) 1605502.
[354] A. Ignaszak, C. Song, W. Zhu, J. Zhang, A. Bauer, R. Baker, V. Neburchilov, S. Ye, S. Campbell, Electrochim. Acta 69 (2012) 397–405.
[355] S.J. Stott, R.J. Mortimer, S.E. Dann, M. Oyama, F. Marken, Phys. Chem. Chem. Phys. 8 (2006) 5437–5443.
[356] T. Ferri, D. Gozzi, A. Latini, Int. J. Hydrog. Energy 32 (2007) 4692–4701.
[357] G.A. Tsirlina, O.A. Petrii, Electrochim. Acta 32 (1987) 649–657.
[358] J. Song, G.R. Li, F.Y. Xiong, X.P. Gao, J. Mater. Chem. 22 (2012) 20580–20585.
[359] Z. Shi, K. Nie, Z.J. Shao, B. Gao, H. Lin, H. Zhang, B. Liu, Y. Wang, Y. Zhang, X. Sun, X.M. Cao, P. Hu, Q. Gao, Y. Tang, Energy Environ. Sci. 10 (2017) 1262–1271.
[360] B. Ren, D. Li, Q. Jin, H. Cui, C. Wang, J. Mater. Chem. A 5 (2017) 13196–13203.
[361] M. Zeng, Y. Chen, J. Li, H. Xue, R.G. Mendes, J. Liu, T. Zhang, M.H. Rümmeli, L. Fu, Nano Energy 33 (2017) 356–362.
[362] B. Ren, D. Li, Q. Jin, H. Cui, C. Wang, J. Mater. Chem. A 5 (2017) 19072–19078.
[363] Y. Zhu, G. Chen, Y. Zhong, W. Zhou, Z. Shao, Adv. Sci. 5 (2017) 1700603.
[364] C. Zhu, A.L. Wang, W. Xiao, D. Chao, X. Zhang, N.H. Tiep, S. Chen, J. Kang, X. Wang, J. Ding, J. Wang, H. Zhang, H.J. Fan, Adv. Mater. 30 (2018) 1705516.
[365] Y. Zhao, K. Kamiya, K. Hashimoto, S. Nakanishi, Angew. Chem. Int. Ed. 52 (2013) 13638–13641.
[366] H. Yan, C. Tian, L. Wang, A. Wu, M. Meng, L. Zhao, H. Fu, Angew. Chem. Int. Ed. 54 (2015) 6325–6329.
[367] J. Yin, Q. Fan, Y. Li, F. Cheng, P. Zhou, P. Xi, S. Sun, J. Am. Chem. Soc. 138 (2016) 14546–14549.
[368] Y. Ma, Z. He, Z. Wu, B. Zhang, Y. Zhang, S. Ding, C. Xiao, J. Mater. Chem. A 5 (2017) 24850–24858.
[369] Y. Zhao, C. Chang, F. Teng, Y. Zhao, G. Chen, R. Shi, G.I.N. Waterhouse, W. Huang, T. Zhang, Adv. Energy Mater. 7 (2017) 1700005.
[370] X. Yan, L. Tian, X. Chen, J. Power Sources 300 (2015) 336–343.
[371] K. Liu, W. Zhang, F. Lei, L. Liang, B. Gu, Y. Sun, B. Ye, W. Ni, Y. Xie, Nano Energy 30 (2016) 810–817.
[372] X. Wang, G. Tai, Z. Wu, T. Hu, R. Wang, J. Mater. Chem. A 5 (2017) 23471–23475.
[373] S. Gupta, N. Patel, A. Miotello, D.C. Kothari, J. Power Sources 279 (2015) 620–625.
[374] L.T. Alameda, C.F. Holder, J.L. Fenton, R.E. Schaak, Chem. Mater. 29 (2017) 8953–8957.
[375] N. Xu, G. Cao, Z. Chen, Q. Kang, H. Dai, P. Wang, J. Mater. Chem. A 5 (2017) 12379–12384.
[376] S. Gupta, N. Patel, R. Fernandes, R. Kadrekar, A. Dashora, A.K. Yadav, D. Bhattacharyya, S.N. Jha, A. MiotelloD, C. Kothari, Appl. Catal. B 192 (2016) 126–133.
[377] J. Masa, P. Weide, D. Peeters, I. Sinev, W. Xia, Z. Sun, C. Somsen, M. Muhler, W. Schuhmann, Adv. Energy Mater. 6 (2016) 1502313.
[378] W. Chen, J. Pei, C.T. He, J. Wan, H. Ren, Y. Zhu, Y. Wang, J. Dong, S. Tian, W.C. Cheong, S. Lu, L. Zheng, X. Zheng, W. Yan, Z. Zhuang, C. Chen, Q. Peng, D. Wang, Y. Li, Angew. Chem. Int. Ed. 129 (2017) 16302–16306.

Peng Yu received his Bachelor's degree in materials chemistry from Hubei Engineering University in 2015. Currently, he is a Ph.D. candidate in Prof. Jun He's group at National Center for Nanoscience and Technology (NCNST) and Prof. Fan Xia's group at China University of Geosciences (Wuhan). His current research interests focus on the development of advanced 2D materials for various catalytic applications, ranging from hydrogen evolution reactions, oxygen reduction reactions, to carbon dioxide reduction.

Fengmei Wang received her B.S. degree in applied chemistry from Hunan University, China, in 2012. Then she received her Ph.D. degree in physical chemistry from the University of Chinese Academy of Sciences at the National Center for Nanoscience and Technology (NCNST), China, in 2017. From then on, she worked in NCNST as an assistant professor. Her major research interests include synthesis and development of novel 2D materials, such as transition metal chalcogenides, meal phosphorous trichalcogenides, etc., for electrocatalysis or photocatalysis.

Tofik A. Shifa received his B.S. degree in applied chemistry from Arbaminch University, Ethiopia in 2007. He then obtained his M.S. degree in analytical chemistry from Haramaya University, Ethiopia in 2011. He has recently got a Ph.D. degree in physical chemistry from the University of Chinese Academy of Sciences at the National Center for Nanoscience and Technology (NCNST), Beijing, China. His research focuses on the controllable synthesis of 2D layered materials for water splitting.

Xueying Zhan received her B.S. degree at Huazhong University of Science and Technology, China, in 2010. Then she obtained her Master degree of optoelectronic engineering from College of Optoelectronic Science and Engineering, HUST, in 2013. From then on, she worked as an engineer at National Center for Nanoscience and Technology, Chinese Academy of Science. Her major research interests include controllable synthesis and applications of 1D and composite nanomaterials in the area of optoelectronics and photocatalysis.

Xiaoding Lou received her Ph.D. at Wuhan University, in 2012. She then worked for one year as a Research Associate in Prof. Benzhong Tang's group at the Hong Kong University of Science and Technology. After finishing her work in 2013, she became an assistant professor and associate professor at the Huazhong University of Science and Technology, respectively. In 2016, she worked at the University of California, Santa Barbara in the group Prof. Alan J. Heeger. Since 2017, she has been a Professor at the China University of Geosciences (Wuhan). Her scientific interest is focused on the chemical and biosensor field.

Fan Xia received his Ph.D. in physical chemistry from the Institute of Chemistry, Chinese Academy of Sciences (CAS) under the supervision of Prof. Lei Jiang, in 2008. He then worked as a postdoctoral fellow in Prof. Alan J. Heeger's group at the University of California, Santa Barbara. He joined the Huazhong University of Science and Technology (HUST) as part of the 1000 Young Talents Program in 2012 and became professor at HUST. He is currently a professor and Dean of Faculty of Materials Science and Chemistry, China University of Geosciences (Wuhan). His scientific interest is focused on bioanalytical chemistry.

Jun He received his Ph.D. in semiconductor physics from the Institute of Semiconductors, Chinese Academy of Sciences (CAS), in 2003. Then he worked successively at the Applied Physics Department of Technische Universiteit Eindhoven, Netherlands, the Material Department of University of California, Santa Babara, and California NanoSystem Insitute (CNSI), University of California, Los Angeles, USA. He joined the "100-Talents" Program of CAS in November 2010 and became a full professor of NCNST since then. His main research interests are the synthesis, characterization, and devices of low dimensional semiconductor materials.